

## Review

# Pairing in excited nuclei: a review

N Quang Hung<sup>1</sup> , N Dinh Dang<sup>2</sup> and L G Moretto<sup>3</sup><sup>1</sup> Institute of Fundamental and Applied Sciences, Duy Tan University, Ho Chi Minh city 700000, Vietnam<sup>2</sup> Quantum Hadron Physics Laboratory, RIKEN Nishina Center for Accelerator-Based Science, 2-1 Hirosawa, Wako City, 351-0198 Saitama, Japan<sup>3</sup> University of California, Berkeley and Lawrence Berkeley National Laboratory, 1 Cyclotron Road, Berkeley, CA 94720, United States of AmericaE-mail: [nqhungdtu@gmail.com](mailto:nqhungdtu@gmail.com), [dang@riken.jp](mailto:dang@riken.jp) and [lmoretto@lbl.gov](mailto:lmoretto@lbl.gov)

Received 26 July 2017, revised 21 November 2018

Accepted for publication 8 February 2019

Published 17 April 2019



Corresponding Editor Professor Gordon Baym

**Abstract**

The present review summarizes the recent studies on the thermodynamic properties of pairing in many-body systems including superconductors, metallic nanosized clusters and/or grains, solid-state materials, focusing on the excited nuclei, that is nuclei at finite temperature and/or angular momentum formed via heavy-ion fusion,  $\alpha$ -induced fusion reactions, or inelastic scattering of light particles on heavy targets. Because of the finiteness of the systems, several interesting effects of pairing such as nonvanishing pairing gap, smoothing of superfluid-normal phase transition, first and second order phase transitions, pairing reentrance, etc, will be discussed in detail. Influences of exact and approximate thermal pairing on some nuclear properties such as temperature-dependent width of the giant dipole resonance, total level density, and radiative strength function of the  $\gamma$ -rays emission will be also analyzed. Finally, the first experimental evidence of the pairing reentrance phenomenon in a  $^{104}\text{Pd}$  nucleus as well as its solid-state counterpart of ferromagnets under strong magnetic field will be presented.

Keywords: pairing correlation, excited nuclei, hot rotating nuclei, phase transition, statistical nuclear thermodynamics, giant dipole resonance, nuclear level density and radiative strength function

(Some figures may appear in colour only in the online journal)

**Contents**

1. Introduction.....	2		
2. Pairing within the uniform model.....	4		
2.1. BCS Hamiltonian within the grand canonical ensemble at fixed angular momentum.....	4		
2.1.1. General theory.....	4		
2.1.2. Level density and statistical quantities.....	5		
2.2. Applications of the theory to the uniform model.....	6		
2.2.1. Single-particle model.....	6		
2.2.2. Dependence of gap parameter upon angular momentum at zero temperature ( $\beta = \infty$ ).....	6		
2.2.3. Dependence of gap parameter upon angular momentum and excitation energy.....	6		
2.2.4. Transition from temperature scale to energy scale.....	8		
2.2.5. Entropy.....	9		
2.2.6. Level-density denominator.....	9		
2.3. Completeness of formalism with respect to angular momentum.....	9		

2.4. Effect of single-particle spin projection distribution upon the shape of the yrast line .....	9
2.5. Transition from the constant spacing model to the shell model .....	10
2.6. Thermodynamic properties of paired nucleus with fixed number of quasiparticles .....	11
2.6.1. Hamiltonian. ....	11
2.6.2. Grand partition function and other thermodynamic quantities.....	11
2.6.3. Limiting properties for $T = 0$ ( $\beta \rightarrow \infty$ ).....	12
2.6.4. Properties of the system for $T > 0$ .....	13
2.7. Experimental level densities and first-order pairing phase transition .....	15
3. Grand-canonical ensemble treatment of pairing problem within the Hartree–Fock–Bogoliubov theory and finite-temperature pairing reentrance .....	16
3.1. Hartree–Fock–Bogoliubov theory for hot and hot rotating nuclei .....	16
3.2. Finite-temperature pairing reentrance in even–even nuclei .....	20
3.3. Finite-temperature pairing reentrance in odd nuclei.....	21
4. Canonical and microcanonical treatments of pairing problem.....	23
4.1. Particle-number projection.....	23
4.2. BCS with Lipkin–Nogami particle number projection plus self-consistent quasiparticle random-phase approximation incorporated into the canonical and microcanonical ensembles.....	25
4.3. Exact solutions within the canonical and microcanonical ensembles .....	28
4.4. Shell model Monte Carlo method at finite temperature .....	30
5. Experimental evidences .....	32
5.1. Experimental evidence of pairing reentrance in nuclei.....	32
5.2. Condensed-matter counterpart: magnetic-field-induced superconductivity .....	34
5.2.1. Magnetic-field-induced superconductivity based on Jaccarino–Peter compensation effect. ....	35
5.2.2. Unconventional magnetic-field-induced superconductivity: Reentrant superconductivity. ....	36
6. Role of pairing in properties of excited nuclei.....	37
6.1. Effect of thermal pairing on giant dipole resonance in hot nuclei.....	37
6.1.1. Effect of BCS pairing on energy and line shape. ....	37
6.1.2. Effect of modified BCS and exact pairing on the width of giant dipole resonance within phonon-damping model. ....	38
6.1.3. Effect of pairing fluctuation on the width of giant dipole resonance within thermal shape fluctuation model.....	39

6.2. Effect of exact thermal pairing on nuclear level density and radiative strength function.....	41
7. Summary and outlook.....	43
Acknowledgments.....	44
References.....	44

## 1. Introduction

Pairing correlation is a common feature characterizing the superconducting (superfluid) properties of strongly interacting many-body systems ranging from the very large ones such as neutron stars to the tiny ones such as atomic nuclei. In macroscopic and/or infinite systems such as low-temperature superconductors, pairing correlation decreases with increasing temperature  $T$  or excitation energy and completely vanishes when the temperature reaches a critical value  $T = T_c$ , called critical temperature. As the result, the system undergoes a phase transition from superfluid to normal phases (superfluid-normal phase transition). This phenomenon was explained very well by the Bardeen–Cooper–Schrieffer (BCS) theory of superconductivity [1]. The latter was proposed based on an assumption that two electrons, one with spin up and one with spin down, in superconductors tend to couple to form a so-called Cooper pair at low temperatures. The condensation of a set of Cooper pairs is responsible for the superconductivity of the materials. Pairing has been found to have a significant contribution in the study of various systems including liquid helium [2], neutron stars [3–5], interacting spins [6, 7], metal clusters [8–10], quantum dots [11], ultrasmall metallic grains [12, 13], etc. The BCS theory predicts the value of the critical temperature  $T_c$ , at which the pairing gap collapses, to be  $T_c \approx 0.568\Delta(0)$ , where  $\Delta(0)$  is the pairing gap at zero temperature. After the introduction of the BCS, Bohr, Mottelson, and Pines recognized the similarity between the electron pairs in superconducting materials and the nucleon (neutron or proton) pairs observed in atomic nuclei [14, 15] and proposed the nuclear superconductivity (superfluidity). Applications of the BCS theory to nuclear system, explicitly performed by Belyaev [16, 17], Soloviev [18, 19], and others [20–29] showed that pairing correlation affects most of the nuclear structure properties, from binding energy, single-particle orbitals to excitation spectra, transition probabilities, collective vibrational and rotational excitations, deformation, thermal properties, level density, etc. In excited nuclei, the increase of temperature or excitation energy breaks the nucleon pairs located around the Fermi levels, which are responsible mostly for the pairing correlation. The unpaired nucleons scatter to the single-particle levels nearby, entirely block them because of the Pauli exclusion principle. This causes the decrease of pairing correlation. When temperature is high enough, reaching its critical value  $T_c$ , all the nucleon pairs are broken, completely destroying the nuclear pairing. Similarly, when the nuclei are excited by rotation, the Coriolis force, which tends to resist the nuclear rotation, is responsible for breaking the nucleon pairs. This force increases with the total angular momentum  $J$  or rotational frequency and at a certain critical angular momentum  $J_c$ , pairing correlation in

rotating nuclei vanishes after all the nucleon pairs are broken. This is the well-known Mottelson–Valatin effect [20].

However, when both temperature and angular-momentum effects act together as in hot rotating nuclei, there appears an anomalous phenomenon, called pairing reentrance. This phenomenon, which was first introduced by Kamuri [23], occurs when the angular momentum of the nucleus is slightly higher than its critical value  $J_c$ . When it takes place, the pairing correlation, which is zero at low temperature, becomes nonzero at a certain temperature, and increases to reach a maximum, then decreases to vanish at a higher temperature. This phenomenon was later confirmed by Moretto [25, 26] by extending the BCS theory to finite temperature and angular momentum and applied it to the nuclear uniform model. The recent study of the projected pairing gaps in ultra-small metallic grains for even and odd numbers of particles also found such anomalous pairing or pairing reentrance (see e.g. figure 9 of [30]). A similar effect called unconventional superconductivity has been recently discovered in the experimental study of superconducting URhGe material in the presence of magnetic field  $H$  [31], whose role is similar to the rotation in nuclei. In this experiment, the URhGe material in the normal state at the applied magnetic field around 2 T becomes superconducting at low temperature as the magnetic field increases up to the values between 8 and 13 T.

Indeed, all the above predictions of the pairing reentrance phenomenon are the results of using the BCS theory. This theory is precise only in infinite and/or very large systems, where the average size of the Cooper pairs (coherence length) is normally large and thermal fluctuations are negligible. For small systems such as underdoped cuprates, where the coherence length is very short, the thermal fluctuations are no longer small, which require a serious reexamination of the BCS theory [32]. Similarly, nuclear system is expected to have large thermal fluctuations due to its finiteness (small number of nucleons compressed into a fixed volume with the diameter of several fermi). Various theoretical studies of the effect of thermal fluctuations on pairing in atomic nuclei have been undertaken in the past three decades. In the pioneering works by Moretto [24], who employed the macroscopic Landau theory of phase transition to evaluate the most probable value of the pairing gap in a uniform model of nuclear pairing problem, it has been pointed out that the average pairing gap does not collapse at the critical temperature as predicted by the BCS theory but monotonically decreases with increasing temperature. Consequently, the superfluid-normal phase transition observed via the discontinuity of the associated specific heat is smoothed out. This approach was later employed by Goodman [33, 34] to include the thermal fluctuations in the Hartree–Fock–Bogoliubov (HFB) theory at finite temperature. The calculations within the static-path approximation (SPA), in which thermal fluctuations are taken into account by taking the thermal average over all static paths around the mean field, also came to the non-vanishing of pairing gap at finite temperature, in agreement with the predictions by Moretto and Goodman in [25, 33]. This result was later reconfirmed by the shell model [35] and shell-model Monte Carlo [36] calculations for realistic nuclei. Recently, by taking

into account the effect of quasiparticle-number fluctuations in the BCS pairing, two microscopic approaches, called modified BCS (MBCS) [37] and finite-temperature BCS1 [38] theories, have been proposed, which pointed out that the quasiparticle-number fluctuations are indeed the microscopic origin that causes the non-vanishing of thermal pairing gap in finite small systems. The predictions of the above-mentioned approaches are in qualitative agreement with the empirical pairing gap of  $^{184}\text{W}$  nucleus extracted from the experimental nuclear level densities [39] as well as that obtained by incorporating the exact solutions of the pairing Hamiltonian into the canonical and grand canonical ensembles [40]. The effect of non-vanishing thermal pairing has also been included in the phonon damping model (PDM) for describing the width of the isovector giant dipole resonance (GDR). The results obtained show that, because of non-vanishing thermal pairing, the GDR width remains almost unchanged, or even reduced at the temperature  $T \leq 1$  MeV, in good agreement with the experimental data [37, 41–43]. It is worthwhile to mention that this nearly temperature-independent value of the experimental GDR width at low temperature was not previously explained in other approaches, which either include only the BCS pairing or neglect pairing. A similar conclusion on the temperature dependence of the GDR width has been made by including thermal pairing fluctuations in the thermal shape fluctuation model, which cause the noncollapsing average pairing gaps [44]. Moreover, a very recent unified microscopic approach based on the exact solutions of the pairing Hamiltonian at zero temperature has been proposed. These exact solutions are incorporated into the canonical ensemble and then combined with the finite-temperature independent-particle model as well as the PDM to simultaneously describe, for the first time, two key quantities of hot nuclei, namely nuclear level density and radiative strength function of the  $\gamma$ -ray emission, which are important for the description of low-energy nuclear reactions as well as nucleosynthesis in stars [45]. It has been shown in [45] that exact thermal pairing, which results in the non-vanishing of pairing gap and smoothing of the superfluid-normal phase transition, plays an important role in the description of the total nuclear level density as well as the radiative strength function of excited nuclei in the energy region below the particle-separation energy.

Due to the presence of thermal fluctuations, the behavior of pairing reentrance in hot rotating nuclear systems is quantitatively different with other macroscopic ones. In fact, by incorporating the exact solutions of a simple pure pairing model into the canonical ensemble at finite temperature and rotational frequency, it has been found in [46] that there appears the temperature-induced pairing correlation, which is the same as the pairing reentrance, at a given value of the external magnetic field as in the case of nanometer-size superconducting clusters or the rotational frequency as in the case of atomic nuclei. However, different from all the predictions of the BCS theory mentioned above, the reentrance phenomenon occurs in such a way that the pairing gap reappears at a given temperature and remains finite at higher temperature due to the strong fluctuations of the order parameters as explained in [46]. The later calculations within a more realistic and exactly

solvable shell-model Hamiltonian at finite temperature and total angular momentum [47] showed a similar pairing reentrance effect. This behavior of pairing reentrance was also reconfirmed by the calculation within the BCS1 approach at finite temperature and angular momentum [48]. From the theoretical points of view, the pairing reentrance in atomic nuclei can be predicted via the behavior of calculated pairing gaps. However, from the experimental side, it is not simple, if not at all feasible, to extract the thermal pairing gap because of the admixture of uncorrelated single-particle configurations, which should be properly excluded from the extension of the formula for the odd–even mass difference [40].

Meanwhile, the heat capacity can be extracted from the experimental level densities by interpolating the level density data up to a very high excitation energy of about 100 MeV using the phenomenological back-shifted Fermi gas formula [49–51]. Consequently, the existence of a bump or an *S*-shape on the curve of the heat capacity around the critical temperature was observed, which allows us to discuss the smoothing of the transition from the superfluid phase to the normal one in hot nuclei. The recent calculation within the shell-model Monte-Carlo method (SMMC) for the heat capacity of a heated rotating  $^{72}\text{Ge}$  nucleus has shown that there appears a local dip in the heat capacity at a rotational frequency of 0.5 MeV and temperature  $T \sim 0.45$  MeV, and a local maximum on the temperature dependence of the logarithm of level density is observed at the same rotational frequency and temperature [52]. These irregularities in the heat capacity and level density are associated with the signatures of the pairing reentrance. The results obtained within the BCS1 at finite temperature and angular momentum for the same  $^{72}\text{Ge}$  nucleus [53] agree with the SMMC prediction for the local minimum in heat capacity, however, no pronounced local maximum in the temperature-dependent level density is seen in this calculation. At the same time, pairing reentrance is seen in the proton pairing gap in [53], whereas this effect is claimed in the neutron pairing energy in [52]. This difference might occur because of using the same single-particle spectra for both protons and neutrons in [52], that is, neglecting the Coulomb interaction in the SMMC calculation, as has been pointed out in [53]. The detection of pairing reentrance phenomenon is therefore still under question. Very recently, in a series of experiments carried out for the reaction  $^{12}\text{C} + ^{93}\text{Nb} \rightarrow ^{105}\text{Ag}^* \rightarrow ^{104}\text{Pd}^* + p$  at the incident energy of 40–50 MeV [54–58], an enhancement of level density has been observed in  $^{104}\text{Pd}$  nucleus at low excitation energy (temperature) and high angular momentum, which is quantitatively similar to that reported in [52]. Immediately after that, the analysis of the BCS1 at finite temperature and angular momentum was carried out for the same warm rotating  $^{104}\text{Pd}$  nucleus and the results obtained for the level density agree quite well with the observed data, indicating the first evidence of pairing reentrance phenomenon in this nucleus [59, 60].

The present review summarizes the recent studies on the pairing properties in finite systems, focusing on excited nuclei, that is at finite temperature and/or angular momentum. The review is organized as follows. Section 2 introduces the

pairing properties based on the BCS Hamiltonian within a simple uniform model. The phase diagram boundaries of the paired regions with the associated phase transitions such as the first-order and second-order ones in the cases with fixed total angular momentum, fixed quasiparticle number, and fixed energy will be discussed in detail. The treatments of nuclear pairing problem within the grand canonical, canonical, and microcanonical ensembles by using several theoretical approaches will be discussed in sections 3 and 4. Section 5 presents the experimental evidences of the pairing reentrance in hot rotating nuclei and solid-state counterpart under a strong magnetic field. The role of pairing in the properties of excited nuclei such as giant dipole resonance, total nuclear level density, and radiative strength function will be highlighted in section 6. The review is summarized in the last section, where conclusions are drawn and an outlook is given.

## 2. Pairing within the uniform model

### 2.1. BCS Hamiltonian within the grand canonical ensemble at fixed angular momentum

**2.1.1. General theory.** We shall calculate all the statistical nuclear properties using an arbitrary shell-model level sequence, including pairing and angular momentum within a generalized BCS Hamiltonian. The standard procedure usually consists of restricting the grand partition function of the system with the constraints to conserve energy, number of particles, and, in general, any other first integral of motion. However, only the first integrals that are expansible in terms of sums over single-particle states can be easily handled in this way. Regarding the total angular momentum, only its *z*-projection *M* has this property. Therefore the following calculations are restricted to a constant angular momentum *z*-projection *M*. Such a procedure is justified and the formalism is complete in most of cases as will be shown in this section.

The pairing Hamiltonian *H* of a Fermi gas with an attractive and constant pairing interaction has the following form in the second quantization [14]

$$H = \sum_{\pm k} \epsilon_k a_k^\dagger a_k - G \sum_{kk'} a_{-k'}^\dagger a_k^\dagger a_k a_{-k}, \quad (1)$$

where  $\epsilon_k$  are the single-particle energies;  $a_k^\dagger$  and  $a_k$  are the particle creation and annihilation operators; and *G* is the pairing strength. Here, for simplicity, the subscripts *k* denote the single-particle states  $|k, m_k\rangle$  in the deformed basis with positive single-particle spin projection  $m_k$ , whereas those with  $-k$  stand for the time-reversal states  $|k, -m_k\rangle$ . Including the constraints on particle number and angular momentum, it is convenient to consider a modified Hamiltonian in the form [25]

$$H \rightarrow H - \lambda N - \gamma M, \quad (2)$$

where *N* is the particle number, *M* is the projection of the total angular momentum on a laboratory-fixed *z*-axis or on a body-fixed *z'*-axis, and  $\lambda$  and  $\gamma$  are two Lagrange multipliers to be determined. The quantities *N* and *M* are expressed in the operator forms as

$$N = \sum_{\pm k} a_k^\dagger a_k, \quad M = \sum_k m_k a_k^\dagger a_k - \sum_{-k} m_k a_{-k}^\dagger a_{-k}. \quad (3)$$

The Hamiltonian, modified as in (2), is then rewritten as

$$H = \sum_k \zeta_k^+ a_k^\dagger a_k + \sum_{-k} \zeta_{-k}^- a_{-k}^\dagger a_{-k} - G \sum_{kk'} a_{-k'}^\dagger a_{k'}^\dagger a_k a_{-k}, \quad (4)$$

where  $\zeta_k^+ = \epsilon_k - \lambda - \gamma m_k$  and  $\zeta_k^- = \epsilon_k - \lambda + \gamma m_k$ . Such Hamiltonian can be approximately diagonalized by means of the Bogoliubov transformation [61, 62]

$$a_k^\dagger = u_k \alpha_k^\dagger + v_k \alpha_{-k}, \quad a_{-k} = u_k \alpha_{-k} - v_k \alpha_k^\dagger, \quad (5)$$

where  $\alpha_k^\dagger$  and  $\alpha_{-k}$  are the quasiparticle creation and destruction operators, respectively, whereas  $u_k$  and  $v_k$  are the Bogoliubov's coefficients satisfying the normalization condition  $u_k^2 + v_k^2 = 1$ .

By substituting (5) in (4) and retaining only the diagonal terms, one obtains

$$H = \sum v_k^2 (\zeta_k^+ + \zeta_k^-) + \sum n_k^+ (\zeta_k^+ u_k^2 + \zeta_k^- v_k^2) + \sum n_k^- (\zeta_k^- u_k^2 + \zeta_k^+ v_k^2) - G \left[ \sum_{kk'} u_k v_k (1 - n_k^+ - n_k^-) \right]^2, \quad (6)$$

where  $n_k^\pm = \alpha_{\pm k}^\dagger \alpha_{\pm k}$  are the quasiparticle occupation numbers. Minimizing (6) with respect to  $u_k$  and keeping  $n_k^+$  and  $n_k^-$  constant, one obtains the Hamiltonian

$$H = \sum (\epsilon_k - \lambda - E_k) + \sum n_k^+ (E_k - \gamma m_k) + \sum n_k^- (E_k + \gamma m_k) + \frac{\Delta^2}{G}, \quad (7)$$

and the gap equation

$$\frac{2}{G} = \sum \frac{1 - n_k^+ - n_k^-}{E_k}, \quad (8)$$

with  $E_k = \sqrt{(\epsilon_k - \lambda - Gv_k^2)^2 + \Delta^2}$  being the quasiparticle energies [25].

The grand partition function  $\Omega$  can be directly obtained from the Hamiltonian (2) by using the relation  $e^\Omega = \text{Tre}^{-\beta H}$ . It is now given as

$$\Omega = -\beta \sum (\epsilon_k - \lambda - E_k) + \sum \ln\{1 + \exp[-\beta(E_k - \gamma m_k)]\} + \sum \ln\{1 + \exp[-\beta(E_k + \gamma m_k)]\} - \beta \frac{\Delta^2}{G}. \quad (9)$$

The gap equation, which relates the quantities  $\Delta$ ,  $\beta$ , and  $\gamma$ , takes now the form

$$f(\Delta, \beta, \lambda, \gamma) = \sum \frac{1}{2E_k} \left[ \tanh \frac{1}{2} \beta (E_k - \gamma m_k) + \tanh \frac{1}{2} \beta (E_k + \gamma m_k) \right] = \frac{2}{G}. \quad (10)$$

**2.1.2. Level density and statistical quantities.** The level density is defined as the inverse Laplace transform of the grand partition function [26]

$$\rho(E, N, M) = \left( \frac{1}{2\pi i} \right)^3 \oint d\beta \oint d\alpha \oint d\mu e^S, \quad (11)$$

where

$$\alpha = \beta\lambda, \quad \mu = \beta\gamma, \quad S = \Omega - \alpha N - \mu M + \beta E. \quad (12)$$

This integral can be evaluated with good approximation at the saddle point of the exponent  $S$ , which is located at

$$N = \frac{\partial \Omega}{\partial \alpha}, \quad M = \frac{\partial \Omega}{\partial \mu}, \quad E = -\frac{\partial \Omega}{\partial \beta}. \quad (13)$$

This leads to the level density in the form

$$\rho(E, N, M) = \frac{e^S}{(2\pi)^{\frac{3}{2}} D^{\frac{1}{2}}}, \quad (14)$$

where

$$D = \begin{vmatrix} \frac{\partial^2 \Omega}{\partial \alpha^2} & \frac{\partial^2 \Omega}{\partial \alpha \partial \mu} & \frac{\partial^2 \Omega}{\partial \alpha \partial \beta} \\ \frac{\partial^2 \Omega}{\partial \mu \partial \alpha} & \frac{\partial^2 \Omega}{\partial \mu^2} & \frac{\partial^2 \Omega}{\partial \mu \partial \beta} \\ \frac{\partial^2 \Omega}{\partial \beta \partial \alpha} & \frac{\partial^2 \Omega}{\partial \beta \partial \mu} & \frac{\partial^2 \Omega}{\partial \beta^2} \end{vmatrix}, \quad (15)$$

with both  $S$  and  $D$  to be evaluated at the saddle point. From the saddle-point conditions (13), the first integrals of the system can be explicitly calculated

$$N = \sum \left[ 1 - \frac{\epsilon_k - \lambda}{2E_k} \left\{ \tanh \frac{1}{2} \beta (E_k - \gamma m_k) + \tanh \frac{1}{2} \beta (E_k + \gamma m_k) \right\} \right], \quad (16)$$

$$M = \sum m_k \left[ \frac{1}{1 + \exp[\beta(E_k - \gamma m_k)]} - \frac{1}{1 + \exp[\beta(E_k + \gamma m_k)]} \right], \quad (17)$$

$$E = \sum \epsilon_k \left[ 1 - \frac{\epsilon_k - \lambda}{2E_k} \left\{ \tanh \frac{1}{2} \beta (E_k - \gamma m_k) + \tanh \frac{1}{2} \beta (E_k + \gamma m_k) \right\} \right] - \frac{\Delta^2}{G}, \quad (18)$$

$$S = \sum \left[ \ln\{1 + \exp[-\beta(E_k - \gamma m_k)]\} + \ln\{1 + \exp[-\beta(E_k + \gamma m_k)]\} + \beta \sum \frac{E_k - \gamma m_k}{1 + \exp[\beta(E_k - \gamma m_k)]} + \beta \sum \frac{E_k + \gamma m_k}{1 + \exp[\beta(E_k + \gamma m_k)]} \right]. \quad (19)$$

The explicit form of second derivatives of  $\Omega$  in (15) is given, e.g. in [26].

## 2.2. Applications of the theory to the uniform model

**2.2.1. Single-particle model.** The model consists of equidistant doubly degenerate single-particle levels (Nilsson-like levels) with density  $g$  and constant angular momentum projection  $m_k = m$ . The levels are symmetrically located from both side of the chemical potential  $\lambda$ , which is set to zero at all temperatures (in general, within a non-symmetric model the chemical potential  $\lambda$  varies with the temperature). In the calculations discussed below when one is dealing with energy as a variable, the uniform model has been employed with the following parameters:  $g = 7 \text{ MeV}^{-1}$ ,  $\Delta_0 = 1.0 \text{ MeV}$ , and  $m = 2\hbar$  to mimic a heavy rare-earth nucleus ( $\Delta_0$  is the gap parameter at  $T = 0$  and  $M = 0$ ).

**2.2.2. Dependence of gap parameter upon angular momentum at zero temperature ( $\beta = \infty$ ).** Assuming the pairing correlation extending over an energy interval  $\pm\omega$  above and below the Fermi surface and transforming all the summations over the single-particle levels into integrals within the limits  $\pm\omega$ , one obtains from (10) the gap parameter at  $T = 0$  and  $M = 0$  as

$$\Delta_0 = \frac{\omega}{\sinh(1/gG)} \approx 2\omega \exp(-1/gG), \quad (gG \ll 1). \quad (20)$$

The dependence of  $\Delta$  upon  $M$  for  $T = 0$  is obtained by integrating (17)

$$\Delta = \Delta_0(1 - M/M_c)^{1/2}, \quad (21)$$

where

$$M_c = gm\Delta_0, \quad (22)$$

from which one immediately derives

$$\left(\frac{d\Delta}{dM}\right)_{M=0} = -\frac{1}{2gm}, \quad \lim_{M \rightarrow M_c} \frac{d\Delta}{dM} = -\infty. \quad (23)$$

The dependence of  $\Delta$  upon  $M$  in (21) is plotted in figure 1, which shows that the gap parameter, i.e. the pairing correlation, decreases with increasing  $M$  to vanish at a critical value  $M_c$ , determined by (22). Equation (23) expresses the slopes of  $\Delta = \Delta(M)$  for  $M = 0$  and  $M = M_c$ . The qualitative meaning of such results can be easily understood by considering the Hamiltonian (1), whose second term shows that, whenever a pair of particles is transferred from a filled level to an empty one, there is an energy gain  $G$ . The first term, of course, means that, in order to transfer a pair of particles from a level  $k$  to a level  $k'$ , one has to invest an amount of energy equal to  $2(\epsilon_{k'} - \epsilon_k)$ . In other words, the pairing interaction affects most the levels close to the Fermi surface. To generate angular momentum, one must break some of the pairs: the excitations arising in this way (quasiparticles) occupy the single-particle levels, which become unavailable (blocked) to the scattered pairs. Consequently, the pairing correlation decreases. When the angular momentum is sufficiently large, all the levels

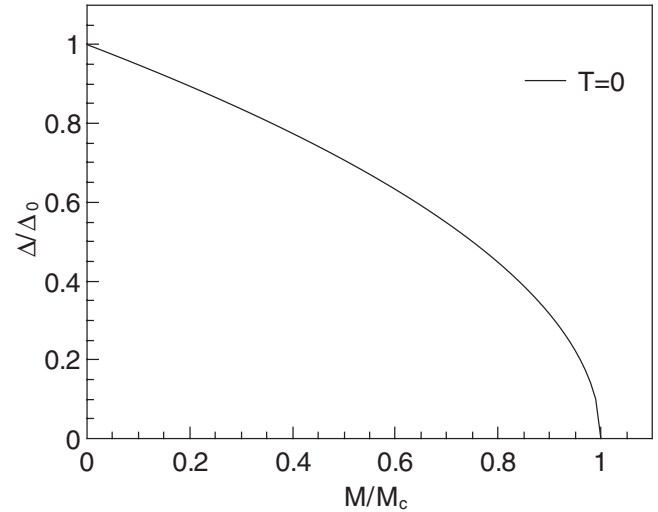


**Figure 1.** Dependence of the gap parameter  $\Delta$  upon the angular momentum  $M$  at zero temperature.  $\Delta_0$  is the gap parameter for  $T = 0$ ,  $M = 0$  and  $M_c$  is the critical angular momentum above which  $\Delta = 0$ . Adapted with permission from [26], Copyright (1972) by Elsevier.

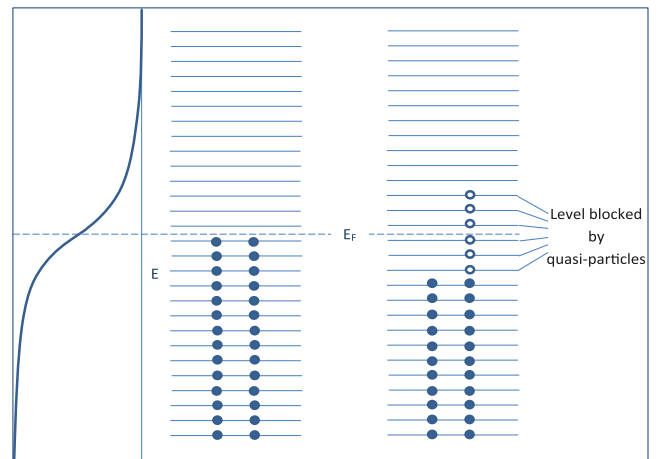


**Figure 2.** Schematic illustration of the effect of angular momentum on the pairing correlation. On the left the system has zero angular momentum. The black full circles represent the particles which occupy the doubly degenerate levels up to the Fermi level  $E_F$ . Pairing smears out the Fermi surface as indicated in the diagram on the outer left, where the occupation numbers are shown as a function of the single-particle energy. On the right, the system has a non-zero angular momentum, obtained by breaking pairs and by polarizing the resulting quasiparticles (open circles with arrow). The quasiparticles block single-particle levels which become unavailable for the pairing correlation. Adapted with permission from [26], Copyright (1972) by Elsevier.

around the Fermi one are blocked by quasiparticles, making the pairing correlation energetically unfavorable (figure 2).

**2.2.3. Dependence of gap parameter upon angular momentum and excitation energy.** In the absence of angular momentum ( $M = 0$ ), the gap equation (10) gives the dependence of  $\Delta$  upon  $T$  alone, which is shown in figure 3. The pairing correlation decreases with increasing  $T$  up to a critical temperature  $T_c$ , where  $\Delta = 0$  and the pairing correlation disappears altogether. The value of  $T_c$  is given by the relation

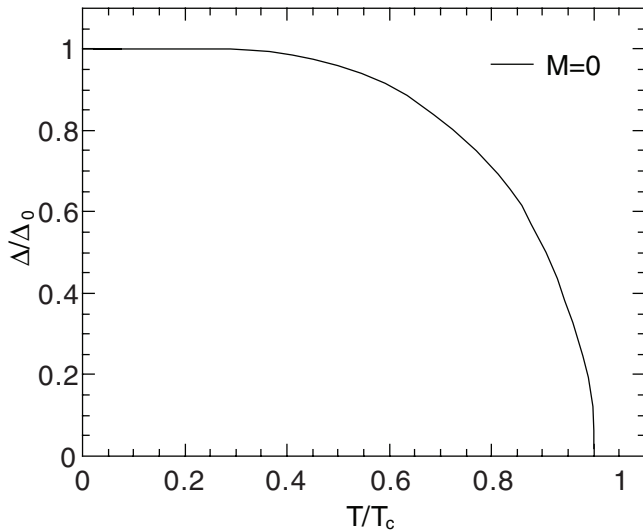


**Figure 3.** Dependence of the gap parameters  $\Delta$  upon the temperature  $T$  at zero angular momentum.  $T_c$  is the critical temperature above which  $\Delta = 0$ . Adapted with permission from [26], Copyright (1972) by Elsevier.

$T_c = 1.14\exp(-1/gG)$ , which consequently leads to the well-known relation [63]

$$\frac{2\Delta_0}{T_c} = 3.53. \quad (24)$$

Again the decrease of the pairing correlation with  $T$  (excitation energy) is caused by breaking particle pairs, which generate the quasiparticles, blocking the single-particle levels close to the Fermi surface. The combined effect of  $T$  and  $M$  can be seen by determining the dependence of the critical temperature upon the angular momentum projection  $M$ . Such a function defining the boundaries between the superfluid and the normal phase in the  $(M, T)$  plane is shown in figure 4. At  $0 \leq M < M_c$  the gap equation (10) yields a single solution for the critical temperature, which decreases with increasing  $M$  as expected. However, at  $M \geq M_c$ , the gap equation produces two critical temperatures: the upper one is the continuation of the curve obtained at  $M < M_c$ , while the lower one starts from zero at  $M = M_c$  and coalesces with the upper one at  $M = 1.22M_c$ . Surprisingly for  $M > M_c$ , the system is in the normal phase within the temperature range between zero and the lower critical temperature, whereas it is in the superfluid phase within the temperature range between the lower and the upper critical temperatures. Above the upper critical temperature, the system returns to its normal phase again. We are dealing here with an unexpected effect, namely for  $M > M_c$ , a system in the normal phase can become a superconductor by increasing its temperature or excitation energy. This is in dramatic contrast with the known case for  $M = 0$  (figure 3), where an increase in temperature destroys the pairing correlation. We call this effect ‘anomalous pairing’ or ‘thermally assisted pairing correlation’ because it is sustained by increasing temperature.

A qualitative insight into such a peculiar phenomenon can be gained as follows. As stated previously, the angular

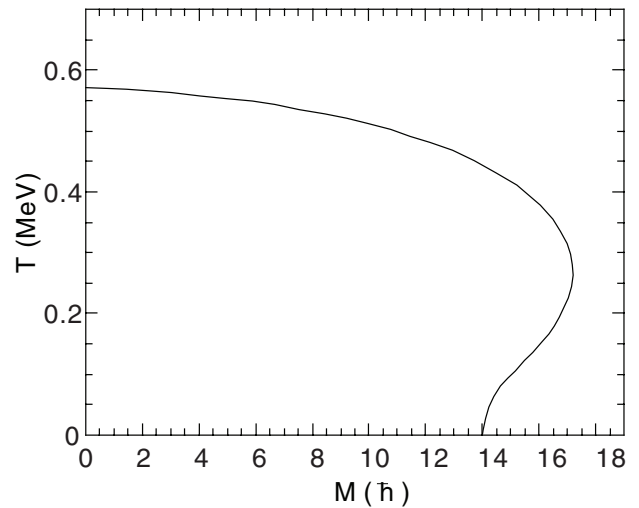


**Figure 4.** Dependence of the critical temperature upon angular momentum. The parameters are the same as in figure 3. Adapted with permission from [26], Copyright (1972) by Elsevier.

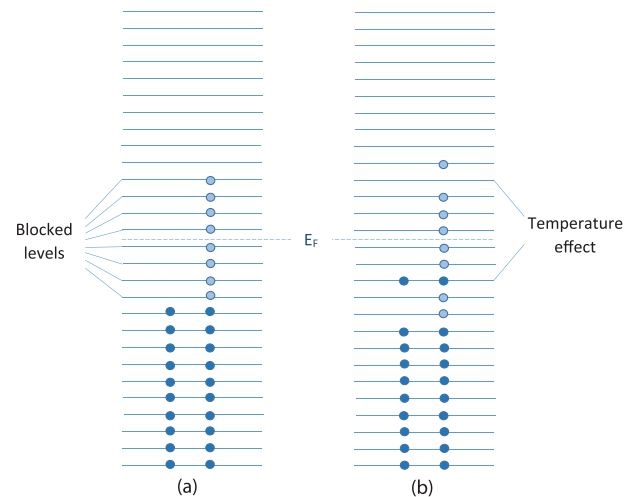


**Figure 5.** Explanation of the thermally assisted pairing correlation. (a) The temperature is zero and the angular momentum is generated by quasiparticles which are tightly packed around the Fermi surface: the pairing interaction finds the most effective levels blocked by quasiparticles. (b) A non-zero temperature spreads out the distribution of quasiparticles making more levels available for the pairing interaction. The result is a tendency of the gap parameter to increase with temperature for non-zero angular momentum. Adapted with permission from [26], Copyright (1972) by Elsevier.

momentum, generated by breaking pairs of particles, puts the quasiparticles into the single-particle levels close to the Fermi surface and polarizes their spins. At  $T = 0$ , a sufficiently high angular momentum causes a large number of quasiparticles completely occupying the closest levels around the Fermi surface. Such a complete blocking of single-particle levels makes the pairing correlation energetically unfavorable (figure 5(a)). Increasing temperature tends to relax the tight packing of quasiparticles by spreading them farther and farther away from the Fermi surface. Consequently, some single-particle levels become partially unoccupied and, therefore, become available

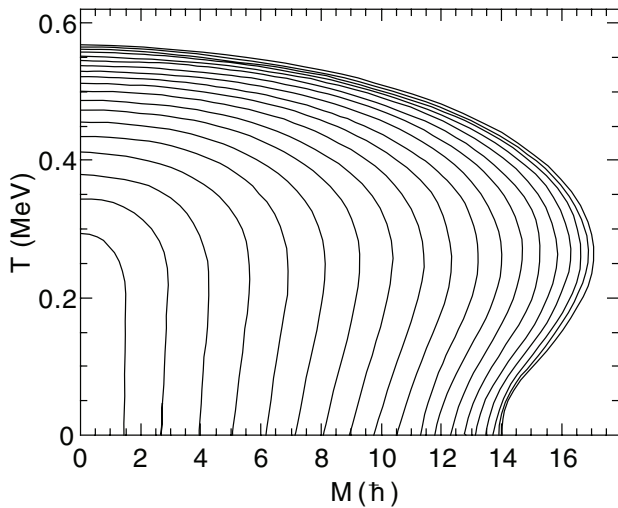


**Figure 6.** Contour map of the gap parameter as a function both of temperature and angular momentum. The spacing in  $\Delta$  between two successive lines is 0.05 MeV from  $\Delta = 1.0$  to  $\Delta = 0.1$  MeV. The outer line corresponds to  $\Delta = 0$ . Adapted with permission from [26], Copyright (1972) by Elsevier.

again for pairs scattered by the pairing interaction (figure 5(b)). At a temperature equal to the lower critical temperature, such a spreading out of quasiparticles is just sufficient to make the pairing correlation energetically favorable. A further increase of the temperature will increase the pairing correlation first but eventually produce the usual pairing breakdown by generating an increasingly large number of quasiparticles.

Such a remarkable effect persists also for values of  $M$  smaller than  $M_c$ , as can be clearly shown by calculating the dependence of the gap parameter  $\Delta$  upon temperature and angular momentum projection. To do so, we solve the set of two equations (10) and (17). In figure 6, the  $(T, M)$  plane is again divided into two regions, paired (superfluid) and normal. It appears that for a constant  $M$  value below  $M_c$ , the gap  $\Delta$  increases with  $T$ , reaches a maximum, decreases, and finally vanishes at the critical temperature. For  $M > M_c$ , the gap parameter  $\Delta$  stays equal to zero from  $T = 0$  up to the lower critical temperature. In the paired region,  $\Delta$  increases, goes through a maximum, decreases again, and vanishes at the upper critical temperature. Notice that  $\Delta$  goes through a maximum with increasing  $T$  for any non-zero value of  $M$ . This initial increase in  $\Delta$  with increasing  $T$  can also be called thermally assisted pairing correlation, but hardly can be called anomalous. The effect at  $M = 0$  could be called anomalous because only in such a case  $\Delta$  decreases monotonically with increasing temperature.

**2.2.4. Transition from temperature scale to energy scale.** The canonical ensemble has been used in statistical calculations for excited nuclei because of the development of more advanced algorithms. Thus, the calculations presented so far should be understood to hold at a fixed temperature. However, for the great majority of purposes, excited nuclei are considered with a fixed excitation energy rather than with a fixed temperature. Therefore, it is more common to speak of nuclei in terms of energy instead of temperature and use the microcanonical ensemble

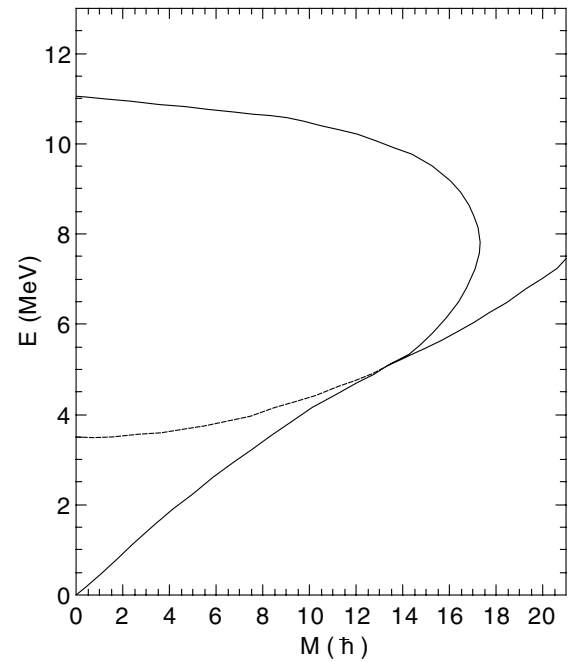


**Figure 7.** Critical energy (upper line) and yrast line (lower line) as a function of angular momentum. The dashed line, which merges into the yrast line at  $M = M_c$  is the yrast line for the unpaired system. The difference between the dashed line and the lower solid line represents the condensation energy due to pairing. Adapted with permission from [26], Copyright (1972) by Elsevier.

instead of the canonical ensemble in statistical calculations for nuclear systems. Even within the canonical ensemble, where the temperature is fixed and energy is allowed to fluctuate, it is possible to calculate the average energy associated with such a temperature. The main effect of such approximation is that of introducing some smoothing of the statistical quantities with respect to energy. The energy of the system at  $T = 0$  calculated as a function of  $M$  is called the yrast line and it is usually defined in a somewhat different fashion (like the function giving the highest angular momentum for a given energy or alternatively giving the lowest possible energy for a given angular momentum). For the uniform model, one obtains

$$E - E_0 = \frac{1}{2}g\Delta_0^2 \frac{M}{M_c} \left(2 - \frac{M}{2M_c}\right) \quad \text{for } M < M_c, \quad (25)$$

$$E - E_0 = \frac{1}{2}g\Delta_0^2 + \frac{M^2}{4m^2g} \quad \text{for } M > M_c, \quad (26)$$

where  $E_0$  is the ground-state energy, e.g. energy at  $T = 0$  and  $M = 0$ . The yrast line is shown in figure 7 (lower line) together with the critical energy as a function of  $M$  (upper line). These two curves, which join smoothly at  $M_c$ , define the region of superfluid phase. The dashed line, as the continuation of the yrast line given by (26) for  $M$  values lower than  $M_c$ , represents the yrast line corresponding to an uncorrelated Fermi gas. Such a line intersects the axis, at  $M = 0$ , at an energy equal to  $\frac{1}{2}g\Delta_0^2$ , which represents the condensation energy from the normal to the superfluid phase at  $M = 0$  and  $T = 0$ . The difference between the dashed line and the lower line represents the  $T = 0$  condensation energy as a function

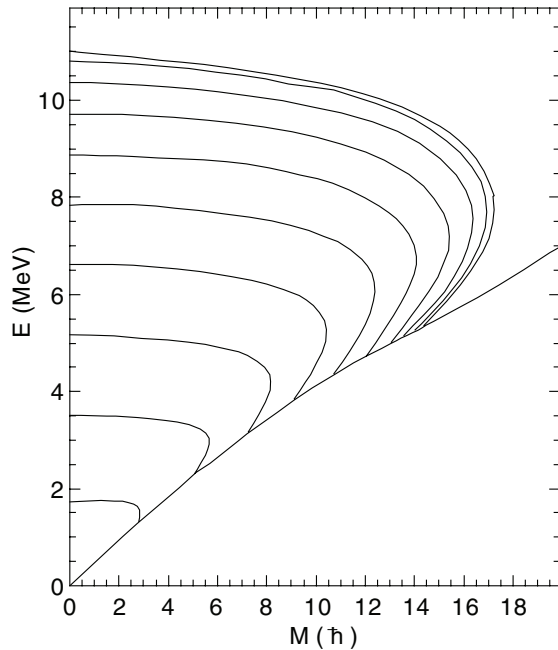


**Figure 8.** Same as in figure 7. The contour lines in the paired region correspond to the regions of equal  $\Delta$  from  $\Delta = 1$  MeV to  $\Delta = 0$  MeV in steps of 0.1 MeV. Adapted with permission from [26], Copyright (1972) by Elsevier.

of  $M$ . Such a condensation energy vanishes together with the pairing correlation at  $M = M_c$ .

As a final simple insight into the change from temperature to energy scale, figure 8, corresponding to figure 6, shows the lines of equal  $\Delta$ -value in the  $(E, M)$  plane. The superfluid region, where the inner lines are located, is bounded by the yrast and critical energy lines, as two outer lines.

**2.2.5. Entropy.** The pairing effects are also very relevant in the entropy expression. Shown in figure 9 is the entropy as a function of  $M$  at several temperatures  $T$ . In the absence of pairing and in particular for  $M$  and  $T$  above their critical values, the entropy, at fixed  $T$  does not depend upon  $M$ . This appears clearly in the right side of the figure, where the curves reduce to equally spaced straight lines parallel to the  $M$ -axis. Within the superfluid region, there is a general depression in the entropy values, the larger entropy the lower  $T$ . At the very low  $T$ , the entropy goes through a maximum.

**2.2.6. Level-density denominator.** As has already been observed for the pairing correlation at  $M = 0$  [63], the denominator of the level density undergoes a discontinuity at  $T_c$ . In particular, at  $M > M_c$ , where two discontinuities should exist with respect to the two values of the critical temperatures, corresponding to exceedingly small excitation energies, the validity of the saddle-point approximation is doubtful.

### 2.3. Completeness of formalism with respect to angular momentum

In the present formalism, only the first integrals can be easily handled by summing over single-particle levels. The energy, the particle number, and the  $z$ -projection  $M$  of the total angular

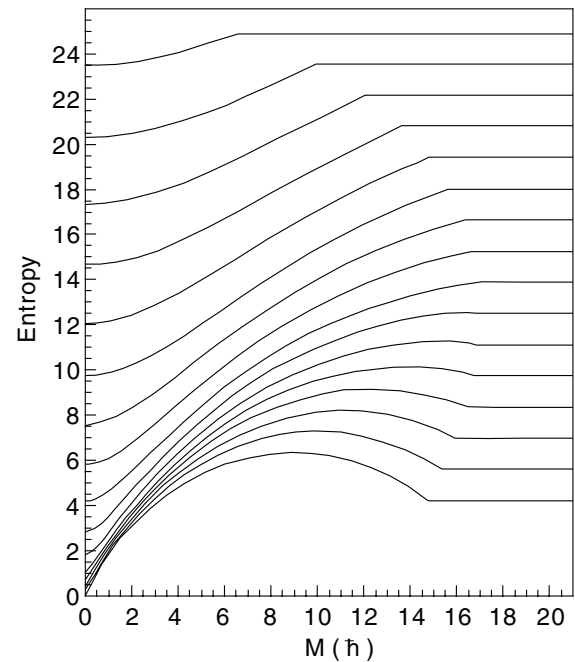


**Figure 9.** Entropy as a function of angular momentum at constant temperatures from  $T = 0.09$  MeV (lowest line) to  $T = 0.54$  MeV (highest line) in steps of 0.03 MeV. Adapted with permission from [26], Copyright (1972) by Elsevier.

momentum satisfy such a requirement, but not the total angular momentum  $J$ . An obvious lack of completeness in such a calculation can be seen, e.g. in the dependence of  $\Delta$  on  $M$  at  $T = 0$  (figure 6). As the choice of the  $z$ -axis is arbitrary, so is the  $M$  projection on such an axis. It is, therefore, unclear how the intrinsic properties of the system, like the pairing correlation, depend on the arbitrary choice of the  $z$ -axis. However, the formalism is essentially complete at least for a spherical (or quasi-spherical nucleus), where any axis can be taken as the symmetry one. It is quite obvious that, if the total momentum is not aligned with the  $z$ -axis, the present formalism accounts only for a part of the overall angular momentum effect. But, if the angular momentum is indeed aligned with the  $z$ -axis (and this can always be the case if a suitable choice of  $z$ -axis is made), then there is no angular momentum component left out, which may affect the intrinsic properties of the system. It follows that we can substitute the angular momentum in place of  $M$  in all the expression concerning intrinsic properties of the system. Such is the case for the expression giving  $\Delta$  as a function of  $M$  and  $T$ , for the yrast line expression, for the energy expression and so on [64, 65].

### 2.4. Effect of single-particle spin projection distribution upon the shape of the yrast line

As has been discussed, the uniform model with a constant spin projection distribution predicts a decreasing angular velocity (rotational frequency) with increasing angular momentum in the paired region. Consequently, the yrast line, which presents a negative second derivative and the moment of inertia as a function of the squared angular velocity, undergoes a back-bending. These effects strongly depend on the spin projection

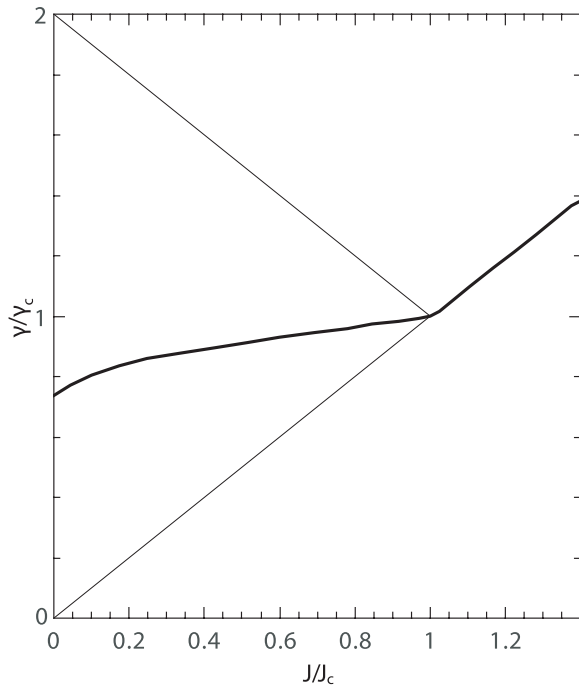


**Figure 10.** Angular velocity as a function of angular momentum for a rectangular distribution of spin projection (thick lines). The thin lines correspond to a  $\delta$ -distribution in spin projection. Adapted with permission from [67], Copyright (1974) by Elsevier.

distribution, whose version  $p(m')dm' = \delta(m' - m)dm'$  is not very realistic. In [66, 67], a rectangular distribution was employed as

$$p(m)dm = \begin{cases} g(dm/m_x), & \text{if } 0 \leq m \leq m_x, \\ 0, & \text{if } m \geq m_x, \end{cases} \quad (27)$$

which quite well approximates the  $2j + 1$  projection of a  $j$ -shell, and therefore is expected to be more realistic for a spherical nucleus. Here,  $m_x$  is the largest possible spin projection. For this distribution, it is also possible to carry out the analytic integration of the angular momentum and the gap equations.

Shown in figure 10 is the complete function  $\gamma = \gamma(J)$ , which monotonically increases with  $J$ , excluding the possibility of the back-bending with the critical angular momentum and the rigid moment of inertia given by  $J_c = \frac{1}{3}egm_x\Delta_0$  and  $\mathfrak{I}_R = \frac{2}{3}gm_x^2$ . The critical angular momentum predicted by the present model is larger than that given by the uniform model when the comparison at constant moment of inertia is made. The ratio  $R$  between the two critical angular momenta is  $R = (1/3)^{1/2}e$ . The yrast line, which is now expected to have a positive second derivative, can be calculated numerically. Its value at the critical angular momentum is

$$\begin{aligned} E_\gamma(J = J_c) &= \frac{1}{2}g\Delta_0^2 + \frac{J_c^2}{2\mathfrak{I}_R} \\ &= \frac{1}{2}g\Delta_0^2\left(1 + \frac{1}{6}e^2\right) \approx 2.23E_{\text{cond}}, \end{aligned} \quad (28)$$

where  $E_{\text{cond}} = \frac{1}{2}g\Delta_0^2$  is the condensation energy owing to pairing, in contrast with the uniform model, which predicts  $E_\gamma(J = J_c) = 1.5E_{\text{cond}}$  (see e.g. equation (32) of [67]). The

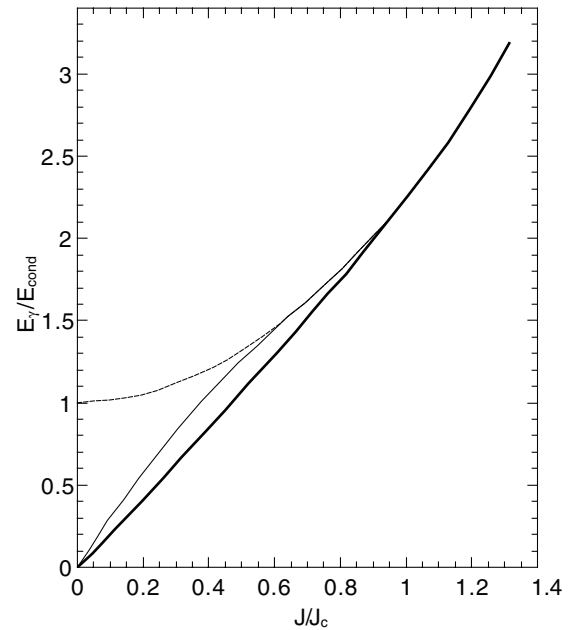


**Figure 11.** Various shapes of the yrast line for various models. The dashed line corresponds to a rigid moment of inertia. The thin line corresponds to a  $\delta$ -distribution in spin projections. The thick line corresponds to a rectangular distribution in spin projection. Adapted with permission from [67], Copyright (1974) by Elsevier.

complete yrast line, presented in figure 11, shows the expected small positive second derivative.

### 2.5. Transition from the constant spacing model to the shell model

While the uniform model brings forth the pairing features, this approximation may be oversimplified. Within this model, it has been shown how the yrast line changes dramatically by replacing the  $m$  distribution as a delta function picked at the average  $m$  with a rectangular distribution for  $0 \leq m \leq m_x$  at the same average value. More dramatic changes take place when the equally spaced single-particle levels are substituted with the shell model levels. Moving the Fermi surface from one degenerate level to another leads to the associated changes in the local single-particle level densities and spins, which dramatically affect the pairing correlation as a function of excitation energy and angular momentum.

Shown in figure 12 are the gap parameters for neutrons and protons as a function of temperature and angular momentum for the nucleus  $^{220}\text{Rn}$ . The figure shows that both temperature and angular momentum affect pairing, leading to a second-order phase transition line where the gap parameter vanishes. On the other hand, the thermally assisted pairing does not show up in the proton component and remains rather weak in the neutron one. In figure 13, the lines of constant entropy are shown in the  $(T, J)$  plane, where the difference between the proton and neutron components is more obvious. Here the second-order criticality line clearly shows a pairing reentrance for the neutron component but not for the proton one.

In figure 14 the line of constant level densities are shown in the  $(E, J)$  plane for the same nucleus as in figure 13. The yrast

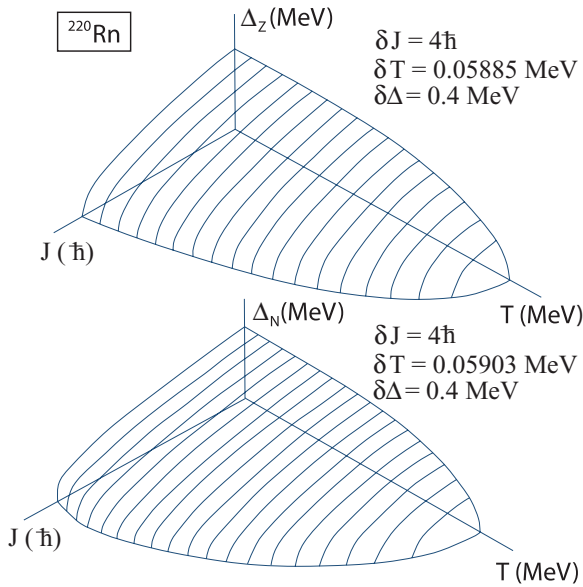


**Figure 12.** Isometric projections of the gap parameter as functions of temperature and angular momentum for the proton and neutron components of  $^{220}\text{Rn}$  nucleus. The magnitudes of the scale intervals in the three coordinates are indicated in the figures. Adapted with permission from [68], Copyright (1973) by Elsevier.

line, which has a weak positive second derivatives, shows a remarkable difference when it is compared with the previously mentioned result for a rectangular spin projection distribution. The difference in the dependence of the critical lines as a function of angular momentum is also visible.

### 2.6. Thermodynamic properties of paired nucleus with fixed number of quasiparticles

The study of relaxation phenomena in nuclei has been widely useful in the description of pre-equilibrium emission of nucleons [69–72]. However, one can also forecast many cases where the statistical properties of a fixed quasiparticle system may be of interest. For instance, the coupling of a doorway state (single-particle or collective in nature) with a certain class of particle-hole states needs to be considered in the description of its width. Various relevant thermodynamical quantities will be considered here as a function of the quasiparticle number by using the residual interaction in the form of the pairing approximation, having in mind that for the systems with unrestricted quasiparticle number, the residual interaction is very important only at low energy [62, 63, 73, 74]. It will be shown that, at small quasiparticle numbers, the pairing correlation is present even at very high excitation energies, which plays a dominant role during the relaxation process leading from a small quasiparticle number to its equilibrium value. The uniform model, which eliminates the shell effects associated with the fluctuations in the single-particle spacings, is employed to clearly identify the correlation between quasiparticle number and pairing.

**2.6.1. Hamiltonian.** The same form of pairing Hamiltonian  $H$  is used with a constant pairing interaction as in (1). To fix the

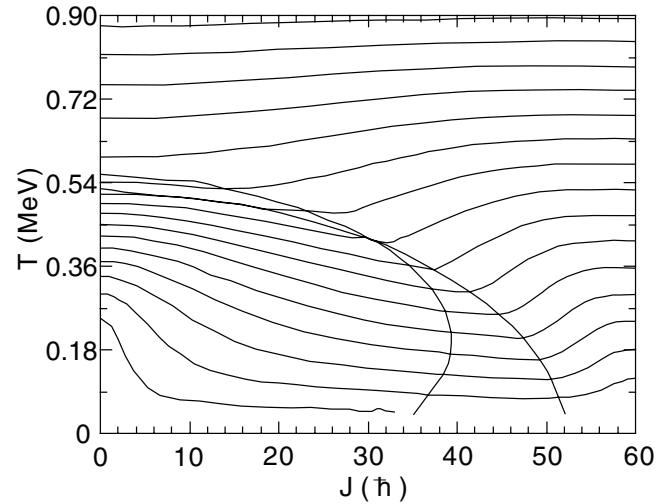


**Figure 13.** Lines of constant entropy in the  $(T, J)$  plane for  $^{220}\text{Rn}$  nucleus. The boundaries of the proton and neutron superfluid phases are also shown. The boundary of the superfluid proton component is the one extending farther to the right of the figure. The lowest value of the entropy and the entropy step are both equal to 2.5. Adapted with permission from [68], Copyright (1973) by Elsevier.

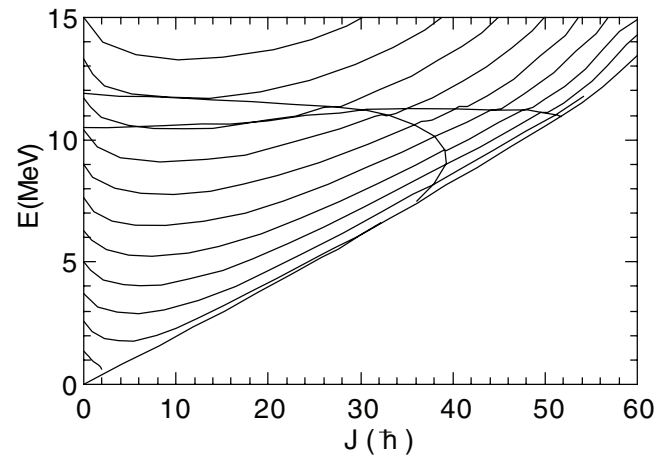


**Figure 14.** Lines of constant natural logarithm of the level density in the  $(E, J)$  plane for the same nucleus as in figure 13. The yrast line and the boundaries of the proton and neutron superfluid phases are also shown, which can be identified as in figure 13. The lowest value and the step of the natural logarithm of the level density are  $-0.25$  and  $0.25$ , respectively. Adapted with permission from [68], Copyright (1973) by Elsevier.

mean number of quasiparticle number, a new auxiliary Hamiltonian is introduced as  $H' = H - \xi Q$ , where  $Q = 2 \sum n_k$  is the quasiparticle number ( $n_k$  is the quasiparticle occupation number) and  $\xi$  is the Lagrange multiplier necessary for this particular constraint. The expectation value of the new Hamiltonian can be explicitly written as

$$H' = \sum (\epsilon_k - \lambda - E_k) + \frac{\Delta^2}{G} + 2 \sum n_k (E_k - \xi). \quad (29)$$

**2.6.2. Grand partition function and other thermodynamic quantities.** The grand partition function  $e^\Omega = \text{Tre}^{-\beta H'}$  can be immediately obtained from the Hamiltonian  $H'$  with

$$\Omega = -\beta \sum (\epsilon_k - \lambda - E_k) - \beta \frac{\Delta^2}{G} + 2 \sum \ln\{1 + \exp[-\beta(E_k - \xi)]\}. \quad (30)$$

All the other thermodynamical functions for the particle number  $N$ , quasiparticle number  $Q$ , energy  $E$ , pairing gap  $\Delta$ , and entropy  $S$  can be obtained by differentiating (30) [67, 75] as

$$N = \frac{1}{\beta} \frac{\partial \Omega}{\partial \lambda} = \sum \left[ 1 - \frac{\epsilon_k - \lambda}{E_k} \tanh \frac{1}{2} \beta (E_k - \xi) \right], \quad (31)$$

$$Q = \frac{1}{\beta} \frac{\partial \Omega}{\partial \xi} = 2 \sum \frac{1}{1 + \exp[\beta(E_k - \xi)]}, \quad (32)$$

$$E = -\frac{\partial \Omega}{\partial \beta} = \sum \epsilon_k \left[ 1 - \frac{\epsilon_k - \lambda}{E_k} \tanh \frac{1}{2} \beta (E_k - \xi) \right], \quad (33)$$

$$\frac{1}{E_k} \tanh \frac{1}{2} \beta (E_k - \xi) = \frac{G}{2}, \quad (34)$$

$$S = 2 \sum \ln\{1 + \exp[-\beta(E_k - \xi)]\} + 2\beta \sum \frac{E_k - \xi}{1 + \exp[\beta(E_k - \xi)]}. \quad (35)$$

In the graphs presented from here on, the gap parameter will be expressed in terms of the ground-state gap parameter  $\Delta_0$ ; the energy and free energy in units of the condensation energy  $C = g\Delta_0^2/2$ ; the temperature in terms of the critical temperature  $T_c = 2\Delta_0/3.5$ ; the quasiparticle number in terms of the most probable quasiparticle number at the critical temperature  $Q_c = 4gT_c \ln 2$ ; and the entropy in terms of the entropy at the critical point  $S_c = 2\pi^2 g T_c / 3$ .

### 2.6.3. Limiting properties for $T = 0$ ( $\beta \rightarrow \infty$ ).

**Gap equation.** In the limit of  $\beta \rightarrow \infty$ , the gap equation can be analytically integrated

$$\xi = \frac{1}{2} \sqrt{\frac{\Delta}{\Delta_0} (\Delta + \Delta_0)}. \quad (36)$$

**Quasiparticle number equation.** The equation for the quasiparticle number can also be analytically integrated in a similar way, giving

$$Q = 4g \sqrt{\xi^2 - \Delta^2}. \quad (37)$$

Combining the two equations (36) and (37), a relation between  $Q$  and  $\Delta$  is obtained as

$$Q = 2g \sqrt{\frac{\Delta}{\Delta_0} (\Delta + \Delta_0)}. \quad (38)$$

**Discussion on the phase stability.** Different from the regular dependences of  $\Delta$  on both temperature and angular momentum, the dependence of  $\Delta$  upon  $Q$  is anomalous. As shown

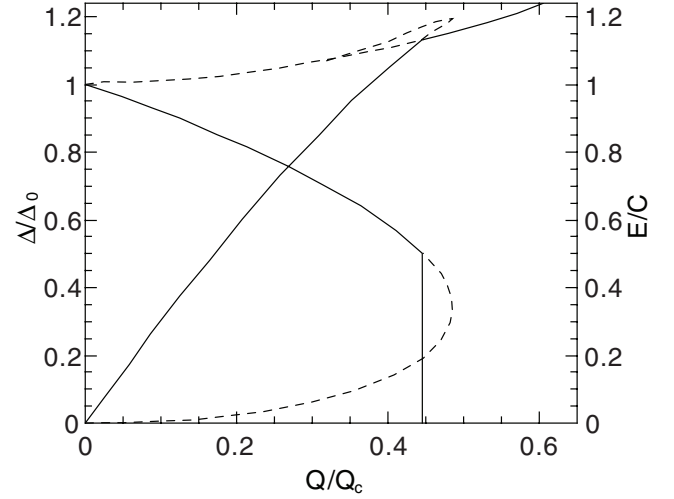


**Figure 15.** Dependence of the gap parameter  $\Delta$  and of the energy  $E$  upon quasiparticle number  $Q$  at  $T = 0$ . The dashed lines correspond to the unstable solutions. Adapted with permission from [75], Copyright (1975) by Elsevier.

in figure 15,  $\Delta$  is a triple valued function of  $Q$  with one trivial and two non-trivial solutions in the interval  $0 \leq Q \leq Q^*$ , where  $Q^* = \frac{4}{3} \sqrt{\frac{1}{3}} g \Delta_0$ , whereas it is single valued ( $\Delta = 0$ ) for  $Q > Q^*$ . Starting at  $\Delta = \Delta_0$  when  $Q = 0$ , the larger solution decreases as expected down to  $\Delta_0/3$  at  $Q = Q^*$ . Similarly, the smaller non-trivial solution starts at  $\Delta = 0$  for  $Q = 0$  and increases with  $Q$  to coalesce with the larger solution at  $Q = Q^*$ . This peculiarity must be resolved by deciding which of the three solutions is the stable one.

An immediate test on the two non-trivial solutions can be made by checking the sign of  $\partial^2 H' / \partial \Delta^2$ . One may recall that the gap equation, expressed by  $\partial H' / \partial \Delta = 0$ , represents the requirement that the Hamiltonian should be stationary with respect to  $\Delta$ . If  $\partial^2 H' / \partial \Delta^2$  is positive, then one has indeed a minimum, while a negative sign implies that the solution is a maximum. The second derivative calculated at the equilibrium value of  $\Delta$  is given as [67]

$$\frac{\partial^2 H'}{\partial \Delta^2} = \Delta^2 \sum \frac{1 - 2n_k}{E_k^3} - \Delta^4 \frac{G}{2} \left( \sum \frac{1 - 2n_k}{E_k^3} \right)^2. \quad (39)$$

By substituting  $n_k$  with its thermal average and considering the uniform model, one obtains

$$\frac{\partial^2 H'}{\partial \Delta^2} = 2g \left( 1 - 2 \frac{\Delta_0 - \Delta}{\Delta_0 + \Delta} \right). \quad (40)$$

This expression vanishes at  $\Delta = \Delta_0/3$ , which is the value of  $\Delta$  at which the larger and the smaller solutions merge. At  $\Delta > \Delta_0/3$  the second derivative is positive, thus indicating a stable solution, whereas for the values of  $\Delta < \Delta_0/3$  the second derivative is negative and the solution is unstable.

**Energy equation.** One must now decide which of the two remaining solutions, the paired or the trivial one ( $\Delta = 0$ ), is the stable solution. To do so, let us consider the energy equation, which in the limit of  $\beta \rightarrow \infty$  becomes

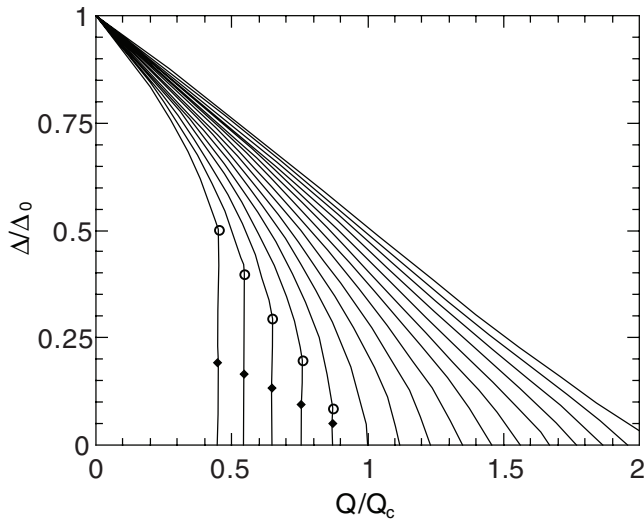


**Figure 16.** Dependence of the gap parameter  $\Delta$  upon quasiparticle number  $Q$  at various  $T$ . The inner isotherm corresponds to  $T/T_c = 0$ . The successive isotherms are space at intervals of  $0.2T/T_c$ . The onset of the first-order phase transition is indicated by an open circle, whereas the unstable solution at the same temperature is indicated by a solid point. Adapted with permission from [75], Copyright (1975) by Elsevier.

$$E = -gS^2 - \frac{1}{2}g\Delta^2 + 2g\xi\sqrt{\xi^2 - \Delta^2}. \quad (41)$$

By subtracting the ground state energy  $E_0 = -gS^2 - g\Delta_0^2/2$  and substituting  $\xi$  with its own expression, one obtains the excitation energy as

$$E^* = \frac{1}{2}g(\Delta_0^2 - \Delta^2)\left(1 + \frac{\Delta}{\Delta_0}\right) \quad \text{for } \Delta > 0, \quad (42)$$

$$E^* = \frac{1}{2}g\Delta_0^2 + \frac{Q^2}{8g} \quad \text{for } \Delta = 0. \quad (43)$$

*The unexpected existence of a first-order phase transition.* Shown in figure 15 is the excitation energy as a function of the quasiparticle number. As the gap parameter  $\Delta$  decreases from  $\Delta_0$  to 0, the energy follows a loop. As the stable solution is the one with the smallest energy, the loop must be bypassed. Since at the bypass point the curves for the paired and the unpaired energies cross. Thus the bypass coordinates can be obtained by equating these two energies  $E_{\text{paired}} = E_{\text{unpaired}}$  or

$$\frac{1}{2}g(\Delta_0^2 - \Delta^2)\left(1 + \frac{\Delta}{\Delta_0}\right) = \frac{1}{2}g\Delta_0^2 + \frac{Q^2}{8g}. \quad (44)$$

This equation gives  $\Delta_x/\Delta_0 = 1/2$ ,  $Q_x = g\Delta_0/\sqrt{2}$ , where  $\Delta_x$  and  $Q_x$  are the values of  $\Delta$  and  $Q$  at the crossing, respectively. The excitation energy at the crossing is  $E_x = (9/8)(g\Delta_0^2/2) = (9/8)C$ , where  $C$  is the pairing condensation energy. In conclusion, at  $Q < Q_x$  the paired solution is the stable one. At  $Q = Q_x$ ,  $\Delta$  decreases abruptly from  $\Delta_0/2$  to 0 and remains zero at  $Q > Q_x$ . This phase transition, clearly first order, is much sharper than the one occurring

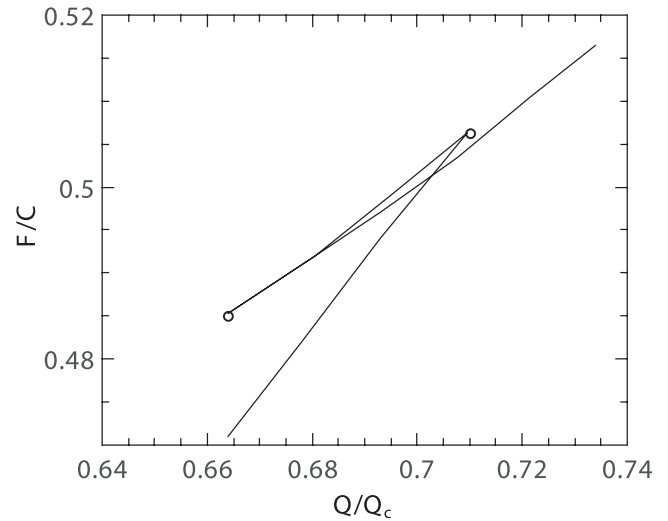


**Figure 17.** Example of an isothermal free energy loop. Adapted with permission from [75], Copyright (1975) by Elsevier.

at the critical angular momentum, where  $\Delta$  continuously decreases to 0, where the first derivative of  $\Delta$  undergoes a discontinuity.

#### 2.6.4. Properties of the system for $T > 0$ .

*Solution of the gap equation.* Shown in figure 16 is the dependence of the gap parameter  $\Delta$  on the quasiparticle number  $Q$  at various  $T$  obtained by simultaneously solving the equations for the gap and quasiparticle number. At  $T < T_c$  two paired solutions exist, whereas at  $T > T_c$  there is one paired solution. Aside from the bending over of the isotherms with  $T > T_c$  (similar to that in figure 15), it appears that the gap parameter at a fixed quasiparticle number actually increases with  $T$ . This is another example of the previously mentioned thermally assisted pairing correlation [26]. An increase in temperature pushes the quasiparticles farther and farther away from the particle Fermi surface, relaxing the blocking due to the quasiparticles and, hence, enhancing the pairing correlation. It follows that, for a fixed quasiparticle number, the pairing correlation is not confined to temperatures smaller than the critical one, but actually extends to indefinitely high temperatures.

*Free energy and phase stability.* In the region of  $T < T_c$ , two paired solutions (plus the usual unpaired solutions) appear. To determine which of the solutions corresponds to a stable system, the free energy  $F = -T\Omega + \xi\Omega$  is investigated, whose dependence upon  $Q$  at  $T < T_c$  is given in figure 17.

As for  $T = 0$ , a loop can be observed, which must be bypassed by the stable solution. This produces a discontinuous jump from the paired configuration with a larger  $\Delta$  to the unpaired configuration. This isothermal transition is accompanied by an energy change  $\Delta E = T\Delta S$ , indicating a true first-order phase transition. All of these isotherms present a minimum corresponding to the equilibrium value of  $Q$ , which satisfies the condition  $\partial F/\partial Q = \xi = 0$ . This means, when the number of quasiparticles is not restricted but is allowed to

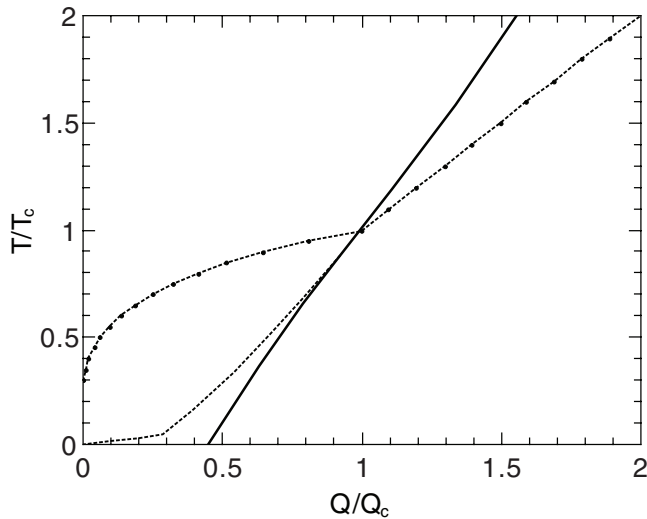


**Figure 18.** Phase diagram in the  $(T, Q)$  plane. The solid line corresponds to the phase transition (first-order for  $T < T_c$ , second-order for  $T > T_c$ ) from the paired region (left-hand side) to the unpaired region (right-hand side). The dotted line corresponds to the paired unstable solution. The line with small and large dots corresponds to the most probable value of  $Q(\xi = 0)$ . Adapted with permission from [75], Copyright (1975) by Elsevier.

attain its equilibrium value, the quasiparticle chemical potential is identically zero.

At  $T < T_c$ , the phase transition (first order) occurs for values of  $Q$  larger than the equilibrium value, whereas above  $T_c$ , the phase transition (now second order) occurs for values of  $Q$  smaller than the equilibrium value. This information can be used to generate a  $(T, Q)$  phase diagram, for example, the one shown in figure 18. This figure shows the boundary between the paired and the unpaired region defined by the vanishing of the gap parameter  $\Delta$ . At  $T < T_c$  this boundary branches into two lines. The leftmost line corresponds to the continuous vanishing of  $\Delta$ , which does not correspond to any stable system. The rightmost line corresponds to the discontinuous vanishing of  $\Delta$  and is physically significant. The line characterized by  $\xi = 0$ , corresponding to the equilibrium number of quasiparticles, starts at the origin of the diagram and stays into the paired region up to  $T_c$ , when it enters in the unpaired region. It is along this line that previous pairing calculations have been made [62, 63, 67, 68, 73, 74]. It is useful now to project various quantities on this basic diagram.

Shown in figure 19 are the projected lines of constant gap parameter  $\Delta$ . It is noticed that, firstly, the gap parameter at fixed  $Q$  actually increases and tends to reach its ground state value as  $T$  goes to infinity. Secondly, even for those values of  $Q$  for which  $\Delta = 0$  at  $T = 0$ , an increase in temperature eventually leads to the onset of pairing, which increases towards the ground state value as an asymptotic limit. These effects are completely understood in terms of the thermally assisted pairing correlation [26, 67, 68].

*The  $(E, Q)$  diagrams and the plots of various thermodynamical quantities.* The relevance of constant energy processes in nuclei makes it desirable to use the energy itself as an independent variable. Shown in figure 20 are the lines of constant

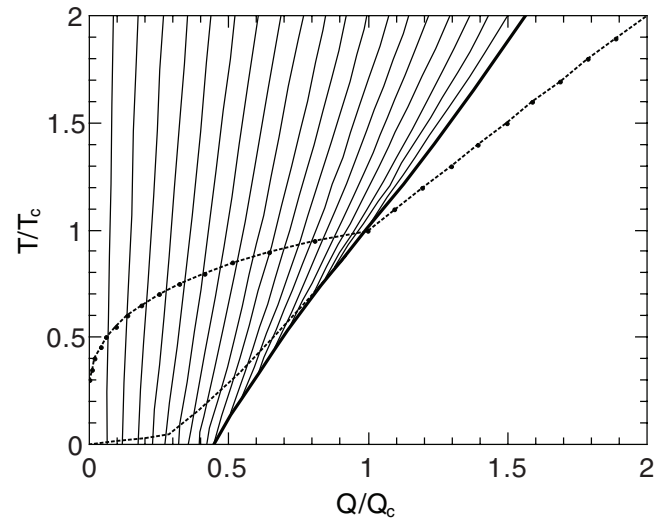


**Figure 19.** Lines of constant gap parameter in the  $(T, Q)$  plane. The solid line corresponds to  $\Delta = 0$ ; the lines to the left correspond to increasing values of  $\Delta$  in steps of  $0.05 \Delta/\Delta_0$ . Adapted with permission from [75], Copyright (1975) by Elsevier.

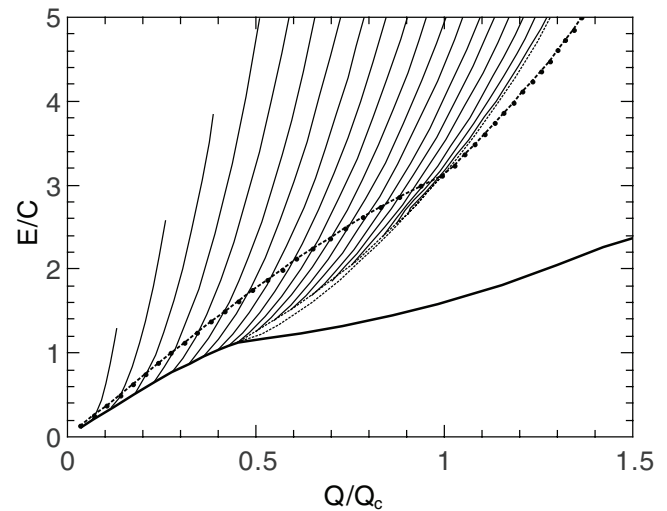


**Figure 20.** Lines of constant gap parameter  $\Delta$  in the  $(E, Q)$  plane. The leftmost line corresponds to  $\Delta/\Delta_0 = 0.05$  and the lines to the right are plotted in intervals of  $0.05 \Delta/\Delta_0$ . Adapted with permission from [75], Copyright (1975) by Elsevier.

$\Delta$  in the  $(E, Q)$  plane. The evolution in pairing of a constant energy system can be directly appreciated as it moves from a very low initial quasiparticle number to its equilibrium value. In all the cases of physical interest, the system starts off with a very large pairing gap, close to its ground state value. With increasing the quasiparticle number, the pairing correlation experiences rapidly drops and disappears above the critical energy. The first order phase transition appears as a gap between the two dotted lines.

*Level density.* Figure 21 shows the  $(E, Q)$  plot of the final result of the calculation for the level density, where constant level density lines for a system characterized by  $g = 7 \text{ MeV}^{-1}$  and  $\Delta_0 = 1 \text{ MeV}$  can be seen. The large gap in the plot is visible due to the first order phase transition.

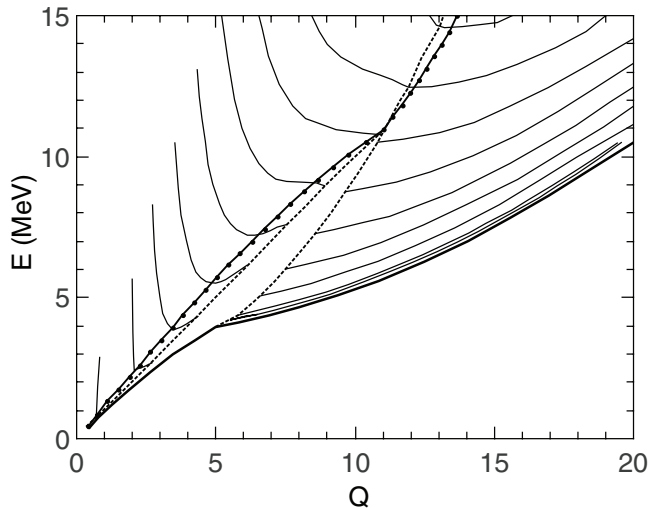


**Figure 21.** Lines of constant level densities in the  $(E, Q)$  plane. The calculation refers specifically to a nucleus with  $g = 7.0 \text{ MeV}^{-1}$  and with  $\Delta_0 = 1.0 \text{ MeV}$ . The lowest level density line has a value  $\ln \rho = 2.0$ . The higher lines are plotted in steps of  $3.0 \ln \rho$ . Adapted with permission from [75], Copyright (1975) by Elsevier.

### 2.7. Experimental level densities and first-order pairing phase transition

A large body of high-quality low-energy nuclear level-density data are now available in the literature. The stunning, common feature of the level densities, particularly evident for deformed, mid-shell nuclei, is the linear dependence of their logarithm with excitation energy. Above approximately  $2\Delta_0$ , and up to about the neutron separation energy, they are well described by the constant-temperature expression empirically proposed by Ericson [21], and Gilbert and Cameron [76]

$$\rho(E) \propto \exp(E/T), \quad (45)$$

with the excitation energy  $E$  and constant temperature  $T$ . This expression turns out to be in good agreement with the cumulative number of levels at low excitation energy. However, no fundamental nor quantitative explanation for this relation has been provided. Moreover, the constant-temperature expression is in striking contrast to the expected Fermi-gas behavior predicting a square-root dependence of the level density with excitation energy

$$\rho(E) \propto \exp[\sqrt{2aE}], \quad (46)$$

where  $a$  is the level-density parameter.

The experimental linear dependence of the entropy  $S(E) \approx \ln \rho(E)$  given by (45) is the microcanonical hallmark of first-order phase transitions. It implies a constant temperature, a latent heat and an infinite heat capacity. As a matter of fact, the experimental data for the rare-earth region [77–83] show that the entropies of adjacent even–even and odd- $A$  nuclei are parallel over the experimental energy range above 2 MeV, that is the level densities of neighboring even–even and odd- $A$  nuclei have nearly identical slopes [84, 85]. This feature allows one to coalesce the level densities of neighboring isotopes by making a horizontal shift along the excitation-energy axis (see figure 22). This shift is constant

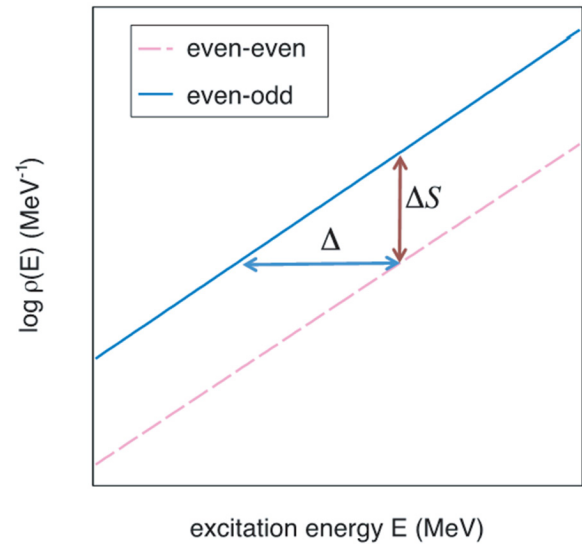


**Figure 22.** Illustration of constant-temperature level densities. The experimental, horizontal shift gives the slope  $(1/T_{CT})$  through (24), and the vertical shift is related to the entropy excess for the quasiparticle as indicated in the figure. Reprinted from [84]. Non-exclusive license to distribute 1.0.

with energy and in very good agreement with the even–odd mass difference, which identifies the elementary excitations as the quasiparticles. It implies that the energy cost per quasiparticle is constant and independent of excitation energy.

Equally intriguing is the vertical shift between the even–even and odd- $A$  nuclear level densities, merging the lower even–even level density and the higher odd- $A$  one (see figure 22). This difference, approximately constant for excitation energies above approximately 2 MeV, can be interpreted as the entropy carried by the extra quasiparticle. Thus, the experimental evidence alone suggests that, as the system is excited, quasiparticles are created with a constant energy cost and carrying a constant amount of entropy. This theory-independent observation is a clear signature of a first-order phase transition [84, 85]. As will be seen below, the two phases are a superfluid phase and an ideal gas of quasiparticles. Hence, the experimental data have a thermodynamic interpretation as that of a clear first-order phase transition with latent heat  $\Delta$  per (quasi)particle, infinite heat capacity, and a fixed amount of entropy per (quasi)particle. This interpretation follows from straightforward thermodynamics, without recouring to any specific nuclear structure theory.

The phase transition is, at least for nuclei well away from closed shells, clearly related to pairing. First of all, the constant shift  $\Delta$  is directly related to the liquid drop mass difference, which, in turn, arises from pairing. Furthermore, by provisionally taking the constant temperature of the experimental level-density spectrum to be the BCS critical temperature according to the well-known BCS relation (24), one can extract the gap parameter  $\Delta_0$  and compare it directly with that obtained from even–odd mass differences represented in the liquid-drop term, namely  $\Delta_{BM} = 12A^{-1/2}$ . From this observation, we can consequently predict the low-energy nuclear level densities from the even–odd mass difference throughout the nuclear chart for regions away from magic proton/neutron

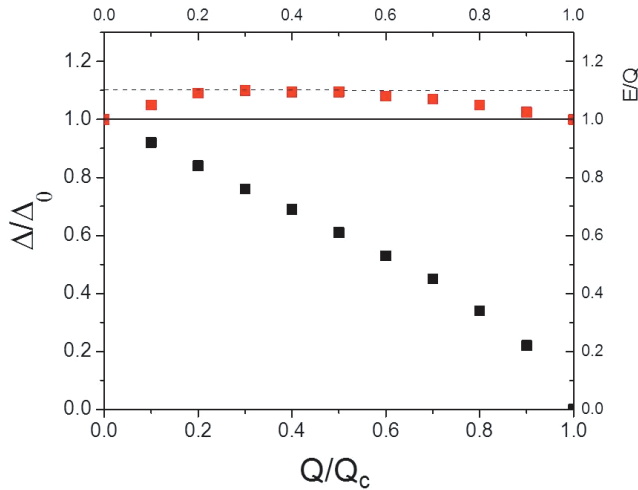


**Figure 23.** Average energy per quasiparticle as a function of the most probable quasiparticle number (see text). Adapted from [84]. Non-exclusive license to distribute 1.0.

numbers. From these features we can immediately infer that a first-order phase transition with a latent heat takes place at the constant temperature  $T_c$ .

We now show that all the empirical features find a close counterpart in the BCS theory. For a set of uniformly spaced single-particle levels, the excitation energy at  $T = T_c$  is given by  $E_c = g\Delta_0^2/2 + \pi^2 gT_c^2/3$ , whereas the most probable number of quasiparticles  $Q_c$  at  $T_c$  is  $Q_c = 4gT_c \ln 2$  [75]. Taking the ratio of these two quantities and utilizing (24), the average cost per created quasiparticle up to  $T_c$  is found as  $E_c/Q_c = \Delta_0$ . This very puzzling result is consistent with the parallel behavior of the level densities described above.

Within the BCS theory, we know that at  $T = 0$  the quasiparticle energy is approximately equal to  $\Delta_0$ , and that  $\Delta$  decreases with increasing temperature, so that  $\Delta = 0$  at  $T_c$ . How is it then possible for the energy per quasiparticle to be constant in this excitation-energy range? The explanation lies mostly in the structure of the quasiparticle energy  $E_k = \sqrt{(\epsilon_k - \lambda)^2 + \Delta^2}$ . With increasing  $T$ ,  $\Delta$  does indeed decrease, but within the uniform model this is compensated by the increase of the average value of  $|\epsilon_k - \lambda|$  and by the change of the underlying pairing field. For this case, we have calculated the average energy per quasiparticle  $E/Q$  as a function of the most probable quasiparticle number for  $1 < Q < Q_c$ . Figure 23 shows that the energy per quasiparticle is very close to 1 MeV in the entire region.

The assimilation of  $T$  with  $T_c$  finds also an explanation in the BCS model. The dependence of the heat capacity on  $T$  exponentially increases from zero and peaks at  $T = T_c$  so that essentially all energy is absorbed at this temperature. This is also true from a microcanonical perspective. From the constant energy cost  $\Delta$  per quasiparticle, it follows that the entropy per quasiparticle is

$$\frac{\partial S}{\partial Q} = \frac{\Delta}{T_c} = \frac{3.53}{2} = 1.77, \quad (47)$$

to be compared with the empirical, vertical shift as discussed above.

The consideration above is based on the BCS theory, which should be revised when applied to finite systems such as nuclei, taking care of large fluctuations owing to the finiteness of the system. In this case the sharp superfluid-normal phase transition is smoothed out and it is not possible to identify a critical temperature  $T_c$ . As will be seen later in section 6.2, a microscopic approach including exact pairing is necessary to explain the constant-temperature level density at low excitation energy as well as its Fermi-gas behavior at high excitation energy.

### 3. Grand-canonical ensemble treatment of pairing problem within the Hartree–Fock–Bogoliubov theory and finite-temperature pairing reentrance

#### 3.1. Hartree–Fock–Bogoliubov theory for hot and hot rotating nuclei

The Hartree–Fock–Bogoliubov theory at finite temperature (HFB) was first derived by Goodman in [33]. This theory, which is generalized from the BCS theory discussed in section 2, is derived based on the same minimization requirement of the grand potential as the BCS theory, namely  $\delta\Omega = 0$ , where  $\Omega = E - TS - \lambda N$  with  $E$ ,  $S$ ,  $\lambda$ , and  $N$  being the total energy, entropy, chemical potential, and particle number. This variational condition leads to the density operator  $\mathcal{D}$  given in the form

$$\mathcal{D} = \frac{1}{Z} e^{-\beta(H - \lambda\hat{N})}, \quad (48)$$

whose trace should satisfy the unitarity condition  $\text{Tr}\mathcal{D} = 1$  and  $\partial\Omega/\partial\mathcal{D} = 0$ . In (48),  $Z = \text{Tr}[e^{-\beta(H - \lambda\hat{N})}]$  is the grand partition function with  $H$  being the nuclear many-body Hamiltonian of the form

$$H = \sum_{ij} \mathcal{T}_{ij} a_i^\dagger a_j + \frac{1}{4} \sum_{ijkl} \mathcal{V}_{ijkl} a_i^\dagger a_j^\dagger a_l a_k, \quad (49)$$

where  $\mathcal{T}_{ij}$  is the kinetic energy operator and  $\mathcal{V}_{ijkl}$  is the anti-symmetrized matrix elements of the two-body interaction. Within the HFB, the Hamiltonian (49) is often expressed in terms of the independent-quasiparticle Hamiltonian  $H_{\text{HFB}}$ , namely

$$H - \lambda\hat{N} \approx H_{\text{HFB}} = E_0 + \sum_i E_i \alpha_i^\dagger \alpha_i, \quad (50)$$

where  $E_0$  is the ground-state energy,  $E_i$  is energy of the quasiparticle, and  $\alpha_i^\dagger(\alpha_i)$  is the quasiparticle creation (destruction) operator obtained from the Bogoliubov transformation. The latter is expressed in terms of a matrix form

$$\begin{pmatrix} \alpha^\dagger \\ \alpha \end{pmatrix} = \begin{pmatrix} U & V \\ V^* & U^* \end{pmatrix} \begin{pmatrix} a^\dagger \\ a \end{pmatrix}, \quad (51)$$

where the coefficients  $U$  and  $V$  of the Bogoliubov transformation must satisfy the conditions  $UU^\dagger + VV^\dagger = \mathbf{1}$  and

$UV^T = VU^T = 0$  with  $\mathbf{1}$  being the unit matrix and  $T$  denoting the transposing operation. The average within the grand canonical ensemble for any operator  $\hat{O}$  is then given as  $\langle \hat{O} \rangle = \text{Tr}(\mathcal{D}\hat{O})$ . The quantities such as total energy  $E$ , entropy  $S$ , and particle number  $N$  are calculated within the grand canonical ensemble as  $E = \langle H \rangle = \text{Tr}(\mathcal{D}H)$ ,  $S = -\langle \mathcal{D} \ln \mathcal{D} \rangle = -\text{Tr}(\mathcal{D} \ln \mathcal{D})$ , and  $N = \langle \hat{N} \rangle = \text{Tr}(\mathcal{D}\hat{N})$ .

The HFB theory approximates the density operator (48) within the independent-quasiparticle picture [37], that is,

$$\mathcal{D} \approx \mathcal{D}_{\text{HFB}} = \prod_k [n_i \hat{\mathcal{N}}_i + (1 - n_i)(1 - \hat{\mathcal{N}}_i)], \quad (52)$$

where  $\hat{\mathcal{N}}_i = \alpha_i$  is the quasiparticle-number operator and  $n_i = \langle \hat{\mathcal{N}}_i \rangle = [\exp(\beta E_i) + 1]^{-1}$  is the quasiparticle-occupation number. Consequently, the grand-canonical ensemble average is calculated using this approximated density, namely  $\langle \hat{O} \rangle = \text{Tr}(\mathcal{D}_{\text{HFB}}\hat{O})$ . Details of the derivation of the HFB can be found, e.g. in [33] or [37]. The final form of the HFB equations is given as

$$\begin{pmatrix} \mathcal{H} & \Delta \\ -\Delta^* & -\mathcal{H}^* \end{pmatrix} \begin{pmatrix} U_i \\ V_i \end{pmatrix} = E_i \begin{pmatrix} U_i \\ V_i \end{pmatrix}, \quad (53)$$

where  $\mathcal{H} = \mathcal{T} - \lambda + \Gamma$ ,  $\Gamma_{ij} = \sum_{kl} v_{ijkl} \rho_{lk}$  and  $\Delta_{ij} = \frac{1}{2} \sum_{kl} v_{ijkl} \kappa_{kl}$  with the single-particle density matrix  $\rho$  and pairing tensor  $\kappa$  being defined within the HFB as  $\rho_{ij} = \langle a_j^\dagger a_i \rangle = \text{Tr}(\mathcal{D}_{\text{HFB}} a_j^\dagger a_i)$  and  $\kappa_{ij} = \langle a_j a_i \rangle = \text{Tr}(\mathcal{D}_{\text{HFB}} a_j a_i)$ , respectively. Finally, the total energy  $E$ , particle number  $N$ , and entropy  $S$  are now given as

$$E = \text{Tr}[(\mathcal{T} + \frac{1}{2}\Gamma)\rho + \frac{1}{2}\Delta\kappa^\dagger], \quad N = \text{Tr}\rho, \quad (54)$$

$$S = - \sum_i [n_i \ln n_i + (1 - n_i) \ln(1 - n_i)]. \quad (55)$$

In the limit of the pairing Hamiltonian (1) where  $v_{kk'k'} = -G_{kk'} = -G$ , one recovers from the HFB equations (53) the conventional BCS ones.

The HFB theory was successfully applied to study thermal shape transitions as well as properties of some excited rare-earth nuclei such as  $^{148}\text{Sm}$ ,  $^{170}\text{Er}$ ,  $^{186,188}\text{Os}$ , etc [86]. Figures 24 and 25 show an example of the HFB calculation for an excited  $^{170}\text{Er}$  nucleus. In this calculation, by using the pairing-plus-quadrupole Hamiltonian of Kumar and Baranger [87, 88] with the constant values of pairing interaction strengths for proton and neutron and deformed harmonic oscillators with two deformation parameters  $\beta$  and  $\gamma$ , the temperature-dependent deformation free energy  $F_{\text{def}}(T, \beta, \gamma) = F(T, \beta, \gamma) - F(T, 0, 0)$ , where  $F = E - TS$  was calculated within the HFB. The minima of the obtained free energy curve were used to determine the values of  $\beta$  (see e.g. figure 24(a)). Consequently, the evolution of the shape transition with temperature characterized by  $\beta$  was examined and shown in figure 24(b). This figure 24(b) indicated that the equilibrium deformation decreases with temperature and there appears a second-order phase transition from a deformed shape to a spherical one at a temperature of 1.81 MeV, regardless of its initial oblate or prolate shape. Moreover, the value of  $\beta$  increases slightly with  $T \leq 0.6$  MeV

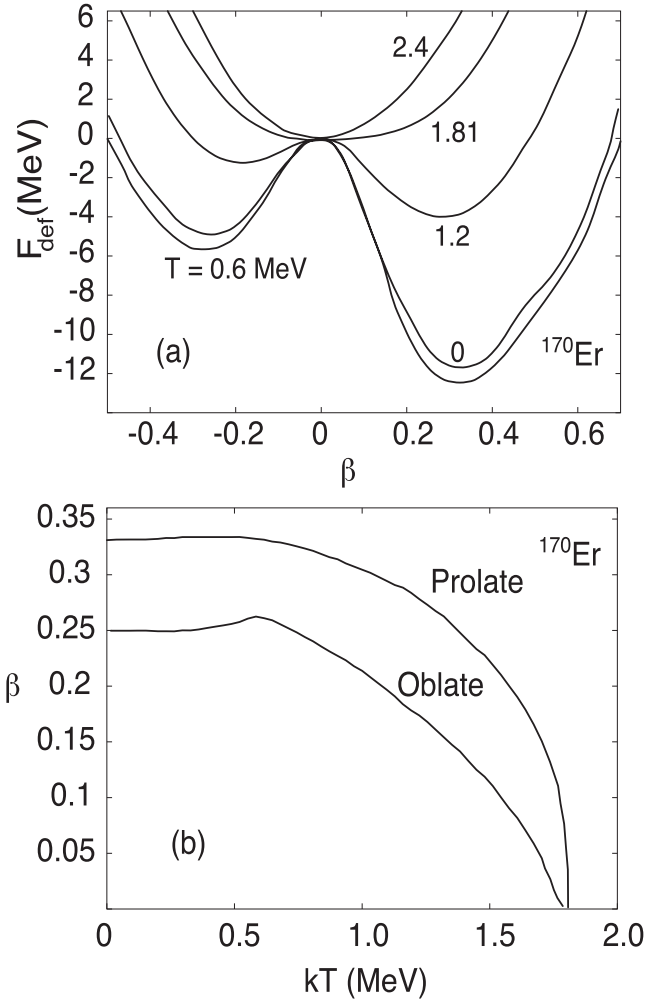


**Figure 24.** (a) Free energy curve versus quadrupole deformation  $\beta$  at different temperatures obtained within the HFB calculation for  $^{170}\text{Er}$ . (b) Quadrupole deformation  $\beta$  versus temperature obtained within the HFB calculation for the prolate and oblate shapes in  $^{170}\text{Er}$ . Adapted with permission from [86], Copyright (1986) by the American Physical Society.

as shown in figure 24(b), whereas it decreases at  $T > 0.6$  MeV. This effect is due to the behavior of neutron and proton pairing gaps as shown in figure 25(a). It is seen in figure 25(a) that the pairing gaps decrease with  $T$  and collapse at the critical temperatures of 0.39 MeV and 0.47 MeV for neutron and proton, respectively. The vanishing of the pairing gaps can be seen clearly via the sharp peaks in the heat capacity around these critical temperatures (figure 25(b)). These peaks are the signature of the superfluid-normal (second-order) phase transition. In figure 25(b), there appears additional sharp peak in the heat capacity at the transition temperature  $T = 1.81$  MeV, where the nucleus becomes spherical shape. This is another second-order phase transition observed in  $^{170}\text{Er}$  nucleus. Similar feature was seen in  $^{186,188}\text{Os}$  in [86].

Recently, the HFB with effective Skyrme interactions has been developed to study the thermal pairing in excited nuclei [89, 90]. With the use of the Skyrme interactions, the HFB equations were expressed in the radial coordinates of the form as [90]

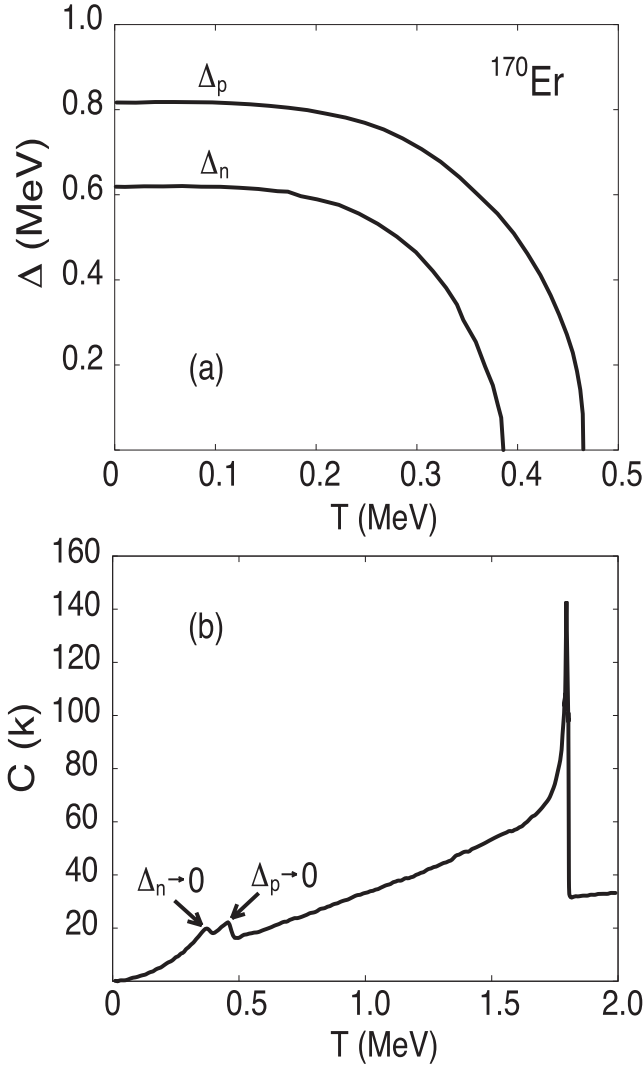


**Figure 25.** Proton and neutron pairing gaps (a) and heat capacity (b) as functions of temperature obtained within the HFB calculation for  $^{170}\text{Er}$ . Adapted with permission from [86], Copyright (1986) by the American Physical Society.

$$\begin{pmatrix} H_T(r) - \lambda & \Delta_T(r) \\ -\Delta_T(r) & -H_T(r) + \lambda \end{pmatrix} \begin{pmatrix} U_i(r) \\ V_i(r) \end{pmatrix} = E_i \begin{pmatrix} U_i(r) \\ V_i(r) \end{pmatrix}, \quad (56)$$

where  $H_T$  is the thermal average Hamiltonian built on the Hartree–Fock mean field with effective Skyrme interactions and density-dependent contact force. The latter has the form

$$\begin{aligned} V(\mathbf{r} - \mathbf{r}') &= V_0 \left[ 1 - \eta \left( \frac{\rho(r)}{\rho_0} \right)^\alpha \right] \delta(\mathbf{r} - \mathbf{r}') \\ &= V_{\text{eff}}[\rho(r)] \delta(\mathbf{r} - \mathbf{r}'), \end{aligned} \quad (57)$$

where  $\rho(r)$  is the baryonic density and  $\eta$  corresponds to the types of pairing force, which equals to 0 and 1 for the volume and surface interactions of the pairing field, respectively. Using this force, the thermal averaged pairing gap  $\Delta_T(r)$  is given as

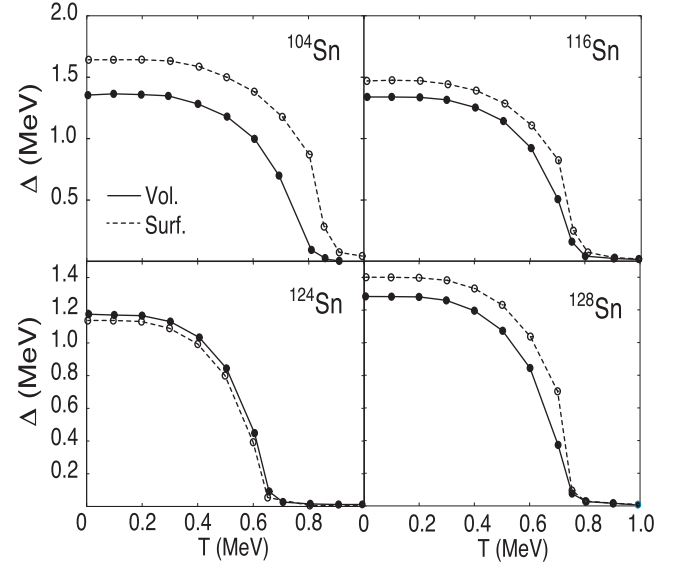


**Figure 26.** Average neutron pairing gaps as functions of temperature obtained within the HFB with Skyrme SLy4 force for  $^{104,116,124,128}\text{Sn}$ . Adapted with permission from [90], Copyright (2007) by Elsevier.

$$\Delta_T(r) = \frac{1}{2} V_{\text{eff}}[\rho(r)] \kappa_T(r), \quad (58)$$

where the thermal averaged pairing tensor  $\kappa_T(r)$  and nucleon density  $\rho_T(r)$  are

$$\begin{aligned} \kappa_T(r) &= \frac{1}{4\pi} \sum_i (2j_i + 1) U_i^*(r) V_i(r) (1 - 2n_i), \\ \rho_T(r) &= \frac{1}{4\pi} \sum_i (2j_i + 1) [V_i^*(r) (1 - n_i) + U_i^*(r) U_i(r) n_i], \end{aligned} \quad (59)$$

with  $n_i = (1 + e^{\beta E_i})^{-1}$  being the temperature-dependent quasiparticle occupation numbers. The average neutron pairing gaps,  $\Delta = \frac{\int \kappa_T(r) \Delta_T(r) dr}{\int \kappa_T(r) dr}$ , obtained within the HFB calculations for  $^{104,116,124,128}\text{Sn}$  (figure 26) are similar to those obtained in figure 25 for  $^{170}\text{Er}$ , namely the gaps decrease with temperature and vanish at around critical temperature  $T_C \simeq 0.5\Delta(T=0)$  of the conventional BCS theory. This behavior of pairing gap does not depend on either the Skyrme force or the types of pairing interaction (volume or surface) as discussed in [90].

The same HFB with Skyrme SLy4 interaction and density-dependent contact (zero-range) force (57) has also been applied to study the pairing and superfluid properties of the inner crust neutron stars [91]. Figure 27 shows an example of the HFB calculation for the crust neutron stars with the  $^{950}\text{Sn}$  and  $^{1800}\text{Sn}$  cells, that is, the cells with  $Z = 50$  protons and  $N = 900$  and  $1750$  neutrons, respectively. This figure indicates that the pairing or superfluid properties of the inner crust matter are strongly affected by the temperature of the crust. For the high density cell ( $^{1800}\text{Sn}$ ), the pairing field is found to decrease strongly in the cluster region, whereas for the

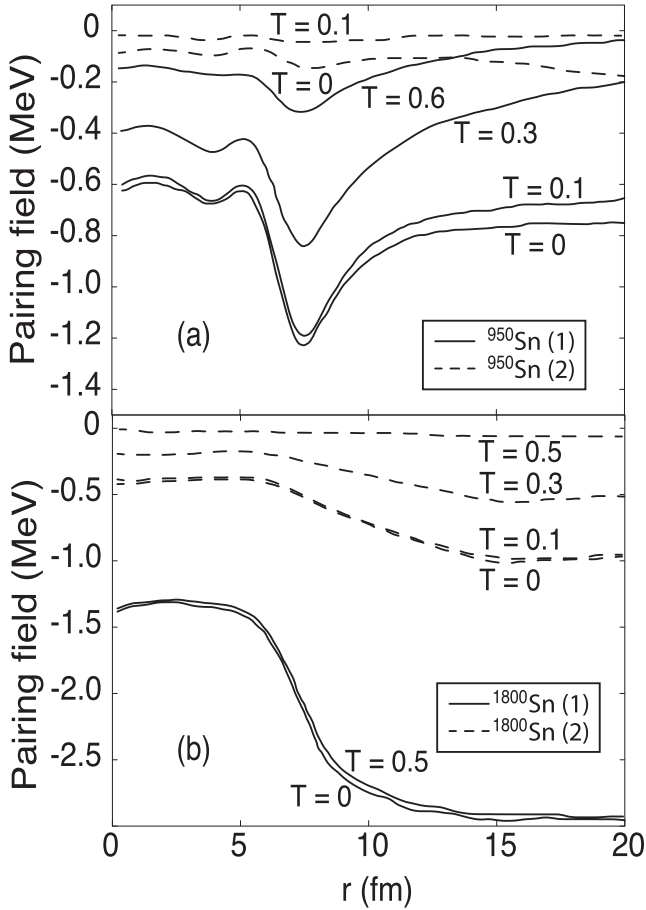


**Figure 27.** Neutron pairing fields at different temperatures obtained within the HFB calculations for the crust neutron stars with the  $Z = 50$  (Sn) proton cells having different neutron numbers, namely  $N = 900$  (a) and  $N = 1750$  (b) neutrons. The numbers 1 and 2, which follow the cell symbols (see the inset), indicate the two parameter sets of the pairing force used in the calculations. Adapted with permission from [91], Copyright (2004) by the American Physical Society.

low-density one ( $^{950}\text{Sn}$ ) it significantly increases in the transition region from the neutron gas to the nuclear matter [91].

The recent calculation within the relativistic HFB (RHFB) with the finite-range Gogny D1S and zero-range DDCI pairing forces using the effective PKO1 Lagrangian at finite temperature predicts the same behavior of neutron pairing gap in  $^{124}\text{Sn}$  nucleus as that predicted within the none-relativistic HFB in figures 25 and 26, namely the neutron pairing gap decreases with temperature and vanishes at the critical temperature  $T_c$  [92]. The value of the latter is found to be very close to the conventional value of the BCS ( $T_c = 0.568\Delta(0)$ ), regardless of the pairing forces (D1S and DDCI) to be used (see e.g. figure 28).

For hot rotating nuclei, the HFB equation was extended to include the cranking term, namely  $H - \lambda\hat{N} - \omega J_x$ , where  $J_x$  is the projection of total angular momentum along the  $x$ -axis ( $\langle J_x \rangle = J$ ) and  $\omega$  is the rotational frequency [34, 93–95]. Here the  $x$ -projection of the total angular momentum  $J_x$ , favorable for the study of deformed nuclei, is used instead of its  $z$ -projection (limited to the spherical or quasi-spherical nuclei only) as in the previous section 2. The derivation of

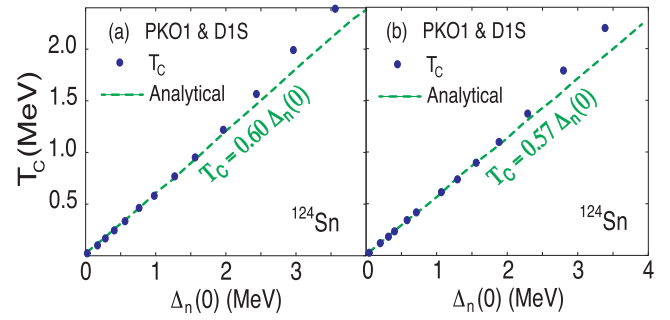


**Figure 28.** Critical temperature  $T_c$  as a function of neutron pairing gap at  $T = 0$  obtained within the relativistic HFB calculation with the finite-range Gogny D1S (a) and zero-range DDCI pairing forces (b) using the PKO1 Lagrangian for  $^{124}\text{Sn}$  nucleus. The dashed lines stand for the analytical relation  $T_c = 0.60(0.57)\Delta_n(0)$ . Adapted with permission from [92], Copyright (2015) by the American Physical Society.

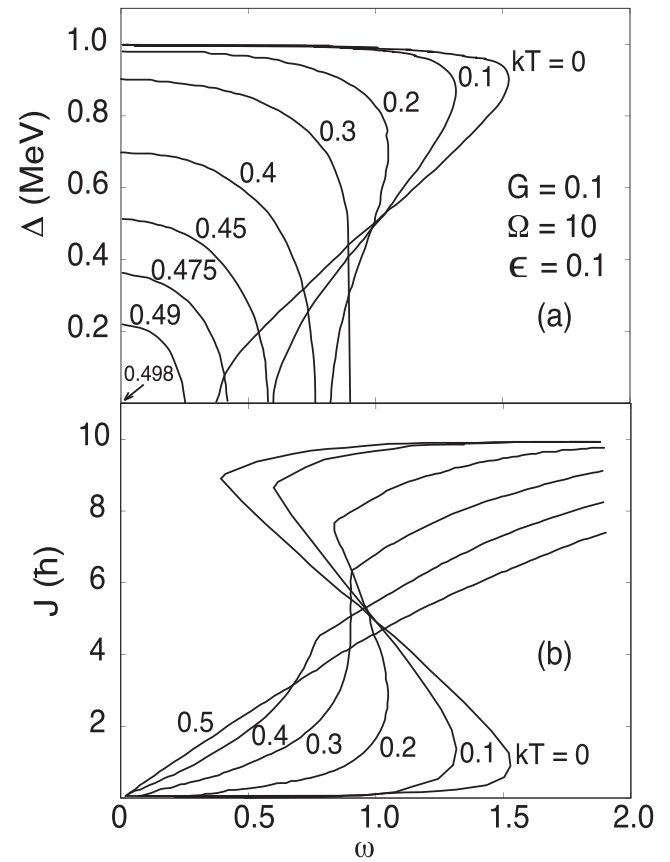


**Figure 29.** Pairing gap  $\Delta$  (a) and angular momentum  $J$  (b) versus angular velocity  $\omega$  obtained within the cranked HFB calculation for a two-level model at different temperatures. Adapted with permission from [93], Copyright (1981) by Elsevier.

the cranked HFB equation was presented in detail in [93]. Figure 29 shows a very simple example of the cranked HFB calculation for a two-level model [93]. The latter contains  $\Omega$  identical sets of four states, each of which consists of two half-filled levels with the single-particle energies equal to  $\pm\epsilon$ . Each particle has spin  $J_x = \pm\frac{1}{2}$  and interacting via a constant pairing strength  $G$ . The total number of particles in this case is  $N = 2\Omega$ , whereas the maximum spin  $\langle J_x \rangle = \Omega$  (see e.g.

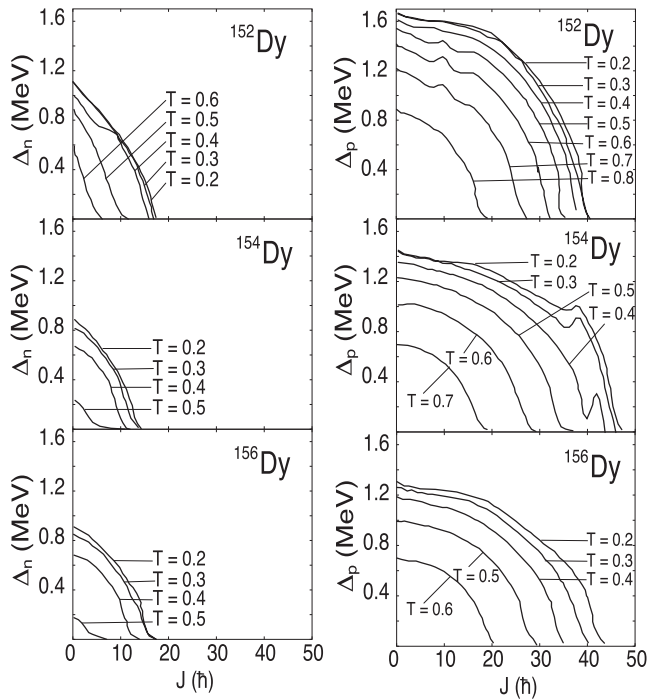


**Figure 30.** Neutron  $\Delta_n$  and proton  $\Delta_p$  pairing gaps versus total angular momentum  $J$  obtained within the cranked HFB calculation at several temperatures for  $^{152,154,156}\text{Dy}$  isotopes. Adapted with permission from [96], Copyright (1995) by the American Physical Society.

figure 2 in [93]). Figure 29(a) indicates that the pairing gap obtained within the cranked HFB decreases with increasing both temperature and rotational frequency. For  $T < 0.3$  MeV, the gap has triple values, indicating the well-known backbending effect as clearly seen in figure 29(b), where the total angular momentum is displayed versus the rotational frequency at different temperatures. Increasing temperature  $T > 0.3$  MeV gradually smears out the backbending effect. This finding of the cranked HFB is qualitatively similar as that obtained within the BCS calculation with fixed  $z$ -projection of angular momentum for the uniform model (see e.g. [67]). Similar effect was reported in the same cranked HFB calculation for a more realistic  $j = 13/2$  model [34]. However the  $(J, T)$  diagram obtained within the cranked HFB in [34, 93] shows no evidence of the pairing reentrance as that predicted within the BCS (e.g. figure 6). The recent neutron and proton pairing gaps obtained within cranked HFB calculations for three  $^{152,154,156}\text{Dy}$  isotopes (figure 30) show no significant difference with those obtained within the above simple models [96].

It is worthwhile to mention that although the HFB and/or RHFB are more realistic than that of the conventional BCS, their predictions for the nuclear pairing properties are qualitatively similar to those of the BCS. The reason is that all the theories, which are based on the Bogoliubov's transformation, violate the particle number conservation. The HFB/RHFB and BCS theories also neglect thermal fluctuations. The latter are known to be important in finite systems so that they smooth out the superfluid-normal phase transition in atomic nuclei as discussed in section 2. As will be seen in section 4,

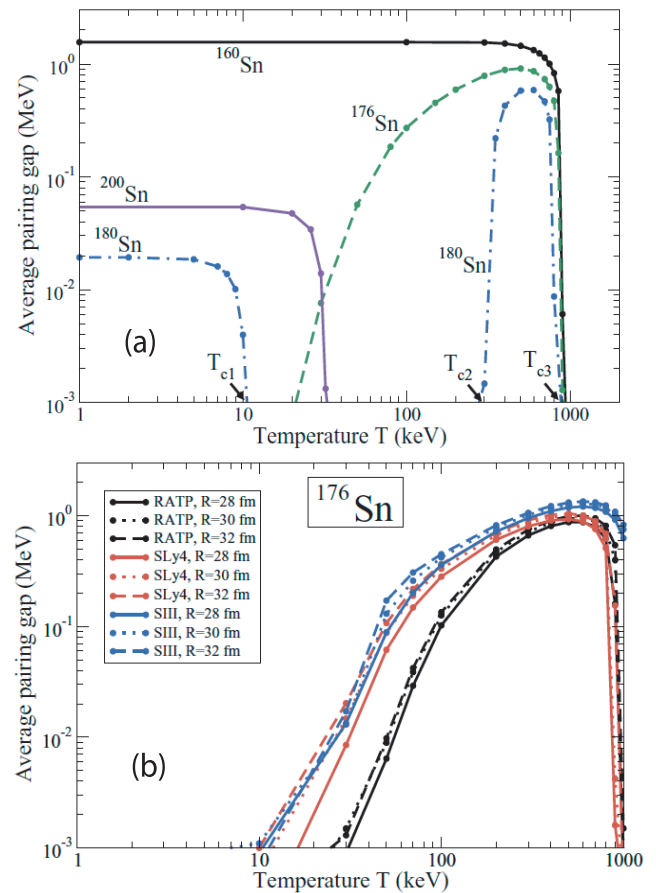


**Figure 31.** Average neutron pairing gap versus temperature obtained within the HFB for  $^{160,176,180,200}\text{Sn}$  using the DIS Gogny (a) and for  $^{176}\text{Sn}$  using three Skyrme interactions with different sizes of the box radius (b). Adapted with permission from [97], Copyright (2012) by the American Physical Society.

the approximate particle-number projection and exact-pairing methods offer a better description of thermal pairing in finite nuclear systems.

### 3.2. Finite-temperature pairing reentrance in even-even nuclei

The calculations of the neutron pairing gap obtained within the HFB calculation for near drip line  $^{176}\text{Sn}$  (by using different versions of the Skyrme force), beyond drip line  $^{180}\text{Sn}$  (by using the DIS Gogny force) nuclei in [97] (figure 31), and those within both HFB and RHFB [98] (by using different versions of the Skyrme interaction and effective Lagrangian) (figure 32) have suggested the pairing reentrance phenomenon at finite temperature. For example, in [98], it is clearly seen that the proton pairing gap of a doubly magic nucleus  $^{48}\text{Ni}$  is zero at  $T \leq T_{c1}$ , increases to reach a maximum at  $T > T_{c1}$ , and decreases to vanish at  $T \geq T_{c2}$  (figure 32). The values of  $T_{c1}$  and  $T_{c2}$  are found to be around 0.08–0.2 MeV and 0.7–0.9 MeV, respectively.

This phenomenon of pairing reentrance in even-even nuclei at finite temperature was first pointed out in [99, 100], where the modified BCS (see section 6.1.2 for the details of the modified BCS theory) was employed to study the thermal pairing properties

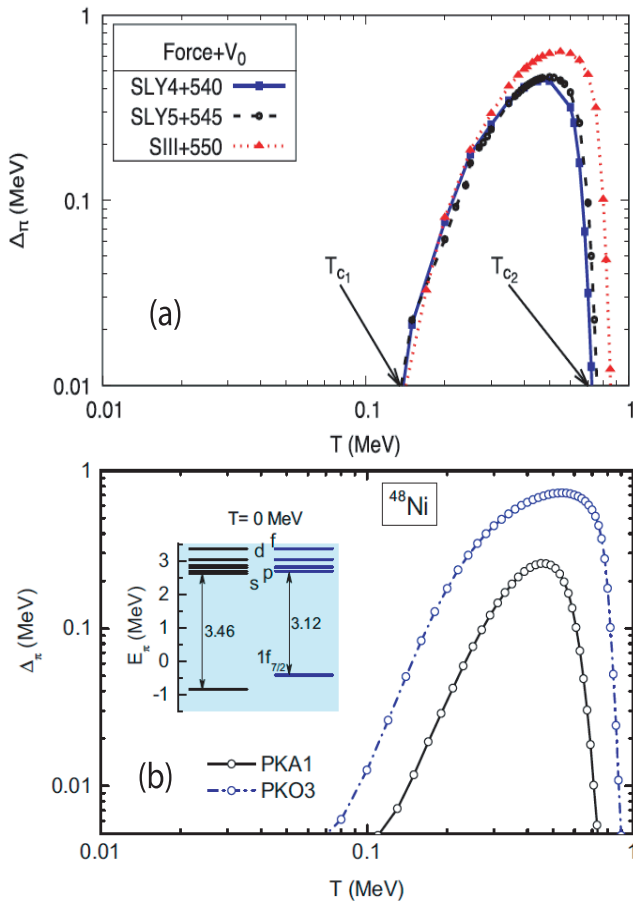


**Figure 32.** Average proton pairing gap versus temperature obtained within the HFB with different Skyrme forces (a) and relativistic HFB with the effective PKA1 and PKO3 Lagrangians (b) for  $^{48}\text{Ni}$ . Adapted with permission from [98], Copyright (2017) by the American Physical Society.

of several even-even  $^{68-84}\text{Ni}$  isotopes. By taking into account coupling to the continuum via the resonance states with the finite widths, it has been predicted in [99] that the neutron pairing gap in  $^{84}\text{Ni}$ , which is beyond the drip line, increases from 0.06 MeV at the temperature  $T = 1.5$  MeV to a value of 0.2 MeV at  $T = 6$  MeV (figure 33), which is the signal of the finite-temperature pairing reentrance. The latter is caused by the effect of the lowest resonance state  $2d_{3/2}$  in the neutron single-particle spectrum of this  $^{84}\text{Ni}$  nucleus as explained in [99]. By artificially reducing the energy of the above  $2d_{3/2}$  resonance state, the effect of pairing reentrance becomes stronger (figure 33), indicating the strong presence of pairing reentrance in nuclei close or beyond the drip line. The discussion in [97, 98], which failed to quote [99], is exactly on this line, namely this pairing reentrance is observed at finite temperature for isotopes, which are near or beyond the drip line and belong to the group where the resonance states are located at a too high energy at zero temperature (preventing them to participate to pairing), but close enough to the last occupied state to be reached at finite temperature (available for pairing).

The discussion above shows that the mechanism causing the pairing reentrance in neutron-rich nuclei at finite temperature is completely different from that occurring in the hot rotating systems, where the rotation is combined with the effect of temperature to make the reentrance of pairing

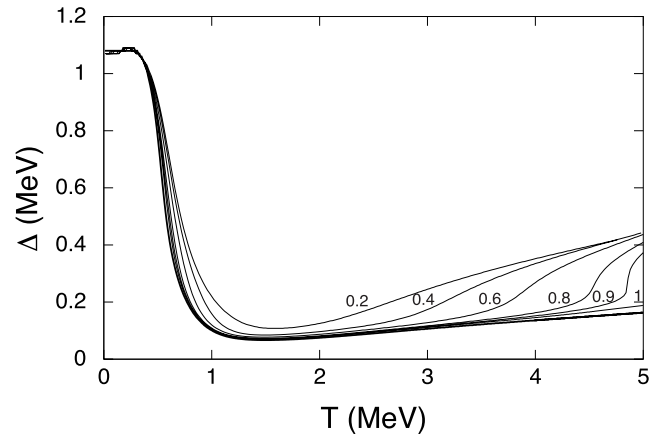


**Figure 33.** Neutron pairing gap as a function of temperature obtained within the resonant-continuum modified BCS theory for  $^{84}\text{Ni}$ . Each line corresponds to different value of the lowest resonance state as indicated on the curves. Adapted with permission from [99], Copyright (2003) by the American Physical Society.

correlation as discussed in the Introduction and section 2. It is also different from the pairing reentrance due to weakening of the blocking effect at finite temperature to be discussed in the next section 3.3.

### 3.3. Finite-temperature pairing reentrance in odd nuclei

The finite-temperature pairing reentrance phenomenon in odd systems with small number of particles was predicted in [30] where the generalized BCS theory with the number-parity projections was applied to study the thermal pairing properties of some finite systems such as superconducting metallic islands and ultrasmall metallic grains. Figure 34 shows an example of the pairing gaps obtained within generalized BCS with the number-parity projected method for the extremely small superconducting grains with the average particle numbers  $\langle N \rangle$  being equal to 100 (even) and 101 (odd) [30]. Figure 34(a) illustrates that the critical temperature associated with the even particle-number-parity projection is larger than the conventional BCS value. In particular, the gap obtained within the odd particle-number-parity projection in figure 34(b) clearly shows the pairing reentrance effect, which is similar as that found in figures 31 and 32 for  $^{176,180}\text{Sn}$  and  $^{48}\text{Ni}$  even-even nuclei. However, the physical nature of the pairing reentrance in odd systems is completely different with that observed in the even ones, namely it is caused by the blocking effect of the odd particle, which is strong at zero temperature but depleted at finite temperature. This effect has been latter confirmed in [101] where a correct treatment of the blocking effect in odd nuclei at finite temperature was proposed. This treatment begins with the analysis of the exact solution of the pairing Hamiltonian (1) at finite temperature (see section 4.3 for the details of exact pairing solutions at finite temperature). For example, figure 35(a) shows the occupation numbers obtained within the finite-temperature exact pairing for the doubly-folded equidistant multilevel pairing model with  $\Omega = 10$  single-particle levels and  $N = 9$  (odd) particles. It is seen in figure 35(a) that the thick solid line, which

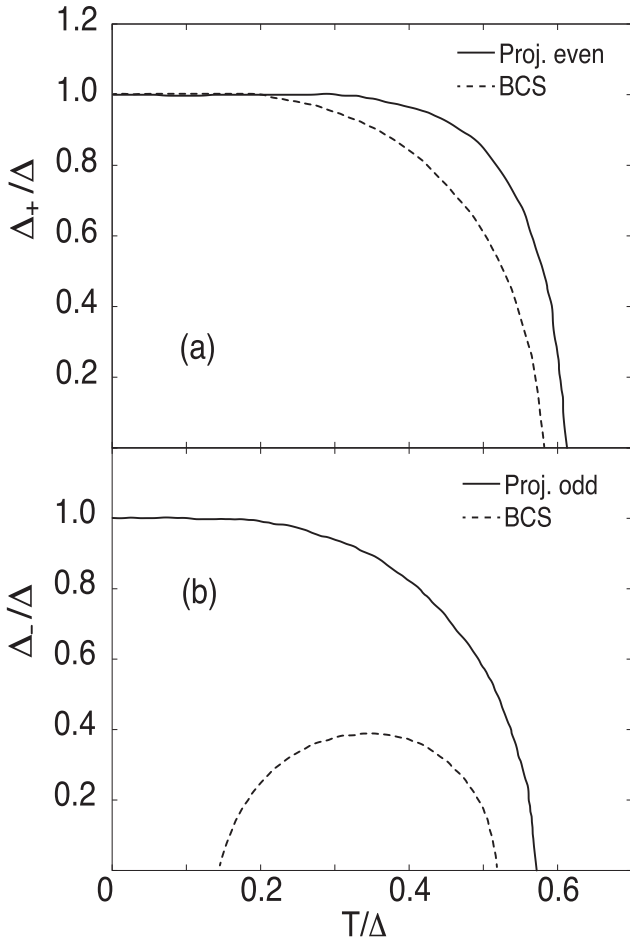


**Figure 34.** Pairing gaps as a function of temperature obtained within the conventional BCS and number-parity projected method for superconducting ultrasmall metallic grains with even particle number  $\langle N \rangle = 100$  (a) and odd particle number  $\langle N \rangle = 101$  (b). Adapted with permission from [30], Copyright (1999) by Elsevier.

separates two groups of lines corresponding to two groups of levels below and above the Fermi surface with the occupation numbers of around 2 and 0, respectively, is the occupation number of the level occupied by the odd particle. This line starts from 1 at zero temperature and decreases slightly with increasing temperature, implying two important features. The first feature is that, although the odd particle is allowed to distribute in all the levels in the exact diagonalization of the pairing Hamiltonian, it always occupies the fifth level, which is the highest occupied one. This feature invalidates the conventional assumption given in the Maino's method [102, 103] that the odd particle must be on any level above the Fermi surface. The Maino's method was popularly used to describe the pairing properties of excited odd nuclei. The second feature is that the occupation number of the odd particle does not remain equal to 1 as its value at zero temperature, but decreases with increasing temperature as discussed in [101]. This feature clearly indicates that the blocking effect caused by the odd particle is weakened due to the effect of temperature. Therefore, a correct formula for the odd-particle-number equation at finite temperature in the BCS theory has been proposed to take into account the above important features, namely

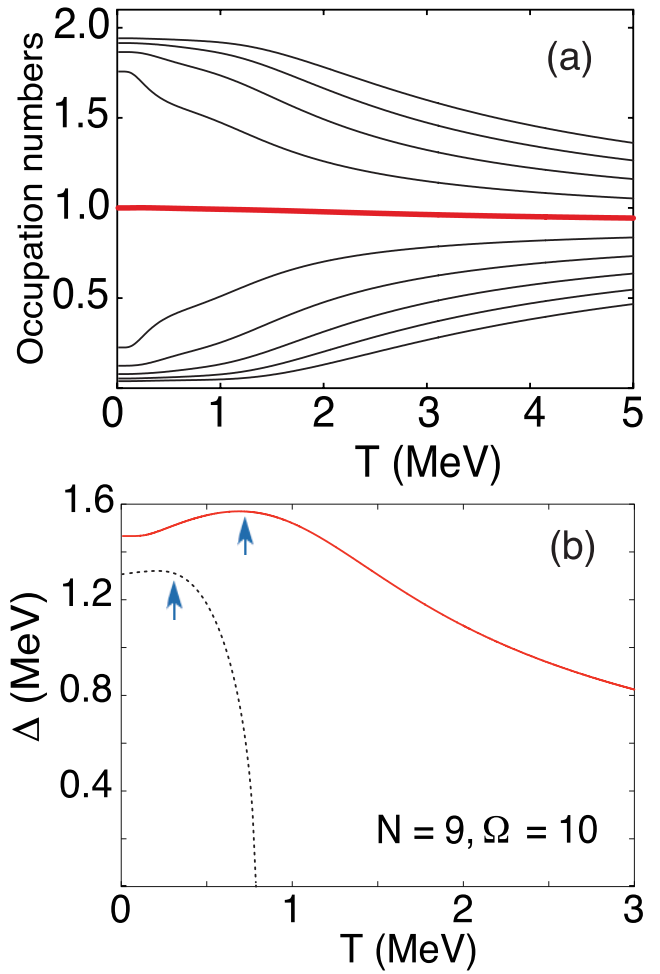


**Figure 35.** (a) Occupation numbers of the single-particle levels as functions of temperature obtained within the finite-temperature exact pairing for the doubly-folded equidistant multilevel pairing model with  $\Omega = 10$  levels and  $N = 9$  (odd) particles. The higher-located line is the occupation number of the lower-located level and vice versa. The thick solid line, which starts from 1 at zero temperature, is the occupation number of the level occupied by the odd particle. (b) Pairing gaps versus temperature obtained within the  $q_k$ -blocked BCS (dotted line) and exact solution (solid line) for the schematic pairing model in (a). The arrows illustrate the region of the pairing reentrance. Adapted with permission from [101], Copyright (2016) by the American Physical Society.

$$N_{\text{odd}} = q_k + 2 \sum_{k' \neq k} [n_{k'} u_{k'}^2 + (1 - n_{k'}) v_{k'}^2], \quad (60)$$

where  $q_k = 1 - \frac{1}{\exp(|\epsilon_k - \lambda|/T) + 1}$  is the occupation number of the odd particle on the blocked single-particle level  $k$  [101]. This occupation number  $q_k$  of the odd particle automatically satisfies two conditions observed in its above exact solution, namely it equals to 1 at zero temperature and varies with temperature. The BCS theory with the improved equation for the odd-particle number (60) is called  $q_k$ -blocked BCS. The results obtained within this  $q_k$ -blocked BCS are found to agree with the exact solution better than those obtained by using the conventional Maino's method for the pairing model with  $N = 9$  particles and different numbers of single-particle levels

$\Omega$  as indicated in figures 3 and 4 of [101]. In particular, the gap obtained within  $q_k$ -blocked BCS increases slightly with temperature at low temperature, which qualitatively agrees with the exact gap (figure 35(b)). This increase of the pairing gap, which is caused by weakening of the blocking effect at finite temperature, is known as the signature of finite-temperature pairing reentrance.

#### 4. Canonical and microcanonical treatments of pairing problem

##### 4.1. Particle-number projection

The violation of particle number  $N$  in the BCS (HFB) ground-state wave function causes the particle-number fluctuation. The latter is present even at  $T = 0$  as the quantal fluctuation, whereas the statistical fluctuation caused by temperature vanishes. Various methods of particle-number projection have been proposed to eliminate this defect by projecting out the component of the wave function corresponding to the right particle number. The particle-number projected energy  $\mathcal{E}^{(N)}$  is obtained by applying the particle-number projected operator  $P^N = (2\pi)^{-1} \int d\phi e^{-i\phi(\hat{N}-N)}$  to a model Hamiltonian  $H$  whose expectation (or average) value in the ground state (or grand canonical ensemble) corresponds to the energy of the system under consideration, namely  $\mathcal{E}^{(N)} = \langle HP^N \rangle / \langle P^N \rangle$ . The particle-number projected methods are classified as the projection after variation and variation after projection ones. The projection after variation uses the BCS (HFB) wave function to calculate the projected energy of the system, whereas the variation after projection minimizes the projected energy to determine the wave function. Therefore, the variation after projection approach is a much better projection method as compared to the projection after variation one, especially in the region where the BCS (HFB) theory breaks down, that is, at very weak interaction and/or temperature above  $T_c$ .

Since a rigorous particle-number projection is impracticable for numerical calculations at finite temperature, various approximate particle-number projection have been proposed. Among the approximate variation after projection methods, the Lipkin–Nogami one, proposed by Lipkin and Nogami [104–107], is quite popular because of its simplicity in numerical calculations. It expresses the expectation value of the pairing Hamiltonian within the projected BCS state in terms of that within the unprojected BCS state. The infinite expansion series is truncated at the second order of the particle-number operator  $N$  to minimize the resulting pairing Hamiltonian  $H - \lambda_1 N - \lambda_2 N^2$ , where only  $\lambda_1$  is the Lagrangian multiplier, whereas the expansion coefficient  $\lambda_2$  is analytically expressed in terms of the coefficients  $u_k$  and  $v_k$  of the Bogoliubov's transformation as [108]

$$\lambda_2 = \frac{G \sum_k (1 - \rho_k) \tau_k \sum_{k'} \rho_{k'} \tau_{k'} - \sum_k (1 - \rho_k)^2 \rho_k^2}{4 [\sum_k \rho_k (1 - \rho_k)]^2 - \sum_k \rho_k^2 (1 - \rho_k)^2}, \quad (61)$$

with  $\rho_k = v_k^2 + (1 - 2n_k^2)n_k$  and  $\tau_k = u_k v_k (1 - 2n_k)$  being the single-particle density and particle-pairing tensor, respectively. The Lipkin–Nogami equations for the gap and particle

number, therefore, have the same formal expressions as those of the BCS equations, where the single-particle energies  $\epsilon_k$  are replaced with their renormalized values

$$\epsilon'_k = \epsilon_k + (4\lambda_2 - G)v_k^2, \quad (62)$$

which determine the quasiparticle energies  $E_k = \sqrt{(\epsilon'_k - \lambda)^2 + \Delta^2}$  with the chemical potential  $\lambda = \lambda_1 + 2\lambda_2(N + 1)$ . Different from the BCS theory, which has nontrivial solutions only above a critical value  $G_c$  of the pairing-interaction parameter  $G$ , the nontrivial solutions of the Lipkin–Nogami equations exist at any nonzero value of  $G$ , and they are very close to the exact ones. The projected total energy of the system is obtained by solving these BCS equations self-consistently with (61) in the form

$$\begin{aligned} \mathcal{E}_{\text{LN}} &= \mathcal{E}_{\text{pair}} - \lambda_2 \delta N^2, \\ \mathcal{E}_{\text{pair}} &= \sum_k (\epsilon_k - G\rho_k) \rho_k - \frac{\Delta^2}{G}. \end{aligned} \quad (63)$$

The particle-number fluctuation  $\delta N^2 \equiv \langle \hat{N}^2 \rangle - \langle \hat{N} \rangle^2$  is given as the sum of the quantal  $\delta N_{\text{QF}}^2$  and statistical  $\delta N_{\text{SF}}^2$  fluctuations, namely  $\delta N^2 = \delta N_{\text{QF}}^2 + \delta N_{\text{SF}}^2$  [29], where

$$\begin{aligned} \delta N_{\text{QF}}^2 &= 4 \sum_k u_k^2 v_k^2 (1 - 2n_k), \\ \delta N_{\text{SF}}^2 &= 2 \sum_k [(1 - 2v_k^2)^2 \mathcal{N}_k + 8(u_k v_k n_k)^2], \end{aligned} \quad (64)$$

and

$$\delta \mathcal{N}_k^2 = n_k (1 - n_k), \quad n_k = \frac{1}{\exp(\beta E_k) + 1}, \quad (65)$$

is the quasiparticle-number fluctuation on the  $j$ th level. At  $T = 0$ , only the quantal fluctuation  $\delta N_{\text{QF}}^2$  remains because the quasiparticle occupation numbers  $n_k$  vanish so does the statistical fluctuation  $\delta N_{\text{SF}}^2$ . With increasing  $T$ , the quantal fluctuation  $\delta N_{\text{QF}}^2$  decreases, whereas the statistical fluctuation  $\delta N_{\text{SF}}^2$  increases, being dominated mainly by the quasiparticle-number fluctuation  $\delta \mathcal{N}_k^2$  because the latter increases while  $u_k v_k$  decreases. Within the BCS, at  $T \geq T_c$ , where the BCS gap vanishes, the particle-number fluctuation  $\delta N^2$  consists only of the statistical fluctuation, which is now expressed in terms of thermal particle-number fluctuations  $\delta N_k^2 = f_k (1 - f_k)$  with the single-particle occupation numbers  $f_k = 1 / \{\exp[\beta(\epsilon_k - \lambda)] + 1\}$ .

The particle number projection only removes the quantal fluctuation from the pairing field, whereas the statistical fluctuation can be eliminated by going beyond the pairing mean field theory. A method, which combines the Lipkin–Nogami method with the static-path approximation to eliminate both quantal and statistical fluctuations from the pairing field, has been proposed in [109]. The static-path approximation uses an expansion of the effective action into a power series around the static path, which is an average of temperature-dependent paths, to carry out the integration over all the static paths, which include all the sums over fluctuations of the pairing mean field.

The static-path approximation replaces the grand potential  $Z(\beta, \lambda) \equiv \text{Tr}\{\exp[-\beta(H - \lambda N)]\}$  with the Trotter product

of time slides and expresses the exponential of each slide as an integral over the one-body Hamiltonian by using the Hubbard–Stratonovich transformation [110, 111]. The partition function of the static-path approximation  $Z_{\text{SPA}}(\beta, \lambda)$  is obtained by integrating the functional representation of the grand potential  $Z(\beta, \lambda)$  over the pairing-field time averages  $\zeta = \Delta e^{i\phi}$  and  $\zeta^*$  in the form

$$\begin{aligned} Z_{\text{SPA}}(\beta, \lambda) &= \frac{2\beta}{G} \int_0^\infty \mathcal{P}(\beta, \lambda, \Delta) \Delta d\Delta, \\ \mathcal{P}(\beta, \lambda, \Delta) &= \exp[-\beta \Omega_{\text{SPA}}(\beta, \lambda, \Delta)], \end{aligned} \quad (66)$$

with the thermodynamic probability  $\mathcal{P}(\beta, \lambda, \Delta)$  determined in terms of the thermodynamic potential  $\Omega_{\text{SPA}}$

$$\begin{aligned} \Omega_{\text{SPA}} &= \mathcal{E}_{\text{pair}} - \lambda N - TS = \sum_k (\epsilon_k - \lambda - E_k) \\ &\quad - \frac{2}{\beta} \sum_k \ln[1 + \exp(-\beta E_k)] + \frac{\Delta^2}{G}. \end{aligned} \quad (67)$$

The partition function of the static path approximation is different from the usual thermodynamic one by the factor  $2\beta/G$ , which affects the energy evaluation, and the metric  $\Delta d\Delta$  instead of  $d\Delta$  used in the thermodynamic averages in [24]. When the pairing field is given by its self-consistent value  $\zeta = G \langle a_{-k} a_k \rangle$ , the energy  $\mathcal{E}_{\text{pair}}$  is equivalent to the usual BCS energy with the pairing gap defined from the BCS equations. The static path approximation becomes exact in the high-temperature limit.

The Lipkin–Nogami method is combined with the static path approximation by replacing the thermodynamic potential  $\Omega_{\text{SPA}}$  in (66) and (67) with  $\Omega_{\text{LN(SPA)}}$ , which includes the Lipkin–Nogami corrections, namely  $\Omega_{\text{LN(SPA)}} = \Omega_{\text{SPA}} - \lambda_2 \delta N^2 + \langle \hat{H}_{\text{res}} \rangle$ , where  $\epsilon_k$  in  $\Omega_{\text{SPA}}$  is replaced with the renormalized  $\epsilon'_k$  by the exchange term  $-Gv_j^2$  and the Lipkin–Nogami correction  $4\lambda v_k^2$  in (62), and  $\langle \hat{H}_{\text{res}} \rangle$  is the contribution from the residual interaction in the pairing Hamiltonian, which cannot be included in the conventional BCS, namely  $\langle \hat{H}_{\text{res}} \rangle = G \sum_k n_k (\epsilon'_k - \lambda) [1 - (\epsilon'_k - \lambda) (1 - 2n_k)/E_k] / (2E_k)$ . By using the total energy of the system,  $\mathcal{E}_{\text{LN(SPA)}}$  can be calculated within the LN(SPA) as

$$\begin{aligned} \mathcal{E}_{\text{LN(SPA)}}(\beta) &\equiv -\frac{\partial \ln Z_{\text{LN(SPA)}}}{\partial \beta} + \lambda N \\ &= \int_0^\infty \langle \hat{H} \rangle \mathcal{P}_{\text{LN(SPA)}} \Delta d\Delta \Big/ \int_0^\infty \mathcal{P}_{\text{LN(SPA)}} \Delta d\Delta - \beta^{-1}, \end{aligned} \quad (68)$$

and the LN(SPA) average pairing gap is determined as

$$\Delta_{\text{LN(SPA)}}(\beta) = \sqrt{-G \mathcal{E}_{\text{LN(SPA)}}}. \quad (69)$$

From the results of calculations carried out within the half-filled shell of the model with  $2\Omega$  degenerate single-particle levels with  $N = \Omega = 20$  particles interacting via a monopole pairing force ( $G = -2\lambda = 0.1$  MeV) and  $\epsilon = \Delta$  [112], it is seen that the Lipkin–Nogami corrections (the dashed curve in figure 36(a)) significantly improve the static-path-approximation energy (the dotted curve in figure 36(a)), almost eliminating the discrepancy with the exact result (the solid curve

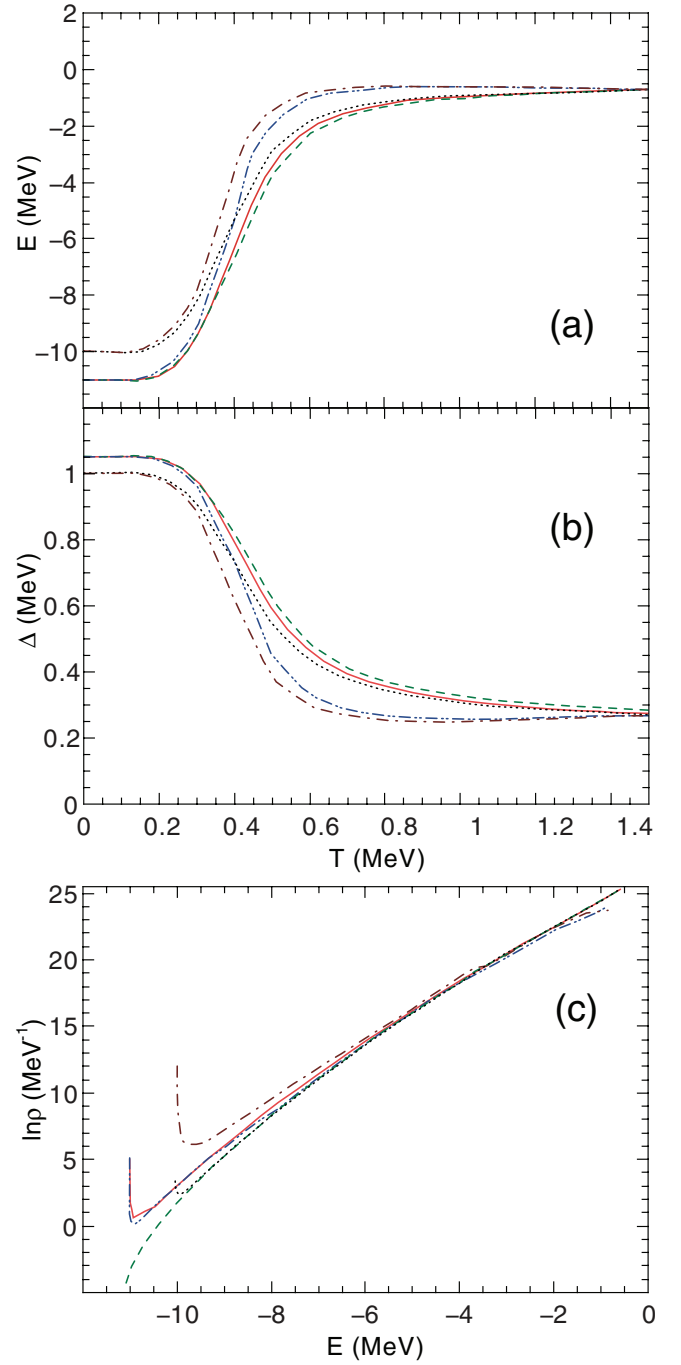


**Figure 36.** Total energy (a), average pairing gap (b) and logarithm of energy level density (c) as functions of temperature ((a) and (b)) and energy (c) in the degenerate  $2\Omega$ -level model. The solid, dotted, dashed, dot-dashed, and double-dot-dashed lines correspond to the result of the exact calculations within the seniority scheme, static path approximation, Lipkin–Nogami (static path approximation), thermodynamic average in the BCS, and BCS with Lipkin–Nogami corrections, respectively. Adapted with permission from [109], Copyright (1993) by the American Physical Society.

in figure 36(a)). Within the Lipkin–Nogami method, the pairing gap reaches the exact value at low  $T$  in both traditional thermodynamic and static path approximation contexts. At high  $T$ , only the pairing gaps obtained within the static path approximation (with or without the Lipkin–Nogami corrections) are close to the exact results (figure 36(b)). Regarding

the energy level density, its logarithm obtained within the static path approximation is quite accurate at high  $T$  (figure 36(c)), whereas at low  $T$  the traditional thermodynamic average including the Lipkin–Nogami corrections gives a better result (the double-dot-dashed curve in figure 36(c)). However, in the context of the static path approximation, the Lipkin–Nogami (static path approximation) allows the calculations of the level density to be extended to lower energies.

Recently, an alternative variation after projection method at finite temperature has been proposed based on the HFB wave function or density operator  $\mathcal{D} = [P^N \exp(-\beta H) P^N] / Z$ , where  $Z = \text{Tr}[P^N \exp(-\beta H) P^N]$ , instead of the BCS(LN) one [113, 114]. The results of total energy, entropy, heat capacity, and pairing gap obtained for a simple two-level model [113] as well as a more realistic doubly folded equidistant multilevel model (see e.g. figure 37) [114] agree quite well with the exact solutions. However, this variation after projection method is still too complicated to be applied to practical calculations in realistic nuclei.

#### 4.2. BCS with Lipkin–Nogami particle number projection plus self-consistent quasiparticle random-phase approximation incorporated into the canonical and microcanonical ensembles

The description of thermal pairing in nuclei within the canonical ensemble can be undertaken either within the finite-temperature particle-number projection as presented in section 4.1 or based on the solutions of a particle-number conserving approach at  $T = 0$ , which are incorporated into the canonical ensemble. The latter is usually carried out by solving the BCS equations in combination with the Lipkin–Nogami particle-number projection [104–107] at  $T = 0$  for each total seniority  $s$  of the system, which is the total number of unpaired particles [115]. When the nucleus is heated (excited), the nucleon pairs are broken, leading to the unpaired particles denoted by the quantum number  $k_s$ . These unpaired particles will block the single-particle levels  $k$ , making them unfavorable for pairing correlation. These blocked levels  $k_s$ , whose occupation numbers are always equal to  $1/2$ , should be therefore excluded from the Lipkin–Nogami BCS (LNBCS) equations. Consequently, the LNBCS equations at  $T = 0$  for each total seniority  $s$  have the following form [116]

$$\Delta^{\text{LNBCS}}(k_s) = G \sum_{k \neq k_s} u_k v_k, \quad N = 2 \sum_{k \neq k_s} v_k^2 + s, \quad (70)$$

where

$$u_{k \neq k_s}^2 = \frac{1}{2} \left( 1 + \frac{\epsilon_k - G v_k^2 - \lambda(k_s)}{E_k} \right),$$

$$v_{k \neq k_s}^2 = \frac{1}{2} \left( 1 - \frac{\epsilon_k - G v_k^2 - \lambda(k_s)}{E_k} \right),$$

$$E_{k \neq k_s} = \sqrt{[\epsilon_k - G v_k^2 - \lambda(k_s)]^2 + [\Delta^{\text{LNBCS}}(k_s)]^2},$$

$$\lambda(k_s) = \lambda_1(k_s) + 2\lambda_2(k_s)(N + 1),$$

$$\lambda_2(k_s) = \frac{G \sum_{k \neq k_s} u_k^3 v_k \sum_{k' \neq k_s} u_{k'} v_{k'}^3 - \sum_{k \neq k_s} u_k^4 v_k^4}{4 \left( \sum_{k \neq k_s} u_k^2 v_k^2 \right)^2 - \sum_{k \neq k_s} u_k^4 v_k^4}.$$

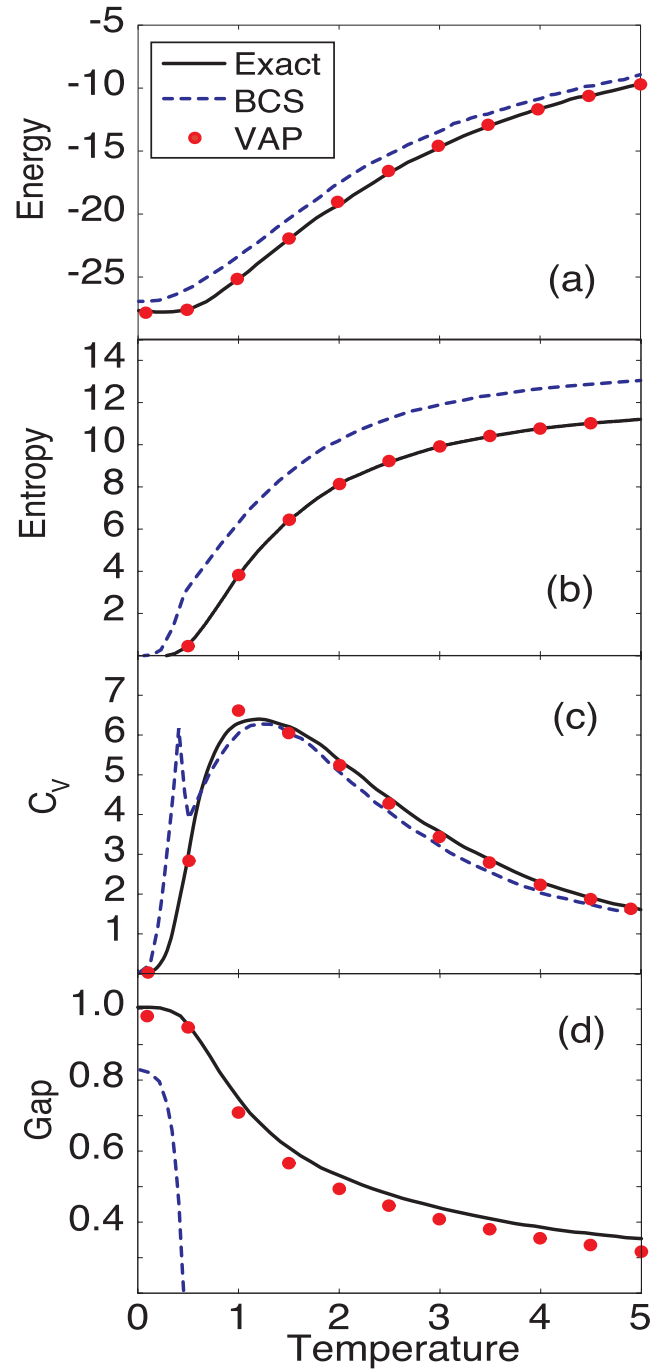


**Figure 37.** Total energy (a), entropy (b), heat capacity (c), and pairing gap (d) obtained within the conventional BCS, variation after projection (VAP) methods and exact solution at finite temperature for a double-folded equidistant multilevel pairing model with  $\Omega = 10$  levels and  $N = \Omega$  particles. Adapted with permission from [114], Copyright (2012) by the American Physical Society.

There are  $n_{\text{LNBCS}} = \sum_s C_s^\Omega$  possible configurations of  $s$  unpaired particles distributed among  $\Omega$  single-particle levels, which is also the total number of eigenstates obtained within the LNBCS. The values of  $s$  are  $0, 2, \dots, \Omega$  and  $1, 3, \dots, \Omega$  for even and odd nuclei, respectively. The LNBCS eigenvalues  $\mathcal{E}_{i_s}^{\text{LNBCS}}$ , which are also the LNBCS energies, for each configuration are then given as [116]

$$\begin{aligned} \mathcal{E}_{i_s}^{\text{LNBCS}} &= 2 \sum_{k \neq k_s} \epsilon_k v_k^2 + \sum_{k_s} \epsilon_{k_s} - \frac{[\Delta^{\text{LNBCS}}(k_s)]^2}{G} \\ &\quad - G \sum_{k \neq k_s} v_k^4 - 4\lambda_2(k_s) \sum_{k \neq k_s} u_k^2 v_k^2. \end{aligned} \quad (71)$$

Using the above eigenvalues, one is able to construct the partition function of the LNBCS based on the canonical ensemble, which is abbreviated as CE-LNBCS [115, 116]

$$Z_{\text{CE-LNBCS}}(\beta) = \sum_s d_s \sum_{i_s=1}^{n_{\text{LNBCS}}} e^{-\beta \mathcal{E}_{i_s}^{\text{LNBCS}}}, \quad (72)$$

where  $d_s = 2^s$  is the degeneracy. All the thermodynamic quantities such as free energy  $\mathcal{F}$ , entropy  $\mathcal{S}$ , total energy  $\mathcal{E}$ , and heat capacity  $\mathcal{C}$  are consequently calculated based on the partition function (72) as follows

$$\begin{aligned} \mathcal{F} &= -T \ln Z(T), \quad \mathcal{S} = -\frac{\partial \mathcal{F}}{\partial T}, \\ \mathcal{E} &= \mathcal{F} + T\mathcal{S}, \quad \mathcal{C} = \frac{\partial \mathcal{E}}{\partial T}. \end{aligned} \quad (73)$$

The pairing gap is also calculated based on the partition function (72) as [115, 116]

$$\begin{aligned} \Delta_{\text{CE-LNBCS}} &= \frac{1}{Z_{\text{CE-LNBCS}}} \\ &\quad \times \sum_s d_s \sum_{i_s}^{n_{\text{LNBCS}}} \Delta_{i_s}^{\text{LNBCS}} e^{-\beta \mathcal{E}_{i_s}^{\text{LNBCS}}}, \end{aligned} \quad (74)$$

where  $\Delta_{i_s}^{\text{LNBCS}} = \Delta^{\text{LNBCS}}(k_s)$  are the seniority-dependent gaps, whose values are obtained after solving (70) for different seniorities  $s$  at  $T = 0$ .

It is worth mentioning that the CE-LNBCS partition function (72) consists of the lowest excited states in each seniority configuration  $s$  only. Consequently, it can be only used to describe the thermal pairing properties at low  $T$  because at high  $T$  the high-lying excited states should be included in the partition function. When describing the nuclear thermodynamic properties, it is obvious that the more excited states are included in the partition function, the higher  $T$  one can reach. This problem can be resolved by performing the self-consistent quasiparticle random-phase approximation built on top of the LNBCS quasiparticle mean field [117, 118]. This approach, which is abbreviated hereafter as LNSCQRPA, takes into account the ground-state and screening correlations, which are neglected within the conventional BCS and quasiparticle random-phase approximation (QRPA). It has been shown in [117, 118] that these correlations are important as they improve the agreement between the energies of ground state and low-lying excited states obtained within the LNSCQRPA and the corresponding exact results for the doubly-folded equidistant multilevel pairing model. The LNSCQRPA equations, whose formalism is presented in details in [117, 118] for each total seniority  $s$  at  $T = 0$ , are solved only for all the unblocked levels  $k \neq k_s$ , similar to those of the LNBCS described above. The number of LNSCQRPA eigenstates  $\mathcal{E}_{i_s}^{\text{LNSCQRPA}}$  obtained in this case is  $n_{\text{LNSCQRPA}} = \sum_s C_s^\Omega \times (\Omega - s)$ , which is much

higher than that of the LNBCS (see e.g. table I in [116]). Similar to the CE-LNBCS, the partition function of the CE-LNSCQRPA is defined as

$$\begin{aligned} Z_{\text{CE-LNSCQRPA}}(\beta) \\ = \sum_s d_s \sum_{i_s=1}^{n_{\text{LNSCQRPA}}} e^{-\beta \mathcal{E}_{i_s}^{\text{LNSCQRPA}}}. \end{aligned} \quad (75)$$

Based on this partition function, one can obtain all the thermodynamic quantities using (73). Although the number of LNSCQRPA eigenstates is much higher than that of the LNBCS, it is still much lower than the corresponding value obtained within the exact diagonalization of the pairing Hamiltonian. Consequently, the computational time is significantly reduced by about two (four) orders in comparison with the direct diagonalization of the Hamiltonian as listed in table I in [116].

By incorporating the LNBCS and LNSCQRPA eigenvalues into the microcanonical ensemble (MCE), one can obtain the corresponding microcanonical ensemble entropies based on the Boltzmann definition  $\mathcal{S}(\mathcal{E}) = \ln \mathcal{W}(\mathcal{E})$ , where  $\mathcal{W}(\mathcal{E}) = \rho(\mathcal{E}) \delta \mathcal{E}$  is the number of accessible states within the energy interval  $(\mathcal{E}, \mathcal{E} + \delta \mathcal{E})$  with  $\rho(\mathcal{E})$  being the density of states, which is also the total level density comparable to the experimentally observed one [40]. The abbreviations MCE-LNBCS and MCE-LNSCQRPA are used hereafter to denote the corresponding approaches, which embed the LNBCS and LNSCQRPA eigenvalues into the microcanonical ensemble, respectively. Within the canonical ensemble, the total level density  $\rho(\mathcal{E})$  is calculated by using the inverse Laplace transformation of the partition function as

$$\rho(\mathcal{E}) \approx e^{\mathcal{S}(\mathcal{E})} [-2\pi \partial \mathcal{E} / \partial \beta]^{-1/2}, \quad (76)$$

whereas the microcanonical ensemble level density is simply calculated as  $\rho(\mathcal{E}) = e^{\mathcal{S}(\mathcal{E})} / \delta \mathcal{E}$  [21].

Since pairing is significant only for the levels around the Fermi surface [15], the CE-LNBCS (LNSCQRPA) is carried out for a limited number of single-particle levels (truncated space), mostly affected by pairing, namely for 22 degenerate single-particle levels for proton or neutron above a stable core such as  $^{48}\text{Ca}$  core for Mo isotopes or  $^{132}\text{Sn}$  core for Dy and Yb nuclei. The single-particle levels outside this truncated space are treated within the finite-temperature independent-particle model (IPM), where pairing is assumed to have no effect [119]. Consequently, the total partition function is given as

$$\ln Z'_\nu = \ln Z'_{\nu,\text{tr}} + \ln Z'_{\text{sp}} - \ln Z'_{\text{sp},\text{tr}}, \quad (77)$$

where  $Z'_{\nu,\text{tr}} \equiv Z_{\nu,\text{tr}} e^{\beta \mathcal{E}_0}$  is the excitation partition function with respect to the ground state energy  $\mathcal{E}_0$ . In (77),  $Z_{\nu,\text{tr}}$  is the CE-LNBCS (CE-LNSCQRPA) partition function for the truncated space, whereas  $Z'_{\text{sp}}$  and  $Z'_{\text{sp},\text{tr}}$  are the canonical ensemble partition function obtained within the IPM (see e.g. equation (8) of [119]) for the whole (from bottom to  $N(Z) = 126$  level) and truncated spaces, respectively.

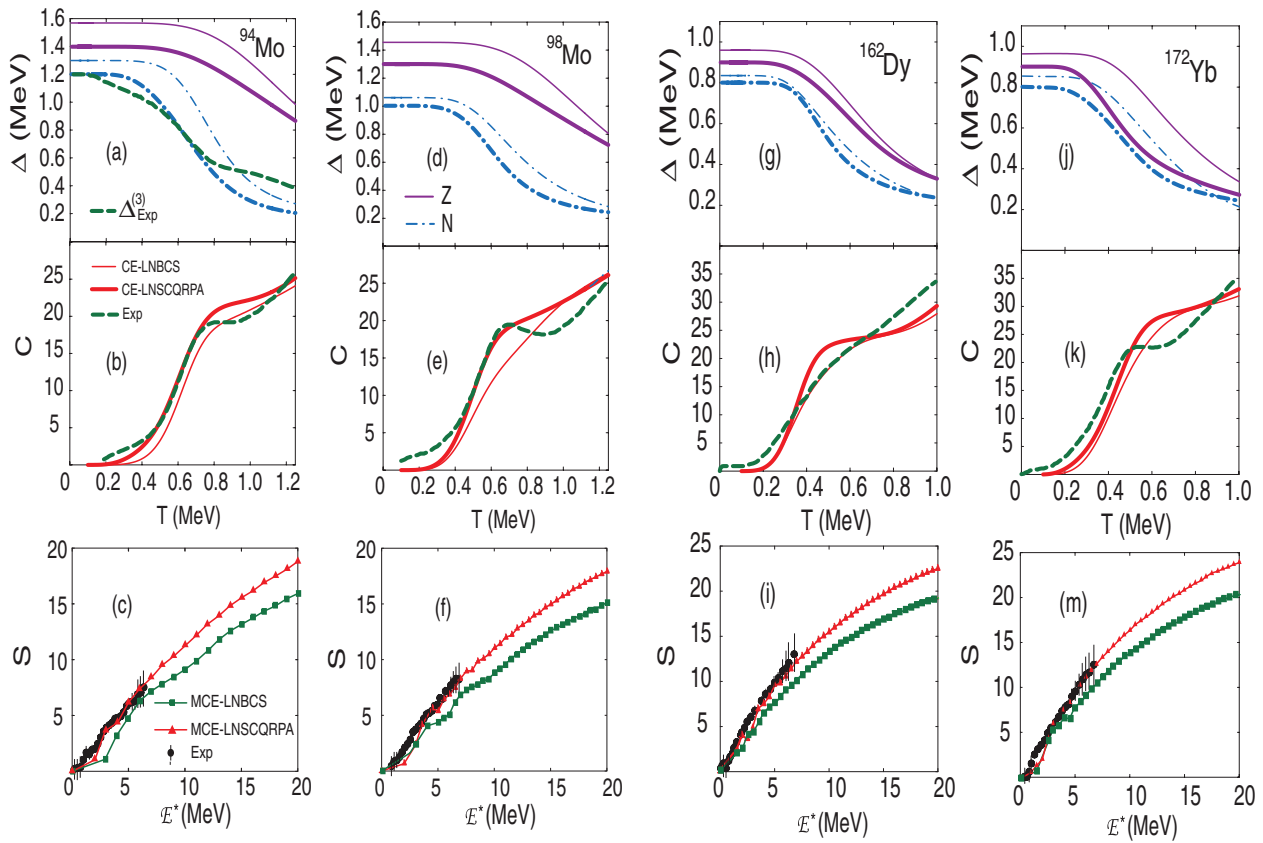


**Figure 38.** Pairing gaps  $\Delta$  and heat capacities  $C$  as functions of  $T$  obtained within the canonical ensemble and entropies  $S$  as functions of  $E^*$  obtained within the microcanonical ensemble for  $^{94,98}\text{Mo}$ ,  $^{162}\text{Dy}$ , and  $^{172}\text{Yb}$  nuclei. In (a), (d), (g) and (j), the solid and dash-dotted lines denote the pairing gaps for protons and neutrons, respectively, whereas the thin and thick lines respectively correspond to the CE-LNBCS and CE-LNSCQRPA results. In (b), (e), (h) and (k), the thin and thick solid lines stand for the CE-LNBCS and CE-LNSCQRPA results, whereas the thick dashed lines depict the experimental results taken from [50, 120, 121], respectively. Shown in (c), (f), (i) and (m) are the MCE entropies obtained within the MCE-LNBCS (squares) and MCE-LNSCQRPA (triangles) and those extracted from experimental data (circles with error bars). Adapted with permission from [116], Copyright (2010) by the American Physical Society.

In figure 38, we show an example of the canonical ensemble pairing gaps  $\Delta$ , canonical ensemble heat capacity  $C$ , and microcanonical ensemble entropy  $S$  obtained within the CE(MCE)-LNBCS and CE(MCE)-LNSCQRPA calculations in comparison with the corresponding experimental data for  $^{94,98}\text{Mo}$ ,  $^{162}\text{Dy}$ , and  $^{172}\text{Dy}$  nuclei. The experimental pairing gap  $\Delta_{\text{Exp}}^{(3)}$  in figure 38(a) is obtained based on the thermal odd-even mass formula (see e.g. equation (11) in [50]), in which the temperature-dependent total energies of the odd and even systems are calculated from the canonical ensemble partition function  $Z(T) = \sum_{i=0}^{\infty} \rho(E_i) e^{-E_i/T} \delta E_i$ , where  $\rho(E_i)$  are the measured total level densities at the excitation energies  $E_i$  and  $\delta E_i$  are the energy bins [50]. The experimental heat capacities shown in figures 38(b), (e), (h) and (k) are also calculated from this partition function (by using (73)). Moreover, the experimental data of microcanonical entropies plotted in figures 38(c), (f), (i) and (m) are obtained from the Boltzmann definition, in which the weight  $\mathcal{W}(E)$  is calculated by using the experimental level density. It is clear from figure 38 that the heat capacities obtained within the CE-LNSCQRPA (thick solid lines) as well as the MCE-LNSCQRPA entropies (triangles) agree quite well with the experimental data for all nuclei under consideration, whereas those obtained within the

CE (MCE)-LNBCS are a bit far from the experimental ones, especially at high  $T$  and/or  $E^*$ . The differences between the results obtained within the CE(MCE)-LNBCS and experimental data should certainly come from the fact that the CE(MCE)-LNBCS contains only the lowest excited states in each total seniority  $s$  configuration as mentioned above. The most interesting feature seen in figure 38 is that all the pairing gaps obtained within either the CE-LNBCS or the CE-LNSCQRPA do not collapse at the critical temperature  $T_C$  as predicted by the conventional BCS, but they all monotonically decrease with increasing  $T$ . Consequently, the sharp peak in the heat capacity, which is the signature of superfluid-normal (SN) phase transition, is smoothed out within these approaches as seen in figures 38(b), (e), (h) and (k). It is also interesting to see in figure 38(a) that the neutron gap obtained within the CE-LNSCQRPA (thick dash-dotted lines) for  $^{94}\text{Mo}$  agrees well the experimental three-point gap [50], indicating that the effect of thermal fluctuations within the CE-LNQRPA is indeed important in the description of thermal pairing in nuclei.

It is also seen in figure 39 that the level densities obtained within the MCE-LNSCQRPA offer the best fit to the experimental data for all nuclei, whereas those obtained within the CE-LNSCQRPA are close to the experimental data in the

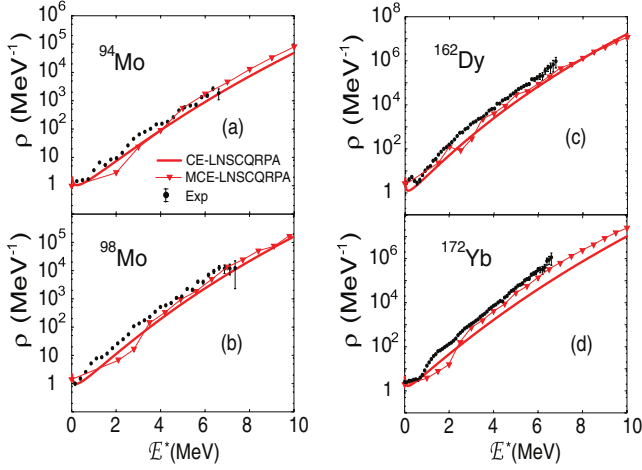


**Figure 39.** Level densities as functions of  $E^*$  obtained within the CE-LNSCQRPA (solid line) and MCE-LNSCQRPA (triangles) versus the experimental data (circles with error bars) for  $^{94}\text{Mo}$ , (a)  $^{98}\text{Mo}$ , (b)  $^{162}\text{Dy}$ , (c) and  $^{172}\text{Yb}$ . (d) Adapted with permission from [116], Copyright (2010) by the American Physical Society.

very low-energy region ( $E^* < 0.5$  MeV) only. The discrepancy between the CE-LNSCQRPA level density and experimental data seen in figures 39(c) and (d) seems to be larger and increases with  $E^*$  for heavy isotopes such as  $^{162}\text{Dy}$  and  $^{172}\text{Yb}$ . The reason might be due to the absence of the rotational and vibrational enhancements as well as the contributions of higher multiplicities such as dipole, quadrupole, etc, which are not included in this study.

#### 4.3. Exact solutions within the canonical and microcanonical ensembles

The exact solution of the pairing Hamiltonian was introduced for the first time by Richardson since 1960s [132–134]. The Richardson’s method allows one to solve exactly the pairing Hamiltonian (by solving the so-called Richardson’s equations) of the systems with the number of particle ranging from the very small ( $N = 2$ ) to very large ( $N = 1000$ ) ones [135]. However, this method is rather complex and provides only the ground state and very few low-lying excited states of the system, which are certainly not sufficient for constructing the exact partition function at finite temperature. Recently, by applying the  $\text{SU}(2)$  algebra of angular momentum, the pairing Hamiltonian can be represented in a new set of basis states  $|k\rangle$ , which depend on the partial seniority  $s_k$  (number of unpaired particles on the  $k$ th orbitals) and partial occupation number  $N_k$ . In this basis states, the pairing Hamiltonian can be directly diagonalized to obtain all the eigenvalues (excited states)  $\mathcal{E}_{i_s}^{\text{ex}}$  and eigenvectors (eigenstates)  $|s\rangle$  at different total seniority  $s$ . Based on these eigenvalues, we can construct the exact partition function within the CE

$$Z_{\text{ex}} = \sum_s d_s \sum_{i_s} e^{-\beta \mathcal{E}_{i_s}^{\text{ex}}}, \quad (78)$$

which is similar as (72) but with the use of exact eigenstates instead of the LNBCS or LNSCQRPA ones. Consequently, all the thermodynamic quantities are calculated based on this

partition function, that is, by using (73), except that the exact pairing gap is calculated based on the following relation

$$\Delta_{\text{ex}} = \sqrt{-G\mathcal{E}_{\text{pair}}}, \quad \mathcal{E}_{\text{pair}} = \mathcal{E} - \mathcal{E}_0, \quad (79)$$

$$\mathcal{E}_0 = 2 \sum_k \left( \epsilon_j - \frac{G}{2} f_k \right) f_k, \quad (80)$$

where the exact temperature-dependent occupation numbers  $f_k$  are calculated from the state-dependent occupation numbers  $f_k^{i_s}$  via  $f_k(\beta) = \frac{1}{Z(\beta)} \sum_s d_s \sum_{i_s} f_k^{(i_s)} e^{-\beta \mathcal{E}_{i_s}^{\text{ex}}}$ . Knowing all the excited states, we can easily calculate the microcanonical ensemble weight  $\mathcal{W}(E) = \rho(E)\delta E$  and microcanonical ensemble entropy  $\mathcal{S}(E) = \ln \mathcal{W}(E)$  as presented in section 4.2. At the same time, we can also calculate the microcanonical ensemble temperature based on the relation  $\beta = 1/T = \partial \mathcal{S}(E)/\partial E$ . Moreover, the microcanonical ensemble temperature of each eigenstate  $T_{i_s}$  can be calculated based on the first derivative of state entropy with respect to the eigenstate  $\mathcal{E}_{i_s}^{\text{ex}}$  [136]

$$S^{(i_s)} = - \sum_k [C_k^{(i_s)}]^2 \ln [C_k^{(i_s)}]^2, \quad (81)$$

where  $(C_k^{(i_s)})^2$  are the weights of the eigenvector components, namely  $|s\rangle = \sum_k C_k^{(i_s)} |k\rangle$  with  $\sum_k [C_k^{(i_s)}]^2 = 1$  [40].

Figure 40 plots an example of exact canonical ensemble and microcanonical ensemble calculations for a doubly-folded equidistant multilevel pairing model, which is also called the Richardson (or ladder) model [137, 138], with number of single-particle levels  $\Omega = 10$  and number of particles  $N = \Omega$ . It is seen from this figure that the pairing gap obtained within the exact canonical ensemble (thick solid lines) decreases with increasing  $T$  but it does not vanish at  $T = T_c$  as that of the conventional BCS (thin dashed lines). Instead, it monotonically decreases with increasing  $T > T_c$  and is still finite even at  $T$  as high as 5 MeV. At the same time, the bump or the discontinuity in the heat capacity predicted within the BCS, which is the signature of superfluid-normal phase transition in finite systems, is smoothed out within the exact canonical ensemble. These results obtained within the exact canonical ensemble are confirmed by those calculated within the two approximations, namely the CE-LNBCS (thick dashed lines) and CE-LNSCQRPA (thin solid lines) as presented in section 4.2. As for the microcanonical ensemble, the state temperatures  $T_{i_s}$  (figure 40(d)) obtained by using the state entropy (81) scatter around the canonical ensemble temperature, indicating the strong fluctuation in this finite small system (with only  $N = 10$  particles moving in  $\Omega = N$  single-particle levels). Many  $T_{i_s}$  values are even negative because they are related to the spread of the exact eigenvectors over the unperturbed basis state  $k$  and therefore do not need to follow the trend of the canonical ensemble temperatures. With increasing the energy interval  $\delta E$  to account for more number of levels, the values of microcanonical ensemble temperature gradually converge to the canonical ensemble ones (figures 40(e) and (f)). This observation means that within the microcanonical ensemble, the thermal equilibrium can be reached only if the system is very large (i.e.  $N$  and  $\Omega$  are very large or infinite but  $N/\Omega$  is

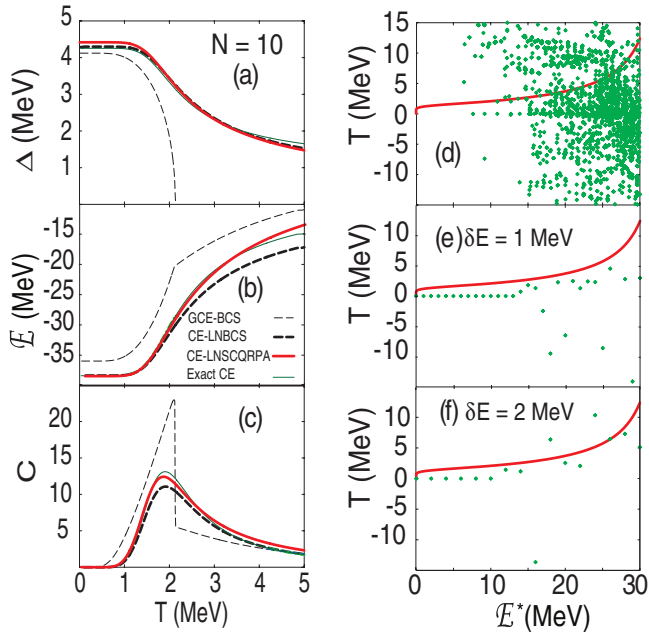


**Figure 40.** (a)–(c) Pairing gap  $\Delta$ , total energy  $\mathcal{E}$ , heat capacity  $C$  as functions of  $T$  obtained within the conventional BCS (thin dashed lines), CE-LNBCS (thick dashed lines), CE-LNSCQRPA (thin lines), and exact CE (thick lines) for the Richardson model with  $N = \Omega = 10$  and  $G = 1$  MeV. (d)–(f) State temperatures  $T_{i_s}$  (d) obtained from the state entropy (81) and MCE temperatures ((e) and (f)) obtained using two different values of energy interval  $\delta\mathcal{E} = 1$  MeV (e) and  $\delta\mathcal{E} = 2$  MeV (f) in the MCE weight  $\mathcal{W}(E)$  for the Richardson model with  $N = \Omega = 10$  and  $G = 0.9$  MeV. The solid lines in (d)–(f) are the temperatures obtained from the CE for the same system. Adapted with permission from [40, 115], Copyright (2009 and 2010) by the American Physical Society.

finite) and its spectrum is very dense (very small level spacings), for example within the metal superconductors, ultracold gases, liquid helium, etc.

It is well-known that a direct measurement of the nuclear pairing gap  $\Delta$  at finite  $T$  is impossible. At  $T = 0$ ,  $\Delta$  is conventionally extracted based on the odd–even mass difference between the binding energy (ground-state energy) of the  $N$ -particle systems and its neighboring ones with  $N \pm 1$  particles as [15]

$$\Delta^{(3)}(N) = \frac{(-1)^N}{2} [\mathcal{E}(N-1) - 2\mathcal{E}(N) + \mathcal{E}(N+1)], \quad (82)$$

where  $\mathcal{E}(N-1)$ ,  $\mathcal{E}(N)$ , and  $\mathcal{E}(N+1)$  are ground-state energies of the systems with  $N-1$ ,  $N$ , and  $N+1$  particles, respectively. The pairing gap defined in (82) is called the three-point gap. A more precise formula, called the four-point gap, which is calculated based on the arithmetic average of the three-point gap, is sometime used, namely [15]

$$\Delta^{(4)}(N) = \frac{1}{2} [\Delta^{(3)}(N) + \Delta^{(3)}(N-1)]. \quad (83)$$

At  $T \neq 0$ , the simplest way to empirically determine the temperature-dependent pairing gap is to extend the three-point and four-point formulas to finite temperature, namely

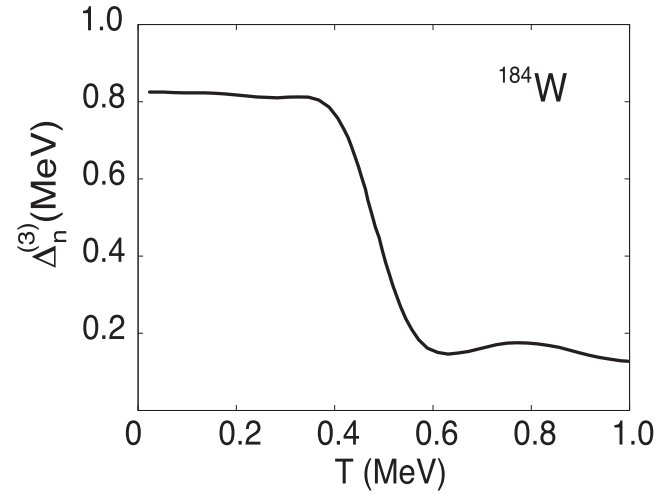


**Figure 41.** Neutron gap  $\Delta_n^{(3)}$  as a function of temperature extracted from the thermal three-point odd–even mass formula using the experimental level densities. Adapted with permission from [39], Copyright (2005) by the American Physical Society.

$$\Delta^{(3)}(N, T) = \frac{(-1)^N}{2} [\mathcal{E}(N-1, T) - 2\mathcal{E}(N, T) + \mathcal{E}(N+1, T)], \quad (84)$$

$$\Delta^{(4)}(N, T) = \frac{1}{2} [\Delta^{(3)}(N, T) + \Delta^{(3)}(N-1, T)], \quad (85)$$

where  $\mathcal{E}(N, T)$  is the total thermal energy of the system with  $N$  particle obtained within the canonical ensemble. The formulas (84) and (85) have been used in [39] and [50] to extract the thermal pairing gaps of  $^{184}\text{W}$  and  $^{94-96}\text{Mo}$  based on their experimental nuclear level densities (see e.g. figure 41). However, there is a drawback of the gaps defined in this way as they still contain the contribution from the uncorrelated single-particle configurations, which increases with  $T$ . Consequently, the pairing gaps defined in (84) and (85) are not valid at  $T \neq 0$ , that is, they are not comparable to the BCS-like pairing gap defined in (79). To remove the contribution of uncorrelated single-particle energies, we have proposed in [40] an improved odd–even mass formula at  $T \neq 0$ , namely

$$\tilde{\Delta}^{(3)}(N, T) = \frac{G}{2} \left[ (-1)^N + \sqrt{1 - 4\frac{S'}{G}} \right], \quad (86)$$

where  $S' = \frac{1}{2} [\mathcal{E}(N+1, T) - \mathcal{E}(N-1, T)] - \mathcal{E}_0(N, T)$  with  $\mathcal{E}_0(N, T)$  being calculated from (80). This quantity  $S'$  is obviously different from the conventional odd–even mass formula due to the presence of the uncorrelated single-particle energy  $\mathcal{E}_0$ , which is zero only at  $G = 0$  (zero-pairing case). The value of  $S'$  is always negative because the absolute value of the uncorrelated energy  $\mathcal{E}_0$  is larger than that of the total (correlated) energy  $\mathcal{E}$  (see e.g. (79)). The modified gap  $\tilde{\Delta}^{(3)}(N, T)$ , as compared to the gap  $\Delta^{(3)}(N, T)$  defined in (84), is therefore closer to the exact canonical ensemble gap in (79) as it excludes the contribution of uncorrelated single-particle

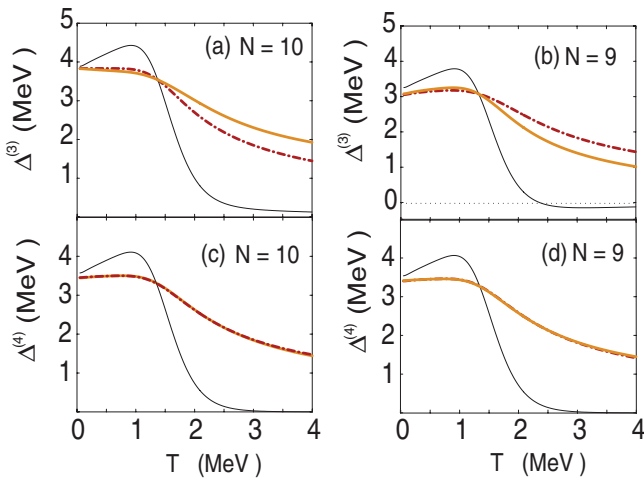


**Figure 42.** Three-point and four-point pairing gaps extracted from the odd–even mass differences as functions of  $T$  for the Richardson model with  $N = 10$  ((a) and (c)) and  $N = 9$  ((b) and (d)) ( $\Omega = 10$ ,  $G = 0.9$  MeV). The thin solid lines are the gaps extracted from (84) and (85), whereas the thick solid lines denote the corresponding modified gaps. The dashed-dotted lines are the exact CE gap  $\Delta_{\text{ex}}$ . Adapted with permission from [40], Copyright (2009) by the American Physical Society.

motions. It is worth noting here that the energies  $\mathcal{E}(N + 1, T)$  and  $\mathcal{E}(N - 1, T)$  in (86) can be obtained from experiments, e.g. from the experimental level density, whereas the energy  $\mathcal{E}_0$  is a model-dependent quantity being calculated based on the single-particle energies  $\epsilon_k$  (temperature independent) and single-particle occupation number  $f_k$  (temperature dependent). Similarly, the modified four-point gap  $\tilde{\Delta}^{(4)}(N, T)$  can be obtained from the modified three-point ones by using e.g. formula (85).

In figure 42, we plot the three-point and four-point gaps extracted from (84) and (85) together with their modified ones versus the exact canonical ensemble gap (79) obtained within the Richardson model with for the cases of even  $N = 10$  and odd  $N = 9$  particle numbers ( $\Omega = 10$  and  $G = 0.9$  MeV). It is easily seen from this figure 42 that the simple extension of the odd–even mass formula to  $T \neq 0$ , which leads to the gaps  $\Delta^{(3)}$  and  $\Delta^{(4)}$ , fails to match the exact canonical ensemble gap  $\Delta_{\text{ex}}$ . The three-point gap  $\Delta^{(3)}$  for  $N = 9$  even turns to unphysically negative at  $T > 2.4$  MeV, indicating that this simple extension is invalid. Meanwhile, the modified gaps  $\tilde{\Delta}^{(3)}$  is in much better agreement with the exact canonical ensemble one. At  $T < 1.5$  MeV, the modified three-point gap  $\tilde{\Delta}^{(3)}$  is almost the same as  $\Delta_{\text{ex}}$ , whereas it becomes higher (smaller) than  $\Delta_{\text{ex}}$  at higher  $T$ . This discrepancy, however, decreases with increasing the particle number. At the same time, the modified four-point gap  $\tilde{\Delta}^{(4)}$  coincides with  $\Delta_{\text{ex}}$ . This result clearly indicates that the modified gap defined in formula (86) is a much better candidate for determining the experimental pairing gap at  $T \neq 0$  rather than the simple extension of odd–even mass differences (84) and (85).

By directly diagonalizing the cranking Hamiltonian  $H - \omega M$ , where  $H$  is given in equation (1) and  $\omega$  is the rotational frequency, for a degenerate spherical shell and a single deformed  $j$  shell in clusters and nuclei and incorporating

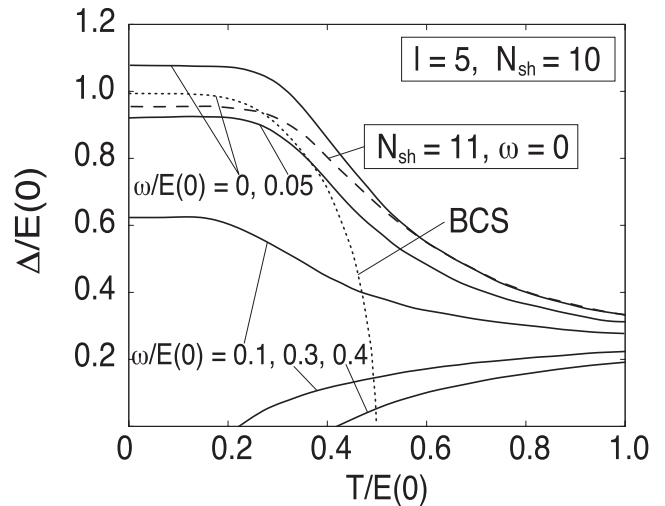


**Figure 43.** Exact pairing gap as a function of temperature and rotational frequency obtained within the exact canonical-ensemble solution for a single-shell Hamiltonian (degenerate model) with even  $N_{\text{sh}} = 10$  (thick lines) and odd  $N_{\text{sh}} = 11$  (dashed line) particle numbers. The dotted line stands for the conventional BCS gap.  $E(0)$  denotes the ground-state energy, which is around 0.3–0.4 MeV for Al clusters and 0.8–1.5 MeV for nuclei. Adapted with permission from [46], Copyright (2003) by the American Physical Society.

the solutions into the canonical ensemble (using e.g. equations (78)–(80)), the authors of [46] have studied the evolution of exact pairing gap with temperature and rotational frequency. The obtained pairing gap (figure 43) is qualitatively similar as the exact canonical gap shown in figure 40. Increasing the rotational frequency makes the pairing gap at low temperature decrease and quench when the rotational frequency is sufficiently high, which is similar as that predicted by the BCS theory with the fixed total angular momentum  $M$  instead of the rotational frequency (see e.g. figure 1). When the pairing gap is quenched by the effect of rotation, increasing temperature gradually makes it reappear. However, different from the prediction of the BCS theory discussed in section 2, the reappearance of pairing gap (pairing reentrance) occurs in such a way that it increases with temperature and remains always finite at higher temperatures as seen in figure 43. This behavior of pairing reentrance is known to be caused by the effect of thermal fluctuations in finite systems as metallic clusters and/or atomic nuclei.

#### 4.4. Shell model Monte Carlo method at finite temperature

The Monte Carlo method was introduced for the first time in 1960s in order to describe the ground-state properties of very light nuclei with  $A = 3$  or 4 particles [122]. Since 1980s, with the development of computer technology, this method was extensively enlarged and applied to describe the structure of atomic nuclei, especially the binding energy of light nuclei such as triton [123] and alpha particle [124]. Since then the Monte Carlo method based on shell model (shell-model Monte-Carlo method) has been strongly developed and successfully applied to describe not only the ground state ( $T = 0$ ) but also thermal ( $T \neq 0$ ) properties of medium-mass nuclei [125], which are beyond the reach of the the conventional shell model. The shell-model Monte Carlo method (SMMC) is derived based on the

Monte Carlo evaluation of the path integral, making use of the Hubbard–Stratonovich transformation of the imaginary-time evolution operator [110, 111], instead of the direct diagonalization of the Hamiltonian as in the shell model. By doing so, it is able to reduce the many-body problem to a set of one-body problems in the auxiliary fields. The SMMC, which is presented in detail in [36, 126, 127], can be summarized as follows.

The SMMC considers a shell-model Hamiltonian of the form [126]

$$H = \sum_{\alpha} \epsilon_{\alpha} \mathcal{O}_{\alpha} + \frac{1}{2} \sum_{\alpha} V_{\alpha} \mathcal{O}_{\alpha}^2, \quad (87)$$

where  $\epsilon_{\alpha}$  are related to the single-particle energies, whereas  $\mathcal{O}_{\alpha}$  are a set of one-body operators and  $V_{\alpha}$  characterize a two-body residual interaction. The operator  $\mathcal{O}_{\alpha}$  can refer to one particle (quasiparticle) densities. The SMMC describes the thermal properties of the Hamiltonian  $H$  (87) at the inverse temperature  $\beta = 1/T$  based on the Gibbs ensemble  $e^{-\beta H}$  [128]. Within the SMMC, the inverse temperature  $\beta$ , which is also called the imaginary time, is divided into  $N_t$  equal time intervals (slices)  $\Delta\beta = \beta/N_t$ . Consequently, the exponent  $e^{-\beta H}$  can be expressed in terms of evolution operator  $U$  of the form

$$U = [\exp(-\Delta\beta H)]^{N_t}. \quad (88)$$

By using the Hubbard–Stratonovich transformation for the  $n$ th time slice, one obtains the following approximation [126]

$$\begin{aligned} \exp(-\Delta\beta H) &\simeq \int_{-\infty}^{\infty} \prod_{\alpha} d\sigma_{\alpha n} \left( \frac{\Delta\beta |V_{\alpha}|}{2\pi} \right)^{1/2} \\ &\times \exp \left[ -\Delta\beta \left( \sum_{\alpha} \frac{1}{2} |V_{\alpha}| \sigma_{\alpha n}^2 + \epsilon_{\alpha} \mathcal{O}_{\alpha} + s_{\alpha} V_{\alpha} \sigma_{\alpha n} \mathcal{O}_{\alpha} \right) \right], \end{aligned} \quad (89)$$

where  $s_{\alpha}$  is the phase factor, which is equal to  $\pm 1$  if  $V_{\alpha} < 0$  and  $\pm i$  if  $V_{\alpha} > 0$ , whereas  $\sigma_{\alpha n}$  is the auxiliary field associated with  $\mathcal{O}_{\alpha}$  at the time slice  $n$ . Based on the Hubbard–Stratonovich transformation (89), the evolution operator (88) can be approximated as

$$U \simeq \int D^{N_t}[\sigma] \times G(\sigma) \exp[-\Delta\beta h_{\sigma}(\tau_{N_t})] \dots \exp[-\Delta\beta h_{\sigma}(\tau_1)], \quad (90)$$

where the integration measure  $D^{N_t}[\sigma]$  and Gaussian factor  $G(\sigma)$  are given by

$$\begin{aligned} D^{N_t}[\sigma] &= \prod_{n=1}^{N_t} \prod_{\alpha} d\sigma_{\alpha n} \left( \frac{\Delta\beta |V_{\alpha}|}{2\pi} \right)^{1/2}, \\ G(\sigma) &= \exp \left( -\sum_{\alpha n} \frac{1}{2} |V_{\alpha}| \sigma_{\alpha n}^2 \right). \end{aligned} \quad (91)$$

The one-body Hamiltonian in (90) has the following form [126]

$$h_{\sigma}(\tau_n) = \sum_{\alpha} (\epsilon_{\alpha} + s_{\alpha} V_{\alpha} \sigma_{\alpha n}) \mathcal{O}_{\alpha}. \quad (92)$$

By using the integrals (89) and (90), the conventional shell-model calculation in the large matrix space is reduced to the

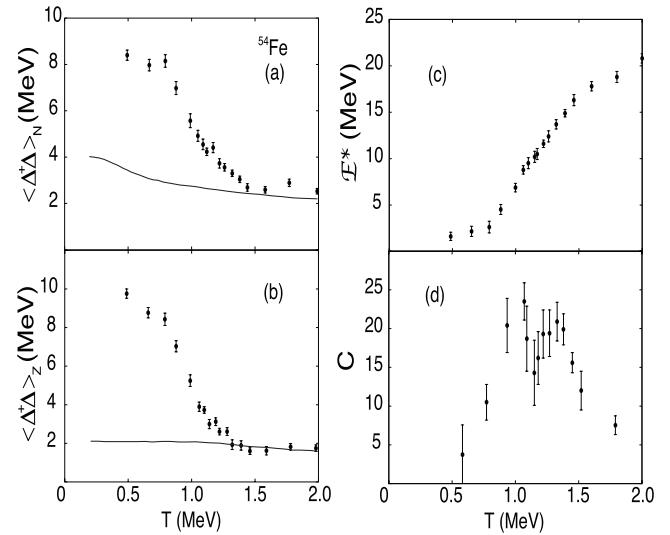


**Figure 44.** Total excitation energy  $\mathcal{E}^*$ , heat capacity  $C$ , squares of neutron  $\langle \Delta^{\dagger} \Delta \rangle_N$  and proton  $\langle \Delta^{\dagger} \Delta \rangle_Z$  pairing gaps as functions of  $T$  obtained within the SMMC for  $^{54}\text{Fe}$  nucleus. Solid curves in (a) and (b) stand for the corresponding pairing gaps calculated from the uncorrelated Fermi gas. Adapted with permission from [36], Copyright (1997) by Elsevier.

calculation of path integrals in the single-particle space. This path integrals over  $\sigma$  are then evaluated by using the Monte Carlo method [36].

Within the SMMC, the thermal average of any observable  $O$  is given as [128]

$$\langle O \rangle = \frac{\text{Tr}(O e^{-\beta H})}{\text{Tr}(e^{-\beta H})} = \frac{\int D[\sigma] W_{\sigma} \Phi_{\sigma} \langle O \rangle_{\sigma}}{\int D[\sigma] W_{\sigma} \Phi_{\sigma}}, \quad (93)$$

where  $D[\sigma] = \lim_{N_t \rightarrow \infty} D^{N_t}[\sigma]$ ,  $W_{\sigma} = G_{\sigma} |\text{Tr} U_{\sigma}|$ , and  $\langle O \rangle_{\sigma} = \text{Tr}(O U_{\sigma}) / \text{Tr} U_{\sigma}$ . In (93),  $\Phi_{\sigma}$  is the Monte Carlo sign, which is defined as  $\Phi_{\sigma} = \text{Tr} U_{\sigma} / |\text{Tr} U_{\sigma}|$ . The trace in (93) can be evaluated within either the grand canonical ensemble or canonical ensemble. Within the grand canonical ensemble, the trace of one-body evolution operator  $U_{\sigma}$  is defined as [127]

$$\text{Tr} U_{\sigma} = \det(\mathbf{1} + \mathbf{U}_{\sigma}), \quad (94)$$

where  $\mathbf{U}_{\sigma}$  is the  $N_s \times N_s$  matrix representing  $U_{\sigma}$  in the  $N_s$  single-particle levels, which are used in the shell-model Hamiltonian (87). Practically, the SMMC employs the canonical ensemble, which can be obtained from the grand canonical ensemble by applying an exact particle-number projection [127].

Within the SMMC, the canonical ensemble partition function  $Z$  can be calculated based on the relation  $-\partial \ln Z / \partial \beta = \mathcal{E}(\beta)$ , where the total energy  $\mathcal{E}(\beta)$  is obtained from the expectation value of the Hamiltonian within the canonical ensemble, namely  $\mathcal{E}(\beta) = \langle H \rangle$ . Knowing the partition function, one can easily calculate all the thermodynamic quantities (using e.g. (73)) as well as level density (76).

Figure 44 shows an example of the SMMC calculation for  $^{54}\text{Fe}$  nucleus using the realistic Brown–Richter Hamiltonian [129] in the complete set of  $1p_{3/2,1/2} 1f_{7/2,5/2}$  states. It is shown in this figure that the expectation values of the proton–proton  $\langle \Delta^{\dagger} \Delta \rangle_Z$  and neutron–neutron  $\langle \Delta^{\dagger} \Delta \rangle_N$  pairing fields, whose square-root values respectively correspond to

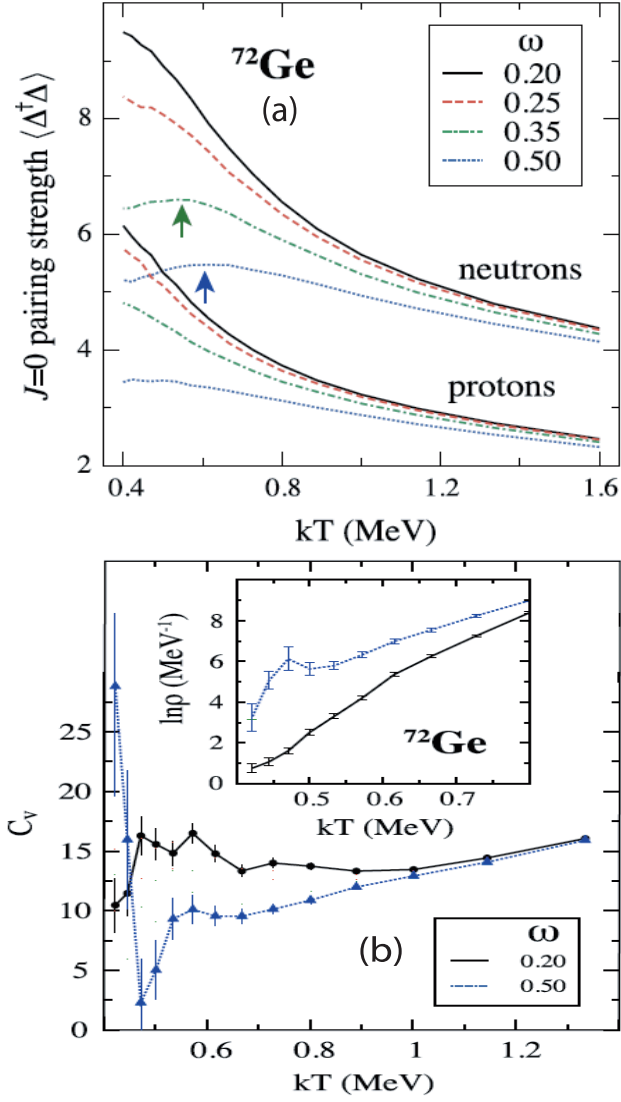


**Figure 45.** Neutron and proton pairing strengths  $\Delta^\dagger \Delta$  (a) and heat capacity (b) versus temperature obtained within the SMMC for  $^{72}\text{Ge}$  at several values of rotational frequency  $\omega$ . The inset in (b) shows the calculated logarithm of total level density. Adapted with permission from [52], Copyright (2010) by the American Physical Society.

the proton and neutron pairing gaps, are significantly higher than those obtained within a non-interacting Fermi gas in the low-temperature region  $0 \leq T \leq 1.5$  MeV. This result indicates a strong effect of thermal and quantal fluctuations, similar to that found in the static path approximation and CE-LNBCS(LNSCQRPA) calculations presented in sections 4.1 and 4.2, respectively. It is also seen from figure 44 that at  $T > 1.1$  MeV, the heat capacity  $C$  starts to decrease due to the limit of the model space ( $fp$  shell) used in the SMMC calculation. To have a right trend of  $C$  at high  $T$ , the SMMC should be combined with the IPM calculation using (77) [119].

The SMMC has been extended to study the thermal properties of heated rotating nuclei by considering the Routhian  $H^\omega = H - \omega J_z$ , where  $J_z$  is the projection of total angular momentum along the cranking  $z$ -axis, which is the same as the angular-momentum projection  $M$  used in section 2 [52, 130, 131]. Figure 45 shows an example of the SMMC calculation for

a  $^{72}\text{Ge}$  nucleus by using a pairing plus quadrupole-quadrupole Hamiltonian with constant pairing strength  $G$  [52]. This figure indicates that the neutron and proton pairing strengths  $\Delta^\dagger \Delta$ , whose square root is proportional to the pairing gap  $\Delta$ , decrease with increasing temperature but remain finite at  $T > 1.6$  MeV (figure 45(a)). However, at high rotational frequency  $\omega \geq 0.35$  MeV, the neutron pairing locally increases to reach a maximum at low temperatures as indicated by the arrows in figure 45(a). The associated heat capacity at  $\omega = 0.5$  MeV seen in figure 45(b) shows a local dip at low temperatures, whereas the level density obtained at the same  $\omega$  shows a significant enhancement in the same temperature region. The low-temperature irregularity in the observation of the heat capacity and level density, indeed, is the signature of pairing reentrance phenomenon in this heated rotating  $^{72}\text{Ge}$  nucleus as explained in [52].

## 5. Experimental evidences

### 5.1. Experimental evidence of pairing reentrance in nuclei

A series of experiments has been recently conducted at the Bhabha Atomic Research Center (BARC) for the reaction  $^{12}\text{C} + ^{93}\text{Nb} \rightarrow ^{105}\text{Ag}^* \rightarrow ^{104}\text{Pd}^* + p$  at the incident energy of 40–45 MeV [54–58]. The proton spectra have been measured in coincidence with a  $\gamma$ -ray multiplicity detector array, which consists of 14 bismuth germanate (BGO) detectors arranged in two closed-packed groups of seven [55]. Details on the experiment can be found e.g. in [54, 55]. The measured proton spectra at different folds, which correspond to the number of BGO detectors used to generate the outputs in the prompt coincidence with the signals from NaI(Tl) (used to detect protons), are shown in figure 46 along with the fitting results obtained within the statistical model calculations using the CASCADE computer program [139]. Within the latter, the following Fermi-gas level density formula, which is a function of the excitation energy  $E^*$  and total angular momentum  $J$ , has been used [54]

$$\rho(E^*, J) = \frac{2J+1}{12\sigma^{3/2}} \sqrt{a} \frac{\exp(2\sqrt{aU})}{U^{3/2}}, \quad (95)$$

where  $U = E^* - E_{\text{rot}} - \Delta P$ ,  $E_{\text{rot}} = \frac{\hbar^2}{2\mathcal{I}} J(J+1)$ ,  $a = \tilde{a} [1 - \frac{\Delta S}{U} (1 - e^{-\gamma U})]$ ,  $\gamma = 0.4A^{4/3}/\tilde{a}$ , and  $\sigma = 2\mathcal{I}/\hbar^2$  with  $\mathcal{I}$ ,  $\Delta S$ , and  $\Delta P$  being the effective rigid-body moment of inertia, shell correction, and pairing energy, respectively. Here, the level density parameter  $\tilde{a}$  is chosen to be  $A/8.6$  MeV $^{-1}$ , which is consistent with that obtained from the previous experiments [140, 141]. The shell correction  $\Delta S$  is defined from the difference between the experimental and liquid drop masses. The calculated proton spectra, obtained by using the conventional nuclear level density (95), are plotted as the dashed lines in figure 46. It is easy to see from this figure that these calculated spectra do not agree with the experimental data, especially in the region of proton energy  $E_p^{c.m.} > 16$  MeV in the center of mass, where the broad structures were observed [54, 57, 58]. To obtain the best fit to the measured spectra, the conventional nuclear level density (95) is multiplied with an empirical enhancement function

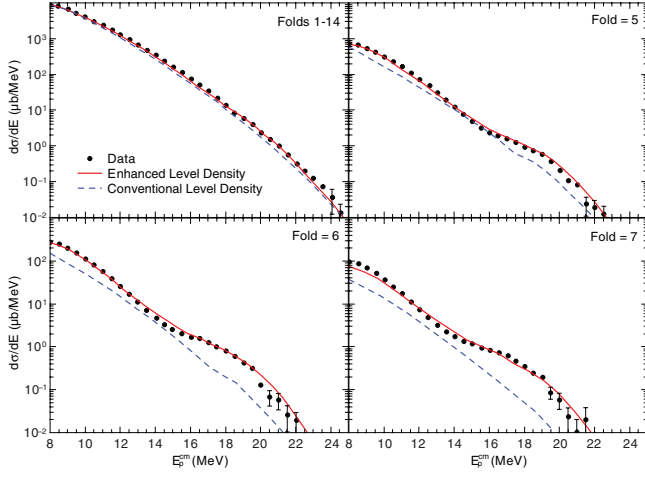


**Figure 46.**  $\gamma$ -multiplicity gated spectra of proton obtained within the  $^{12}\text{C} + ^{93}\text{Nb}$  reaction at  $E(^{12}\text{C}) = 40$  MeV. The solid and dash lines stand for the fitted results obtained within the CASCADE code, which uses the conventional and enhanced level densities, respectively. Adapted with author's permission from [58].

$$\varepsilon(E^*, J) = 1 + Kf(E^*)g(J), \quad (96)$$

where

$$f(E^*) = \begin{cases} \exp\left[-\frac{(U-E_c)^2}{2\sigma_X^2}\right], & \text{if } U > E_c, \\ 1, & \text{if } U \leq E_c, \end{cases} \quad (97)$$

$$g(J) = \begin{cases} \exp\left[-\frac{(J-J_c)^2}{2\sigma_J^2}\right], & \text{if } J > J_c, \\ 1, & \text{if } J \leq J_c. \end{cases} \quad (98)$$

Here,  $E_c$  and  $J_c$  are, respectively, the critical excitation energy and angular momentum, whereas the  $\sigma_X$  and  $\sigma_J$  correspond to the full width at half maximums (FWHM) of the excitation-energy and angular-momentum distributions, respectively. The best fitted values of these quantities are found to be  $K = 30$ ,  $E_c = 3$  MeV,  $J_c = 18\hbar$ ,  $\sigma_J = 3$  MeV, and  $\sigma_X = 3.5 - 0.06J$  MeV [54, 55]. With the use of enhanced level density (96), the agreement between the experimental and calculated spectra becomes much better than the use of conventional level density as shown in figure 46.

In figure 47, we show an example of level densities obtained by using the conventional (95) and enhanced (96) formulas as functions of  $T$  at  $J = 20\hbar$ . It is interesting to see from figure 47 that the enhancement of level density observed in this  $^{104}\text{Pd}$  nucleus is qualitatively similar to that predicted by the SMMC for  $^{72}\text{Ge}$  [52] at nearly the same  $T$  and  $J$  values. This result suggests that the pairing reentrance phenomenon might have actually been observed in this  $^{104}\text{Pd}$  nucleus. However, in order to confirm this, one needs to perform the theoretical calculation within a microscopic approach for the same nucleus at the same  $T$  and  $J$  values. To do so, we have employed a theory of so-called the BCS1, which is the BCS theory incorporating the effect of quasiparticle-number fluctuations at finite temperature and finite angular momentum. The BCS1 equations are derived basically in the same way as the conventional BCS ones presented

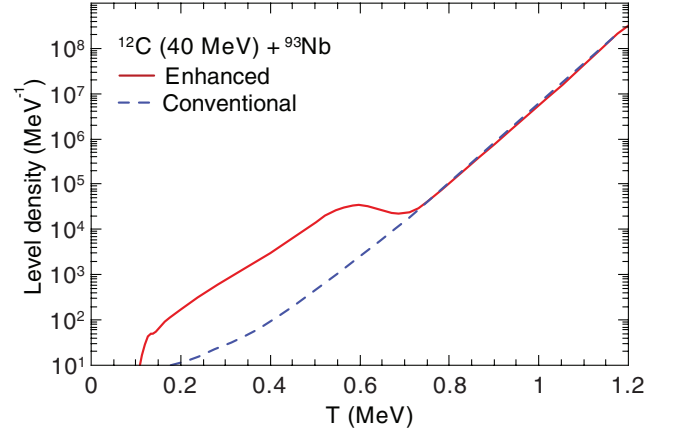


**Figure 47.** Conventional and enhanced level densities versus temperature for  $^{104}\text{Pd}$  nucleus at  $J = 20\hbar$  (adapted with author's permission from [58]).

in section 2, namely employing the variational procedures to minimize the expectation value of the pairing Hamiltonian  $H - \lambda N - \gamma M$  within the grand canonical ensemble. Detail on the derivation of the BCS1 equations can be found in [38, 53]. The final form of the BCS1 equations for the pairing gap  $\Delta$ , particle number  $N$ , and total angular momentum  $M$  is given as

$$\begin{aligned} \Delta_k &= \Delta + \delta\Delta_k, \\ N &= 2 \sum_k \left[ v_k^2 (1 - n_k^+ - n_k^-) + \frac{1}{2} (n_k^+ - n_k^-) \right], \\ M &= \sum_k m_k (n_k^+ - n_k^-), \end{aligned} \quad (99)$$

where  $\Delta = G \sum_{k'} u_{k'} v_{k'} (1 - n_{k'}^+ - n_{k'}^-)$  is similar as the conventional BCS gap, whereas  $\delta\Delta_k = G u_k v_k \delta\mathcal{N}_k^2 / (1 - n_k^+ - n_k^-)$  is level-dependent and contains the quasiparticle-number fluctuations at finite temperature and angular momentum  $\delta\mathcal{N}_k^2 = (\delta\mathcal{N}_k^+)^2 + (\delta\mathcal{N}_k^-)^2 = n_k^+ (1 - n_k^+) + n_k^- (1 - n_k^-)$ . Here the quasiparticle occupation numbers,  $n_k^\pm$ , quasiparticle energy,  $E_k$ , and Bogoliubov coefficients  $u_k$  and  $v_k$ , are defined as usual as

$$\begin{aligned} u_k^2 &= \frac{1}{2} \left( 1 + \frac{\epsilon_k - Gv_k^2 - \lambda}{E_k} \right), & v_k^2 &= 1 - u_k^2, \\ E_k &= \sqrt{(\epsilon_k - Gv_k^2 - \lambda)^2 + \Delta_k^2}, \\ n_k^\pm &= \frac{1}{1 + e^{(E_k \mp \gamma m_k)/T}}. \end{aligned} \quad (100)$$

By solving the BCS1 equations, one can obtain all the thermodynamic quantities such as level-weighted pairing gaps  $\bar{\Delta} \equiv \sum_k \Delta_k / \Omega_L$  with  $\Omega_L$  being the number of single-particle levels  $k$  for neutrons ( $N$ ) and proton ( $Z$ ), total energy  $\mathcal{E} = \mathcal{E}_N + \mathcal{E}_Z$ , total entropy  $\mathcal{S} = \mathcal{S}_N + \mathcal{S}_Z$ , and consequently total grand-partition function  $\Omega = \Omega_N + \Omega_Z = \mathcal{S} + \alpha_N N + \alpha_Z Z + \mu M - \beta \mathcal{E}$  ( $\alpha = \lambda/T$ , and  $\mu = \omega/T$ ). The angular-momentum dependent level density  $\rho(E, M)$  is then calculated using (14). The  $J$ -dependent level density  $\rho(\mathcal{E}, J)$  can be obtained by

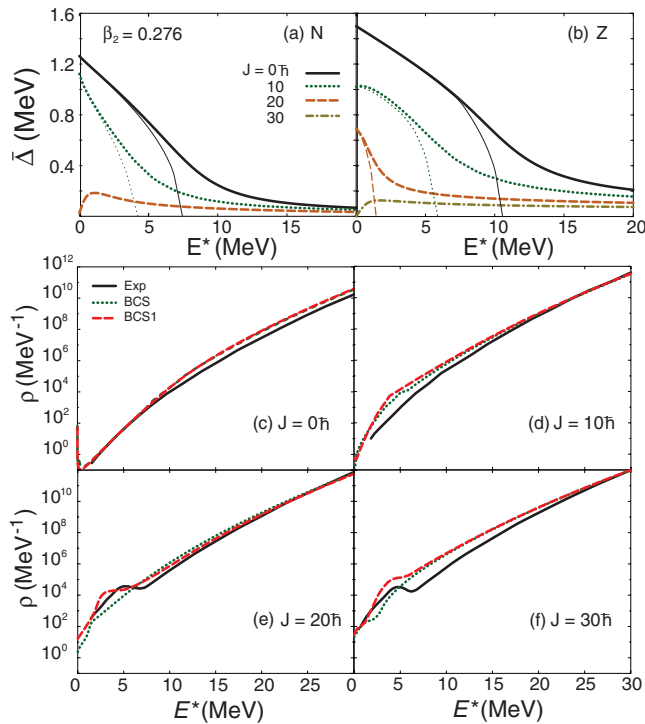


**Figure 48.** Level-weighted pairing gaps  $\bar{\Delta}$  for neutron (N) (a) and protons (Z) (b) and total level densities (c)–(f) as function of excitation energy  $E^*$  obtained within the BCS and BCS1 by using the quadrupole deformation parameter  $\beta_2 = 0.276$ . The thin and thick lines in (a) and (b) denote the BCS and BCS1 results, respectively, whereas the dotted and dashed lines in (c)–(f) respectively stand for the BCS and BCS1 total level densities. The solid lines in (c)–(f) are the experimentally extracted data. Reprinted from [59]. CC BY 3.0.

differentiating  $\rho(\mathcal{E}, M)$  as discussed in section 2.3, namely  $\rho(\mathcal{E}, J) = \rho(\mathcal{E}, M = J) - \rho(\mathcal{E}, M = J + 1)$ .

Figure 48 shows the neutron and proton pairing gaps  $\bar{\Delta}_{N(Z)}$  (a) and (b) and level densities  $\rho(\mathcal{E}, M)$  (c)–(f) as function of excitation energy  $E^* = \mathcal{E}(T, M) - \mathcal{E}(0, M)$  obtained within the BCS and BCS1 for  $^{104}\text{Pd}$  nucleus at a fixed value of quadrupole deformation parameter  $\beta_2$  of the axially deformed Woods–Saxon potential [142] and different values of  $J$ . It is seen that the pairing gaps obtained within the conventional BCS (thin lines) at all  $J$  decrease with increasing  $E^*$  and collapse at some critical values  $E_c^*$ , which become smaller when  $J$  is higher. When  $J$  is higher than its critical value  $J_c$ , which is about  $20\hbar$  for neutron and  $30\hbar$  for proton, the BCS gaps completely disappear. At the same time, by including the quasiparticle-number fluctuations, the BCS1 gaps do not collapse but monotonically decrease with increasing  $E^*$  and remain finite even at  $E^* > 30$  MeV. At  $J = 20\hbar$  for neutron and  $J = 30\hbar$  for protons, where the BCS gaps are all zero, the pairing reentrance is clearly seen in the BCS1 gaps. As a result, while there is no enhancement of level density obtained within the BCS, two local enhancements are seen in the BCS1 level densities, in qualitative agreement with the experimentally extracted (empirical) data at exactly two values of  $J = 20$  and  $30\hbar$ , where the pairing reentrance takes place for neutrons and protons, respectively.

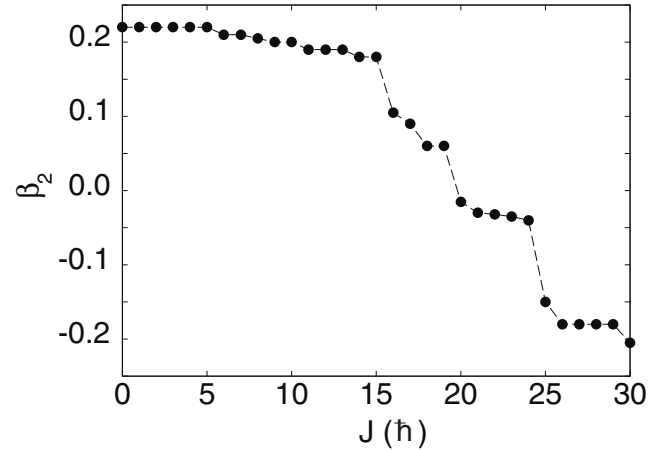


**Figure 49.** Quadrupole deformation parameter  $\beta_2$  of the axially deformed Woods–Saxon potential as functions of the total angular momentum  $J$  obtained within the BCS (BCS1). Reprinted from [60]. CC BY 4.0.

To have a better description, we have adjusted the deformation parameter  $\beta_2$  so that the level densities obtained within the BCS1 fit best the empirical data, especially in the region where the enhancement of level density is observed. The values of  $\beta_2$  obtained in this way are plotted versus  $E^*$  in figure 49. It is seen in figure 49 that  $\beta_2$  decreases from a positive value of 0.22 at  $J = 0\hbar$  to a negative one at around  $J = 20\hbar$ . This variation of  $\beta_2$  clearly indicates a shape transition from the prolate shape ( $\beta_2 > 0$ ) to the oblate one ( $\beta_2 < 0$ ), which is reasonable in this mass region because of the alignment of protons in  $g_{9/2}$  and neutrons in  $h_{11/2}$  single-particle orbitals [143, 144]. As a result, the BCS1 gaps change slightly as compared to the case in which  $\beta_2$  is fixed, namely pairing reentrance is seen in the proton and neutron gaps at  $J = 20\hbar$  and  $30\hbar$ , respectively (see figures 50(a) and (b)). Interestingly, the BCS1 level densities are in much better agreement with the empirical data than those obtained within the case of fixed  $\beta_2$ , especially in the region where the enhancement of level densities is observed (see figures 50(c)–(f)).

All the results of the microscopic calculations within the BCS and BCS1 theories shown above clearly indicate that the observed enhancement of level density as seen in figure 47 might be the first experimental evidence of pairing reentrance phenomenon in a hot rotating nucleus.

## 5.2. Condensed-matter counterpart: magnetic-field-induced superconductivity

The behavior of hot rotating nuclei can be put in correspondence with superconductors in the presence of an external magnetic field, where the latter plays the same role as that of the nuclear rotation. In general, the application of a sufficiently strong magnetic field destroys the superconducting state in a superconductor because of the Zeeman effect, which breaks the paired electrons in a spin-singlet state, and the orbital effect, where the vortices penetrating into the superconductors annihilate the energy gain from creating the paired electrons. However, the study of the interplay of superconductivity and magnetism in the recent past has experimentally observed that

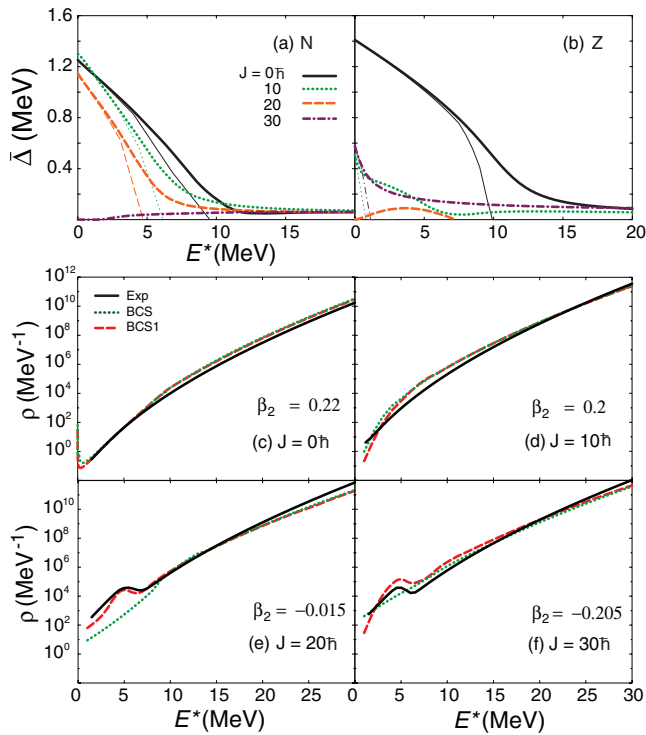


**Figure 50.** Same as figure 48 but using different values of  $\beta_2$  shown in figure 49. Reprinted from [60]. CC BY 4.0.

a high magnetic field can also induce superconductivity in a number of materials at low temperatures [31, 145–150].

**5.2.1. Magnetic-field-induced superconductivity based on Jaccarino–Peter compensation effect.** In [145, 146], a magnetic-field-induced superconductivity (MFIS) has been observed in the europium-containing metallic compound  $\text{Eu}_x\text{Sn}_{1-x}\text{Mo}_6\text{S}_8$  added with a small amount of Br or Se, where  $x$  ranges from 0.7 to 0.8. In the sample  $\text{Eu}_{0.75}\text{Sn}_{0.25}\text{Mo}_6\text{S}_{7.2}\text{Se}_{0.8}$ , the data at the lowest temperature ( $T = 0.37$  K) on the diagram of the normalized electrical resistance  $R/R_N$  versus applied magnetic field  $H$  shown in the inset of figure 51(a) reveal that, with increasing  $H$ , an S-N-S-N succession of transitions from the superconducting (S) state to the normal (N) one takes place. Two separate domains of magnetic-field-induced superconductivity are found at low and high fields (figure 51(a)). While in a conventional superconductor only the one at low fields exists, the high-field domain spans from 4 to 22 T at  $T = 0$  and extends from  $T = 0$  to 1 K at the field magnitude of 12 T. This phenomenon is interpreted in terms of the Jaccarino–Peter compensation mechanism [151], according to which the high-field domains occur as a result of a balance between the externally applied field and the effective exchange field, which arises from the internal interaction of conduction electrons with the ions in the lattice. The negative exchange interaction between the magnetic moments and the conduction electrons can compensate the internal field of the electrons, which is antiparallel to the external one. As a result, the Zeeman effect ceases to work when the both fields are completely cancelled out.

A similar magnetic-field-induced superconductivity has been observed in a heavy-fermion system and, at the same time, a simple cubic system, namely  $\text{CePb}_3$  in [147], where

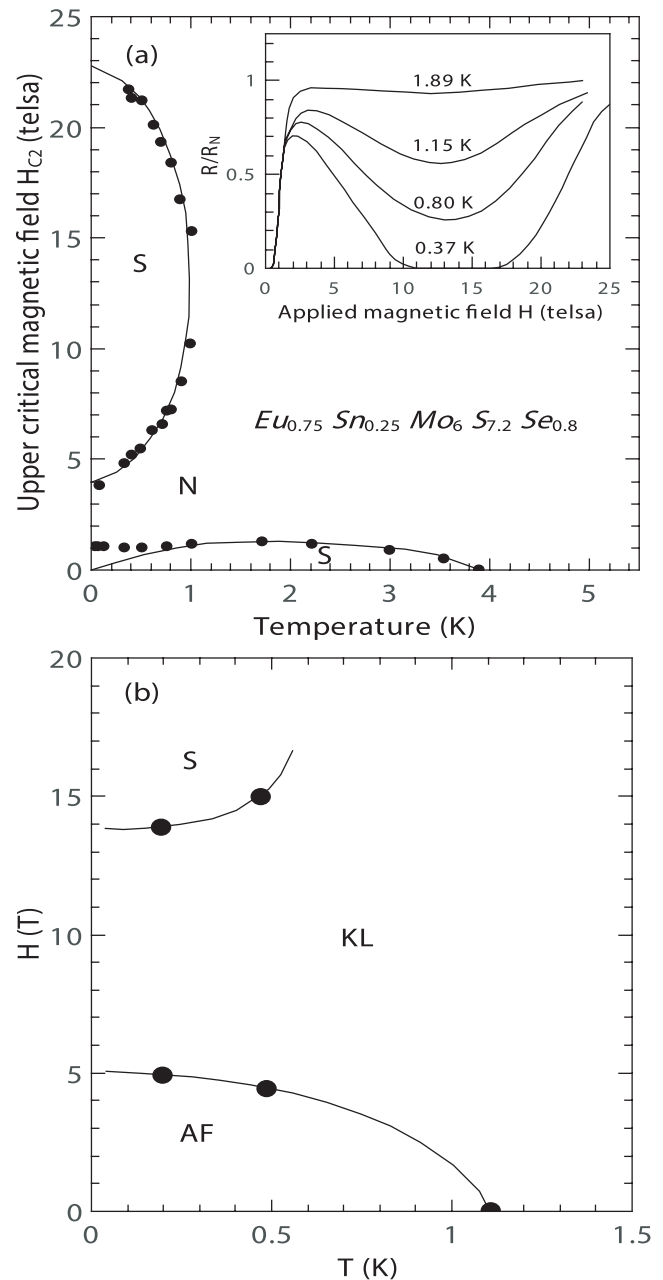


**Figure 51.** (a) Magnetic field-temperature phase diagram for the sample  $\text{Eu}_{0.75}\text{Sn}_{0.25}\text{Mo}_6\text{S}_{7.2}\text{Se}_{0.8}$ . The upper critical magnetic field  $H_{C2}$ , above which superconductivity is destroyed, is the upper bound of the region for the values of the applied magnetic field to penetrate into the interior of a type-II superconductor. The solid circles are the measurements in [145, 146], whereas the solid lines are the results of calculations according to the multiple pair breaking theory [152]. The inset shows the normalized electrical resistance  $R/R_N$  versus the applied magnetic field at several temperatures. Adapted with permission from [145], Copyright (1984) by the American Physical Society. (b) The same phase diagram for  $\text{CePb}_3$ , where AF, S, and KL stand respectively for antiferromagnetic, superconducting, and Kondo lattice. Adapted with permission from [147], Copyright (1985) by the American Physical Society.

at  $T = 0.2$  K a magnetic field of 14 T induces the system into the superconducting state, whereas at  $T = 0.48$  K, a field of 15 T drives the sample to be superconducting (figure 51(b)). The difference as compared to the magnetic-field-induced

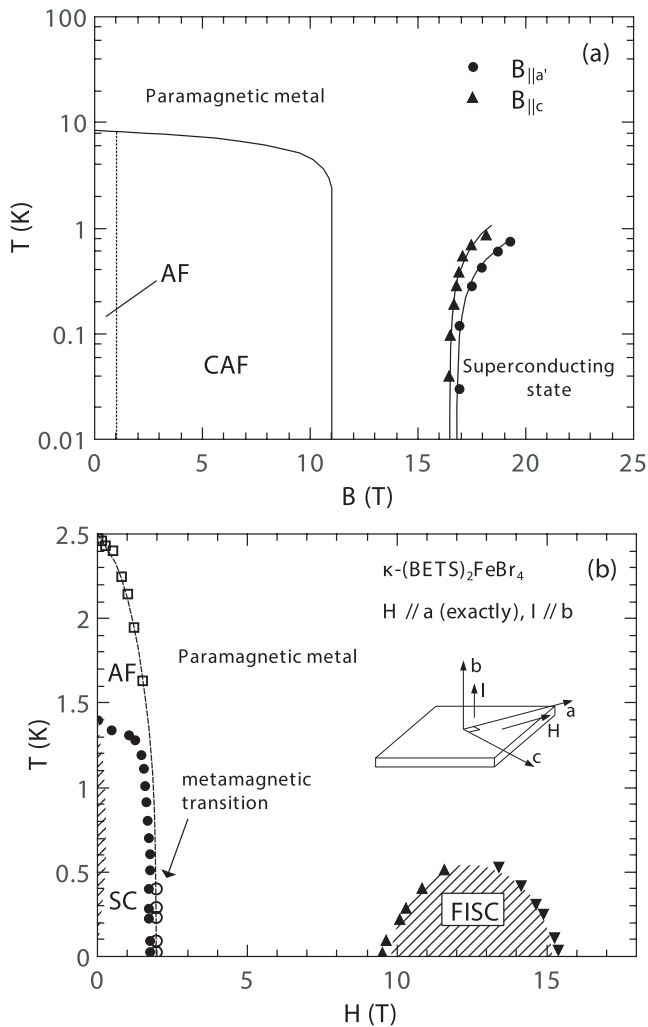


**Figure 52.** (a) Magnetic field-temperature phase diagram for  $\lambda$ -(BETS)<sub>2</sub>FeCl<sub>4</sub> when the magnetic field is parallel to the conduction layer  $a$ - $c$ . At zero field, a metal-insulator transition occurs at  $T \approx 8$  K. In the insulating phase, the Fe moments are AF ordered, whereas CAF stands for canted AF. The magnetic-field-induced superconductivity is seen at above 17 T. Adapted with permission from [148], Copyright (2001) by Springer Nature. (b) The same phase diagram for  $\kappa$ -(BETS)<sub>2</sub>FeBr<sub>4</sub> when the field is parallel to the  $a$ -axis. Closed circles, open circles/squares, and closed triangles are the superconducting, metamagnetic, and magnetic-field-induced superconductivity transitions, respectively. The shaded area shows the superconducting phase predicted by the multiple pair breaking theory [152]. Adapted with permission from [149], Copyright (2004) by the American Physical Society.

superconductivity in [145, 146] (figure 51(a)) is in the domain below 5 T, which is an antiferromagnetic (AF) phase, characterizing CePb<sub>3</sub>.

The magnetic-field-induced superconductivity also takes place in organic conductors. In [148], it has been observed that, at temperature  $T = 0.1$  K, a magnetic field above 17 T, which is applied exactly parallel to the conducting layers in the crystal of the quasi-2D  $\lambda$ -(BETS)<sub>2</sub>FeCl<sub>4</sub> with BETS being bis(ethylenedithio)teraselefulvalene, induces superconductivity (figure 52(a)). Although the Jaccarino–Peter compensation arisen from the exchange interaction between the Fe moments and the conduction electrons might have caused the

magnetic-field-induced superconductivity in this case, this effect cannot explain why the magnetic-field-induced superconductivity is observed only when the applied magnetic field is strictly parallel to the conducting layers. The strong anisotropy in inducing the superconductivity suggests that the low dimensionality of the electronic system strongly affects the emergence of superconductivity, and it is likely that magnetic fluctuations through the paramagnetic Fe moments have led to the pairing interaction between the conduction electrons and the BETS molecules.

In [149], the magnetic-field-induced superconductivity has been detected in quasi-2D organic conductor  $\kappa$ -(BETS)<sub>2</sub>FeBr<sub>4</sub>, which is a salt that undergoes the antiferromagnetic order of the Fe<sup>3+</sup> spins at  $T = 2.5$  K, with the magnetic easy axis along the  $a$ -axis in the 2D conduction layer  $a$ - $c$ , and is superconducting at  $T < 1.4$  K. As the magnetic field increases, which is applied exactly parallel to the  $a$ -axis, superconductivity is first broken at  $T = 1.8$  K. At  $T = 27$  mK, the resistance increase almost linearly with the applied magnetic field above 2 T, and then abruptly drops by three orders of magnitude at the field magnitude above 8 T. In the region of the field magnitudes between 11 T and 14 T, the resistance drops to zero, signaling the magnetic-field-induced superconductivity. The magnetic-field-induced superconductivity vanishes at the field further increases above 17 T. It also becomes unstable with increasing the temperature, and almost suppressed at  $T = 0.81$  K. The magnetic field—temperature diagram of the magnetic-field-induced superconductivity for  $\kappa$ -(BETS)<sub>2</sub>FeBr<sub>4</sub> is shown in figure 52(b). The authors of [148, 149] concluded that the magnetic-field-induced superconductivity caused by the Jaccarino–Peter compensation effect should be a universal phenomenon in the low-dimensional systems with large magnetic moments and negative strong exchange interaction between conducting electrons and magnetic moments.

**5.2.2. Unconventional magnetic-field-induced superconductivity: Reentrant superconductivity.** All the magnetic-field-induced superconductivity cases based on the Jaccarino–Peter compensation effect discussed in section 5.2.1 have the induced moment parallel to the applied magnetic field. In contrast, for the ferromagnetic superconductor URhGe, where the superconducting temperature  $T_{sc}$ , below which the material is superconducting, is smaller than the Curie temperature  $T_c$  (9.5 K) in the absence of the applied magnetic field. This result means that the superconducting phase coexists with the ferromagnetic one and the reentrant superconductivity has been discovered [31] when the applied magnetic field is directed along the  $b$ -axis, that is perpendicular to the direction of easy magnetization (the  $a$ - $c$  plane). It has been found that, at a sufficiently low temperature, such an applied magnetic field suppresses the superconducting state, but at a much high field of about 8 T the superconducting phase is recreated and exists up to the applied-field magnitude of about 13 T with the maximum  $T_{sc}$  equal to around 0.4 K (figure 53). The appearance of reentrant superconductivity is explained by the strong increase in the magnetic susceptibility, which corresponds to the longitudinal magnetic fluctuations in the vicinity of the first-order phase transition in both ferromagnetic and paramagnetic states.

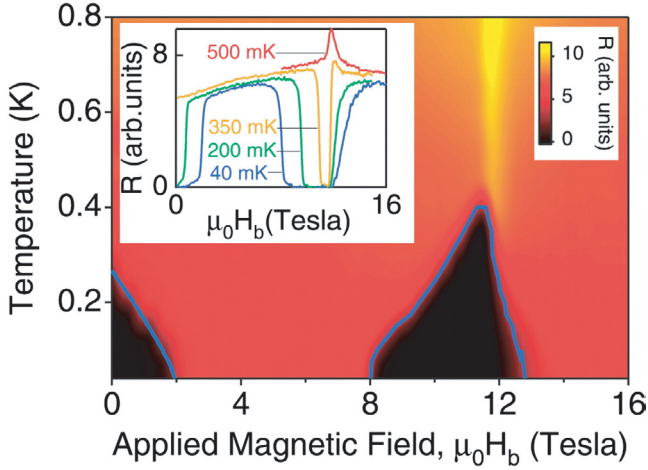


**Figure 53.** Magnetic field-temperature phase diagram for URhGe when the magnetic field is parallel to the  $b$ -axis. The black domains are the zero-resistivity regions, where superconductivity takes place. The maximum transition temperature corresponds to the field magnitude, at which the resistivity has a peak at a higher temperature. The (blue) solid lines show the position, where the resistance reaches a value equal to half of that in its normal state. The inset shows the resistance as a function of the applied magnetic field at several temperatures, which correspond to the horizontal cuts through the main panel. Reprinted with permission from [31], Copyright (2005) by Science.

## 6. Role of pairing in properties of excited nuclei

### 6.1. Effect of thermal pairing on giant dipole resonance in hot nuclei

**6.1.1. Effect of BCS pairing on energy and line shape.** The most popular theory among microscopic approaches to collective excitations is the theory of small amplitude vibrations called the random-phase approximation (RPA), or quasiparticle RPA (QRPA) in the quasiparticle representation including pairing. The QRPA at finite temperature, abbreviated hereafter as FT-QRPA, describes the excitations generated by the coherent superpositions of the quasiparticle-pair operators in thermal equilibrium, which define the QRPA phonon operator  $Q_\nu^\dagger$  in the form

$$Q_\nu^\dagger = \sum_{k>l} \left( \frac{X_{kl}^\nu A_{kl}^\dagger - Y_{kl}^\nu A_{kl}}{\sqrt{D_{kl}}} + \frac{x_{kl}^\nu B_{kl}^\dagger - y_{kl}^\nu B_{kl}}{\sqrt{d_{kl}}} \right), \quad (101)$$

where

$$\begin{aligned} A_{kl}^\dagger &= \alpha_k^\dagger \alpha_l^\dagger, & B_{kl}^\dagger &= \alpha_k^\dagger \alpha_l, \\ A_{kl} &= (A_{kl}^\dagger)^\dagger, & B_{kl} &= (B_{kl}^\dagger)^\dagger, \end{aligned} \quad (102)$$

with  $\alpha_{k(l)}^\dagger$  ( $\alpha_{k(l)}$ ) being the quasiparticle creation (annihilation) operators of the single-particle levels  $k(l)$  as defined in (5). The average values of the commutators between the quasiparticle pair creation  $A_{kl}^\dagger$  and annihilation  $A_{kl}$  operators, and those between quasiparticle scattering  $B_{kl}^\dagger$  and  $B_{kl}$  operators in the grand canonical ensemble read

$$\begin{aligned} \langle [A_{kl}, A_{k'l'}^\dagger] \rangle &= \delta_{kk'} \delta_{ll'} D_{kl}, & D_{kl} &= (1 - n_k - n_l), \\ \langle [B_{kl}, B_{k'l'}^\dagger] \rangle &= \delta_{kk'} \delta_{ll'} d_{kl}, & d_{kl} &= (n_l - n_k), \end{aligned} \quad (103)$$

where the quasiparticle occupation number  $n_k \equiv \langle \alpha_k^\dagger \alpha_k \rangle$  is defined, as usual, by the Fermi–Dirac distribution of the quasiparticle with energy  $E_k$  at temperature  $T$ , namely  $n_k = 1/[\exp(\beta E_k) + 1]$ . The pairing gap  $\Delta(T)$  in the quasiparticle energy  $E_k \equiv \sqrt{(\epsilon_k - \lambda - Gv_k^2)^2 + \Delta^2(T)}$  is found by solving the BCS, modified BCS and/or the BCS1 equations at finite temperature. The last two cases include the effect of the thermal fluctuation of the quasiparticle numbers which is neglected in the conventional BCS theory as mentioned in the Introduction and section 5. Here, the coefficients of the Bogoliubov transformation  $u_k$  and  $v_k$  have their conventional forms (see e.g. (100)), in which the term  $Gv_k^2$  is often omitted because of its small contribution or its effect is already included in the phenomenological mean-field potential, such as the Woods–Saxon one.

The FT-QRPA equations are usually obtained by linearizing the equations of motion  $\langle [A_{kl}^\dagger, [H - \lambda N, Q_\nu^\dagger]] \rangle = \omega \langle [A_{kl}^\dagger, Q_\nu^\dagger] \rangle$  and  $\langle [B_{kl}^\dagger, [H - \lambda N, Q_\nu^\dagger]] \rangle = \omega \langle [B_{kl}^\dagger, Q_\nu^\dagger] \rangle$  under the assumption that the phonon operators (101) are ideal boson ones, that is  $\langle [Q_\nu, Q_{\nu'}^\dagger] \rangle = \delta_{\nu\nu'}$ , which, together with the quasiboson approximation (103), leads to the normalization condition  $\sum_{k>l} (X_{kl}^\nu X_{kl}^{\nu'} - Y_{kl}^\nu Y_{kl}^{\nu'} + x_{kl}^\nu x_{kl}^{\nu'} - y_{kl}^\nu y_{kl}^{\nu'}) = \delta_{\nu\nu'}$ .

The finite-temperature RPA, abbreviated as FT-RPA, and FT-QRPA equations are the set of equations obtained within the quasiboson approximation for the eigenvectors  $X_{kl}^\nu$ ,  $Y_{kl}^\nu$ ,  $x_{kl}^\nu$  and  $y_{kl}^\nu$ , as well as the eigenvalues  $\omega_\nu$ , which are the energies of phonon excitations. The use of a separable residual interaction  $V_{klk'l'} = \kappa^{(L)} F_{kl}^{(L)} (F_{k'l'}^{(L)})^*$ , where  $\kappa^{(L)}$  is the strength parameter (positive for isovector and negative for isoscalar particle-hole ( $ph$ ) matrix elements) and  $L$  denotes the multipolarity, allows the elimination of the amplitudes  $X_{kl}^\nu$ ,  $Y_{kl}^\nu$ ,  $x_{kl}^\nu$  and  $y_{kl}^\nu$  to obtain a dispersion equation for the phonon energies  $\omega$  in the form [153]

$$1 + \kappa^{(L)} \sum_{k>l} [F_{kl}^{(L)}]^2 \times \left[ \frac{[u_{kl}^{(+)}]^2 (E_k + E_l) D_{kl}}{\omega^2 - (E_k + E_l)^2} - \frac{[v_{kl}^{(-)}]^2 (E_k - E_l) d_{kl}}{\omega^2 - (E_k - E_l)^2} \right] = 0, \quad (104)$$

with  $u_{kl}^{(+)} = u_k v_l + v_k u_l$ ,  $v_{kl}^{(-)} = u_k u_l - v_k v_l$ . At zero pairing,  $u_{ph}^{(+)} = 1$  and  $v_{pp'}^{(-)} = v_{hh'}^{(-)} = 0$ , the second sum on the left-hand side of (104) vanishes, and one recovers from it the RPA dispersion equation [154, 155].

The effect of pairing on the energy of the giant dipole resonance within the FT-QRPA was obtained in [28] for the spherical nucleus  $^{58}\text{Ni}$  and is shown in figure 54. When the QRPA phonon operators are constructed from the superpositions of two BCS quasiparticle operators, the energy of the giant dipole resonance weakly decreases with the temperature  $T$  in the ranges  $0 < T \ll T_c$  and  $T > T_c$ . Near the critical temperature  $T_c$ , it shows a sudden bending down with a break at  $T_c$ . The same feature was reported within the FT-QRPA for the rotating deformed nucleus  $^{164}\text{Er}$  in [27]. The decrease in the energy of the giant dipole resonance with the temperature is a feature of the FT-RPA but the sudden bending at the critical temperature

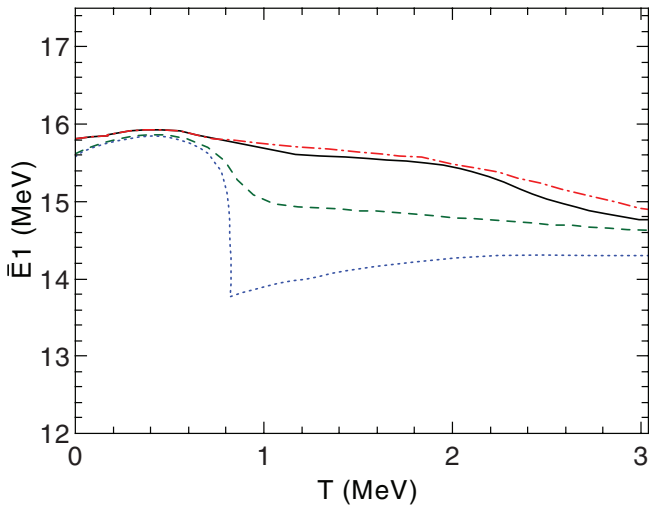


**Figure 54.** Centroid energies of the isovector giant dipole resonance in  $^{58}\text{Ni}$  as functions of  $T$ . The dotted, dashed, and solid lines represent the results obtained within by using the conventional BCS gap  $\Delta$ , thermal average gap  $\langle\Delta\rangle$  according to section 2 without particle-number projection, and  $\langle\bar{\Delta}\rangle$  including the particle-number projection within the Lipkin–Nogami method, respectively. The dash-dotted line corresponds to the result obtained with zero-temperature BCS gap  $\Delta(0)$ . Adapted from [156]. *copy*; IOP Publishing Ltd. All rights reserved.

$T_c$  is caused by the collapse of the pairing gap at this critical temperature within the BCS theory. Thermal fluctuations of the pairing field smooth out this singularity as has been shown in [156].

**6.1.2. Effect of modified BCS and exact pairing on width of giant dipole resonance within phonon-damping model.** Similarly to the BCS1 at finite temperature, the modified BCS (MBCS) also considers the thermal fluctuations of the pairing field in terms of the quasiparticle-number fluctuation [37]. This is realized by using the secondary transformation from quasiparticle operators  $\alpha_k^\dagger$  and  $\alpha_k$  to modified quasiparticle ones,  $\bar{\alpha}_k^\dagger$  and  $\bar{\alpha}_k$ , *viz.*,

$$\begin{aligned}\bar{\alpha}_k^\dagger &= \sqrt{1-n_k}\alpha_k^\dagger - \sqrt{n_k}\alpha_{-k}, \\ \bar{\alpha}_{-k} &= \sqrt{1-n_k}\alpha_{-k} + \sqrt{n_k}\alpha_k^\dagger.\end{aligned}\quad (105)$$

The modified BCS equations are obtained in the form

$$\bar{\Delta} = G \sum_k [(1-2n_k)u_k v_k - \sqrt{n_k(1-n_k)}(u_k^2 - v_k^2)], \quad (106)$$

$$N = 2 \sum_k [(1-2n_k)v_k^2 + n_k - 2\sqrt{n_k(1-n_k)}u_k v_k], \quad (107)$$

with the last terms on the right-hand side of (106) and (107) arising because of the quasiparticle-number fluctuation  $\sqrt{\delta\mathcal{N}_k^2} \equiv \sqrt{n_k(1-n_k)}$ .

The MBCS theory has met some critics from the authors of [157], who claimed that it is thermodynamically inconsistent. Their tests show that, depending on the configuration space, the MBCS gap may become negative or diverge at a certain temperature far above the critical temperature  $T_c$ , where the

BCS gap collapses. However, as has been pointed out in [158], their analysis is inadequate to judge the MBCS applicability because of the following main reasons.

Firstly, the claim of thermodynamical inconsistency within the MBCS was made based on the principle of compensation of dangerous diagrams. The latter was postulated to define the coefficients  $u_j$  and  $v_j$  of the Bogoliubov canonical transformation. This postulation and the variational calculation of the pairing Hamiltonian lead to equation (19) in [157], which requires that the coefficients in the terms containing the operators of quasiparticle number  $\mathcal{N}_j \equiv \sum_m \alpha_{jm}^\dagger \alpha_{jm}$  and quasiparticle pair  $\mathcal{A}_j^\dagger \sim \sum_m \alpha_{jm}^\dagger \alpha_{jm}^\dagger$  should vanish in the ground state of the BCS theory. This postulate is justified so long as divergences can be removed from the perturbation expansion of the ground-state energy. However, at finite temperature, a temperature-dependent ground state does not exist. Instead, one should use the expectation values over the canonical or grand canonical ensemble. Therefore, equation (19) of [157] no longer holds, as has been shown by numerical check in figure 3 of [158]. This invalidates the claim by the authors of [157] that the MBCS theory is thermodynamically inconsistent.

Secondly, the results of the test made in [157] were obtained either in the temperature region, where the use of temperature-independent single-particle spectra is no longer valid (for  $^{120}\text{Sn}$  and Ni isotopes), or within too limited configuration spaces, namely the doubly degenerate equidistant and half-filled model with  $N = 10$  particles or two major shells for Ni isotopes. The calculations using the temperature-independent realistic single-particle spectrum for neutrons in  $^{120}\text{Sn}$  [37], and within an extended configuration spaces [158] have shown that the MBCS is a good approximation up to high temperature even for a system with  $N = 10$  particles.

Finally, in [159], a systematic test of the MBCS theory has been conducted by using the exactly solvable Richardson model. The predictions given by the MBCS theory have been compared with those offered by the BCS theory and the exact results, obtained at various numbers  $\Omega$  of levels, and particles,  $N$ . This systematic test has shown that the criterion of validity for the MBCS theory is fulfilled up to a temperature  $T_M$ . In the calculations using the reduced values of pairing-interaction parameter  $G$  to maintain the same pairing gap at zero temperature with increasing the particle number  $N$ , the value of  $T_M$  increases almost linearly with  $\Omega = N$  from around 0.6 MeV (higher than  $T_c$ ) at  $\Omega = N = 6$  up to around 24 MeV at  $\Omega = N = 100$ . For low  $N$ , it is demonstrated that enlarging the configuration space by adding one more valence level, *i.e.*  $\Omega = N + 1$ , restores the symmetry in the line shape of the quasiparticle-number fluctuation  $\sqrt{\delta\mathcal{N}_k^2}$ . As a result, the region of applicability of the MBCS theory can be extended up to  $T \sim 4\text{--}5$  MeV, even for  $N = 14$ . Hence, the conclusion, previously drawn from the application of the MBCS theory to realistic nuclei, is reconfirmed that the pairing gap does not collapse at  $T_c$  within the MBCS theory, but decreases monotonously with increasing the temperature.

The isovector giant dipole resonance (GDR) in nuclei is the collective vibration of protons against neutrons, which has been studied for more than eight decades. Except for very light nuclei, the absorption cross section of the GDR, as a function of  $\gamma$ -ray energy ( $E_\gamma$ ), is described by a single (for spherical nuclei) or a multi-component (for deformed nuclei) Lorentzian function

$$\sigma(E_\gamma) = \sum_i \frac{\sigma_i E_\gamma^2 \Gamma_i^2}{[(E_\gamma^2 - E_i^2)^2 + E_\gamma^2 \Gamma_i^2]}, \quad (108)$$

where  $E_i$ ,  $\Gamma_i$  and  $\sigma_i$  are, respectively, the resonance energy, width and the peak cross section of the  $i$ th component. The widths of GDR components represent the damping of the collective motion.

In the microscopic description of the GDR built on ground state, the resonance consists of many one particle-one hole ( $1p-1h$ ) coherent excitations across the Fermi surface. Its width  $\Gamma_Q$  (around 4–5 MeV in medium and heavy nuclei) occurs because of the quantal effects and consists of three parts [169] as

$$\Gamma_Q = \Gamma^{\text{LD}} + \Gamma^\downarrow + \Gamma^\uparrow. \quad (109)$$

The Landau width  $\Gamma^{\text{LD}}$  is the variance  $\sigma = \sqrt{\langle E^2 \rangle - \langle E \rangle^2}$  of the energy distribution of  $1p-1h$  states forming the giant resonance. The spreading width  $\Gamma^\downarrow$  is caused by the coupling of these states to  $2p-2h$  states and the subsequent progressive coupling to the complex  $np-nh$  states with  $n > 2$ . The escape width  $\Gamma^\uparrow$  arises from the coupling to the continuum causing the direct particle decay to hole states of the residual nucleus. In medium and heavy nuclei, the major contribution to  $\Gamma_Q$  is given by  $\Gamma^\downarrow$ , whereas in light nuclei, both  $\Gamma^\uparrow$  and  $\Gamma^{\text{LD}}$  are also important.

In highly excited nuclei (at finite temperature  $T$  and angular momentum  $J$ ), thermal effects also contribute in the total GDR width. Extensive experimental and theoretical works on the giant dipole resonance in excited nuclei in the last several decades have shown a reasonable stability of the GDR centroid energy and an increase in the GDR width with temperature ( $T \sim 1-3$  MeV) and angular momentum  $J$ . Some experiments have indicated the saturation of GDR width at high temperature.

The phonon damping model (PDM), proposed in [160, 161], is one of few theoretical models, which successfully describe the damping of the GDR including the pairing effect at finite temperature. Within the PDM, the GDR width is caused by the coupling of the structureless GDR phonon to non-collective  $ph$ ,  $pp$  and  $hh$  configurations. In open-shell nuclei, its Hamiltonian in the quasiparticle representation consists of three terms, describing the quasiparticle mean field, the phonon field and the interaction between them. The resulting GDR width consists of the quantal  $\Gamma_Q$  and thermal  $\Gamma_T$  widths in the forms [162]

$$\Gamma_Q = 2\pi \sum_{ph} [F_{ph}^{(1)}]^2 \times [u_{ph}^{(+)}]^2 (1 - n_p - n_h) \delta(E_D - E_p - E_h), \quad (110)$$

$$\Gamma_T = 2\pi \sum_{s>s'} [F_{ss'}^{(1)}]^2 \times [v_{ss'}^{(-)}]^2 (n_{s'} - n_s) \delta(E_D - E_s + E_{s'}), \quad (111)$$

with  $(ss') = pp'$  and  $hh'$ , the quasiparticle occupation numbers  $n_k$  and quasiparticle energies  $E_k$ , whereas  $u_{ph}^{(+)}$  and  $v_{ss'}^{(-)}$  are given in (104). The selection of the model's parameters  $F_{ph} = F_1$  and  $F_{ss'} = F_2$  is discussed in details in [162].

The increase in the total width at low temperature is compensated by the temperature dependence of the thermal pairing. Given the thermal fluctuations in finite nuclei, the pairing gap does not collapse at the critical temperature of the superfluid-normal phase transition but monotonically decreases with increasing the temperature as has been discussed in sections 2 and 4, turning the smooth Fermi surface due to pairing at zero temperature to the step-function distribution, thus, reducing the effect of coupling to  $pp$  and  $hh$  configurations. Depending on the pairing force, this compensation at low temperature leads to the insensitivity of the GDR width to temperature or even its decrease at  $T \leq 1$  MeV. At  $T > 1$  MeV, the effect of thermal pairing becomes small and the GDR width starts to increase because of the increase in  $\Gamma_T$  [162].

The calculations of the GDR widths have been carried out by using the modified BCS and the exact pairing gaps at finite temperature, with the corresponding quasiparticle energies, and Bogoliubov's coefficients  $u_k$  and  $v_k$ . The proton and neutron single-particle energies are obtained from the axially deformed Woods-Saxon potentials. The results obtained for Sn isotopes and  $^{201}\text{Tl}$ , shown in figure 55, demonstrate how the inclusion of thermal pairing reduces the GDR width at  $T < 1.5$  MeV, significantly improving the agreement with the experimental data.

The experimental and theoretical cross-sections obtained for the GDR in  $^{120}\text{Sn}$  at the initial temperatures of the cascade decay  $T = 1.24$ , and 1.54 MeV are shown in figure 56. This is the low temperature region, at which discrepancies are most pronounced between theory and experiment. From this figure, it is seen that thermal pairing clearly offers a better fit to the experimental line shape of the GDR at low temperature.

**6.1.3. Effect of pairing fluctuation on width of giant dipole resonance within thermal shape fluctuation model.** The thermal shape fluctuation model (TSFM) has been widely used in the interpretation of experimental data on the GDR width. The TSFM explains the observed increase in the GDR width as due to the increase of nuclear deformation with angular momentum  $J$  and the increase of shape fluctuation with temperature  $T$ . A larger deformation implies a wider splitting of the GDR energies. The Coriolis effect at high rotational frequencies produces further splitting. The observed GDR width, which is an ensemble average over those for various shapes, thus increases with temperature and/or angular momentum.

However, the TSFM in its original version without pairing failed to describe the GDR width in open shell nuclei at low temperature ( $T < 1.5$  MeV). Recently, the TSFM was extended to include the fluctuations in the pairing field [44, 168]. The nuclear shapes were related to the GDR observables using a model Hamiltonian, which describes the motion of nucleons

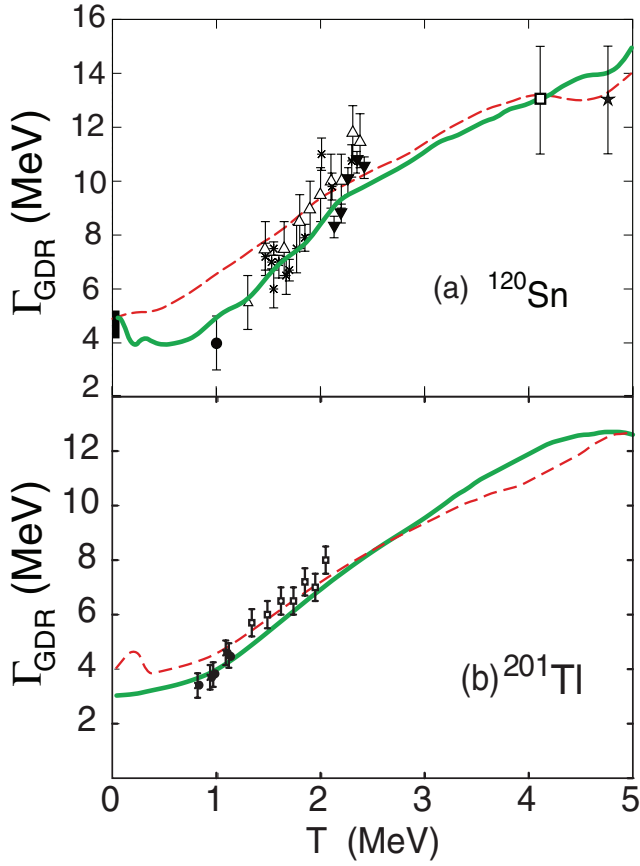


**Figure 55.** GDR widths in (a) Sn isotopes and (b)  $^{201}\text{Tl}$  and predictions of PDM including modified BCS pairing (a) and exact pairing (b). The (green) solid and (red) dashed lines are the PDM calculations with and without pairing, respectively. Data points in (a) and (b) are from [163–166] and [167], respectively. Adapted with permission from [41, 162], Copyright (2003 and 2012) by the American Physical Society.

within an anisotropic harmonic oscillator potential with the residual separable dipole–dipole and monopole pairing interactions, as  $H = H_{\text{osc}} + \eta D^\dagger D + \chi P^\dagger P$ , where  $H_{\text{osc}}$  stands for the anisotropic harmonic oscillator hamiltonian with  $D$  and  $P$  being the dipole and pairing operators, respectively. The parameter  $\eta$  characterizes the isovector component of the neutron and proton average field and  $\chi$  denotes the strength of the pairing interaction.

The averaged cross section of the GDR was calculated using (108) with  $\Gamma_i = \Gamma_0(E_i/E_0)^\delta$ , where  $\Gamma_0$  is the intrinsic width,  $\delta \sim 1.9$ ,  $E_i = E_0 \exp[-\sqrt{5/(4\pi)}\beta_i \cos(\gamma_i - 2\pi i/3)]$ , and

$$\sigma(\omega) = \frac{\int_{\beta} \int_{\gamma} \int_{\Delta_p} \int_{\Delta_N} \mathcal{D}[\alpha] \exp[-F_{\text{TOT}}(T; \beta, \gamma, \Delta_p, \Delta_N)/T] \sigma(\omega, \beta, \gamma, \Delta_p, \Delta_N)}{\int_{\beta} \int_{\gamma} \int_{\Delta_p} \int_{\Delta_N} \mathcal{D}[\alpha] \exp[-F_{\text{TOT}}(T; \beta, \gamma, \Delta_p, \Delta_N)/T]} \quad (112)$$

with a volume element given by  $\mathcal{D}[\alpha] = \beta^4 |\sin 3\gamma| d\beta d\gamma d\Delta_p d\Delta_N$ . The total free energy ( $F_{\text{TOT}}$ ) at a fixed deformation was calculated using the finite temperature Nilsson–Strutinsky method as  $F_{\text{TOT}} = E_{\text{LDM}} + \sum_{\tau=\pi,\nu} \delta F_{\tau}$ , where the liquid-drop energy  $E_{\text{LDM}}$  was obtained by summing up the Coulomb and surface energies corresponding to a triaxially deformed shape with deformation parameters  $\beta$  and  $\gamma$ . The shell correction  $\delta F_{\tau} \equiv F_{\tau} - \tilde{F}_{\tau}$  was calculated by using the

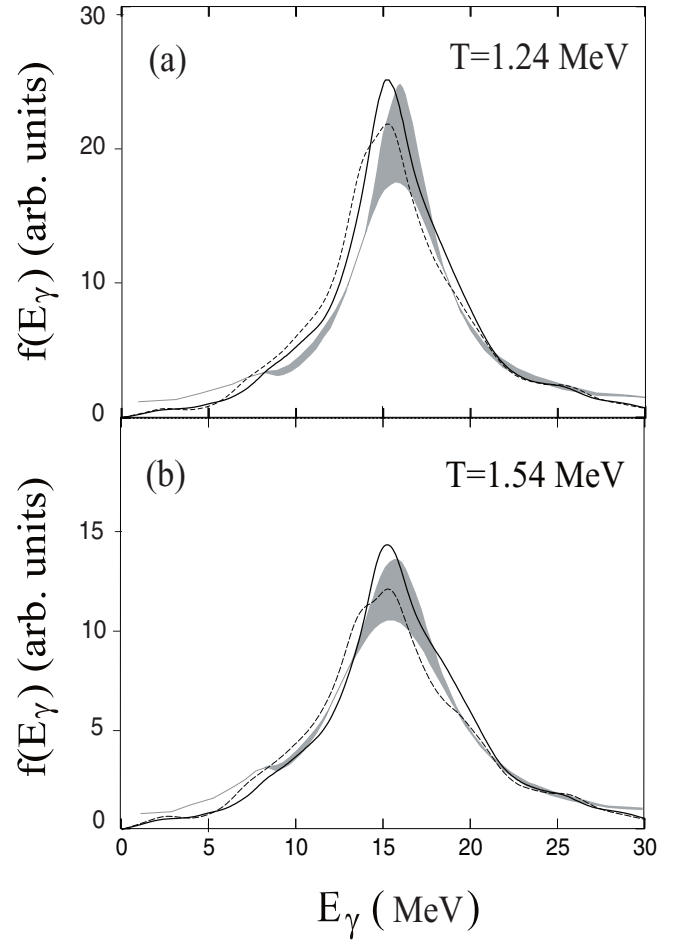


**Figure 56.** Experimental (shaded areas) from figure 2 of [170] in comparison with theoretical divided spectra obtained within the PDM without pairing (dashed lines) and including pairing (thick solid lines) for the GDR in  $^{120}\text{Sn}$ . Adapted with permission from [162], Copyright (2003) by the American Physical Society.

proton ( $\pi$ ) and neutron ( $\nu$ ) single-particle energies obtained in the triaxial Nilsson potentials. With the pairing fluctuations, the corresponding free energy was determined in the grandcanonical ensemble as  $F = \langle H \rangle - \lambda N - TS = \sum_k (\epsilon_k - \lambda - E_k) - 2T \sum_k \ln [1 + \exp(-E_k/T)] + \Delta^2/G$ , where  $H$  is the nuclear Hamiltonian (1),  $\lambda$  is the chemical potential,  $N$  is the particle number,  $S$  is the entropy, and  $\epsilon_k$  are the single-particle energies obtained by diagonalizing  $H$  within a harmonic oscillator basis comprising the first 12 major shells. The quasiparticle energies  $E_k$  and the pairing gap  $\Delta$  were obtained from the BCS theory by assuming a constant pairing strength  $G_{\pi,\nu} = [19.2 \pm 7.4(N - Z)]/A^2$ . The smoothed free energy was found by Strutinsky’s method. The total entropy is given as  $S = \sum_k s_k = -2 \sum_k [n_k \ln n_k + (1 - n_k) \ln(1 - n_k)]$ , with the quasiparticle occupation numbers  $n_k$ .

The average pairing gaps  $\langle \Delta \rangle$ , average quadrupole deformation parameters  $\beta$  and GDR widths  $\Gamma$  obtained within this formalism for  $^{120}\text{Sn}$  are shown in figure 57. The results clearly show that, for open shell nuclei, the inclusion of pairing fluctuations in the TSFM significantly improves comparison with experiment at low temperature.

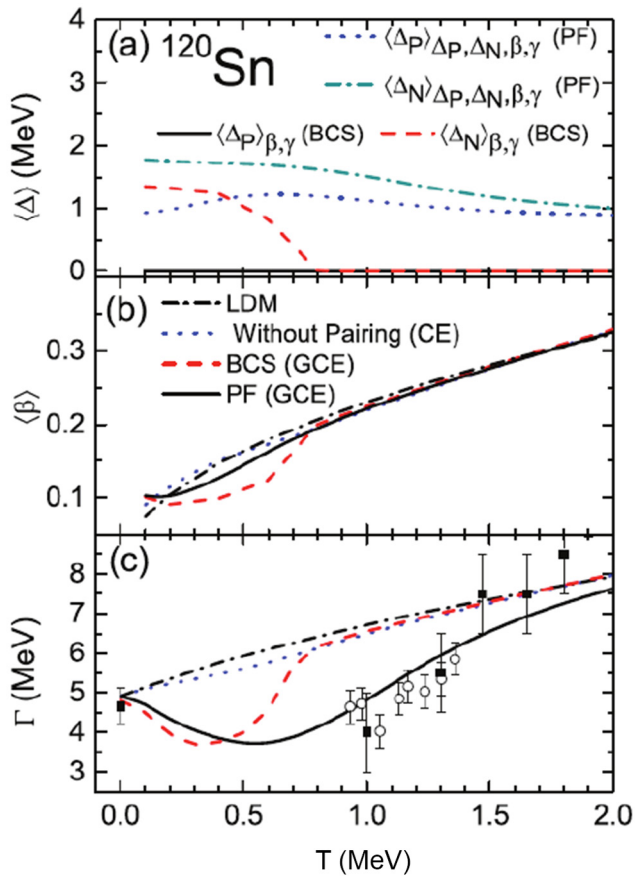


**Figure 57.** (a) Average pairing gap, (b) average quadrupole deformation parameter, and (c) GDR width in  $^{120}\text{Sn}$ , as a function of temperature. Calculations without pairing are done within the canonical ensemble, and those with BCS pairing (BCS) and pairing fluctuations (PF) are carried out within grand canonical ensemble. Predictions by the liquid drop model (LDM) are also presented. Solid squares are the experimental GDR widths in  $^{120}\text{Sn}$  taken from [164, 171]. Open circles are data for the GDR widths in  $^{119}\text{Sb}$  [172]. Adapted with permission from [44], Copyright (2015) by the American Physical Society.

## 6.2. Effect of exact thermal pairing on nuclear level density and radiative strength function

As has been pointed out in the Introduction, a unified microscopic approach [45] has been proposed very recently in order to simultaneously describe two key quantities of hot nuclei, namely nuclear level density and radiative strength function of the  $\gamma$ -ray emissions. These quantities are important for the description of low-energy nuclear reactions as well as nucleosynthesis in stars. The derivation of this approach and its application to some realistic nuclei are reviewed in this section.

For the level density, the approach is derived based on the exact solution of the pairing problem introduced in section 4.3 for a given number of single-particle levels around the Fermi surface (truncated space) in combination with the independent-particle model for the levels outside the truncated space as (77). In the latter, the partition function  $Z'_{\nu, sr}$  is replaced with the exact canonical ensemble partition function  $Z_{\text{ex}}$  (78), which is obtained by directly diagonalizing the

pairing Hamiltonian for 12 doubly degenerate single-particle levels with 6 levels above and 6 levels below the Fermi surface. Knowing the partition function, one can easily calculate all the thermodynamic quantities following (73) as well as the total density of state  $\omega(E^*) = e^S / (T\sqrt{2\pi C})$ . The total level density  $\rho(E^*)$  can be obtained from the state density  $\omega(E^*)$  by considering the contribution of the nuclear spin distribution as  $\rho(E^*) = \omega(E^*) / (\sigma\sqrt{2\pi})$ , where the spin cut-off parameter  $\sigma$  in axially deformed nuclei is often divided into two components, the parallel component  $\sigma_{\parallel} = \mathcal{I}_{\parallel} T / \hbar^2$  and the perpendicular one  $\sigma_{\perp} = \mathcal{I}_{\perp} T / \hbar^2$ , which are associated with the nuclear moments of inertia parallel ( $\mathcal{I}_{\parallel}$ ) and perpendicular ( $\mathcal{I}_{\perp}$ ) to the symmetry axis, respectively. Here for simplicity, we use the empirical formula for  $\sigma_{\perp}$ , which is obtained from the limit of rigid body with the same density distribution as of the nucleus, namely  $\sigma_{\perp}^2 \approx 0.015A^{5/3}T$  [173], whereas  $\sigma_{\parallel}$  can be expressed in terms of  $\sigma_{\perp}$  and quadrupole deformation parameter  $\beta_2$  as  $\sigma_{\parallel} = \sigma_{\perp} \sqrt{(3 - 2\beta_2)/(3 + \beta_2)}$  [174, 175]. Moreover, the collective vibrational and rotational excitations, which are known to enhance the level density but are not included in the pairing Hamiltonian, are also taken into account via their corresponding  $k_{\text{vib}}$  and  $k_{\text{rot}}$  factors. The latter, which are defined as the ‘correct’ level density including all degrees of freedom and the level density without the contribution from the collective vibration and rotation [174–178], can be calculated based on the empirical formulas as  $k_{\text{vib}} = \exp[0.0555A^{2/3}T^{4/3}]$  [178] and  $k_{\text{rot}} = (\sigma_{\perp}^2 - 1)[1 + e^{(E^* - U_C)/D_C}]^{-1} + 1$ , where  $D_C$  and  $U_C$  are given as  $D_C = 1400\beta_2^2 A^{-2/3}$ ,  $U_C = 120\beta_2^2 A^{1/3}$  [174, 175]. The final level density, including the effects of vibrational and rotational enhancements, is given by [174, 175, 179]

$$\rho(E^*) = k_{\text{rot}} k_{\text{vib}} \frac{\omega(E^*)}{\sigma_{\parallel} \sqrt{2\pi}}. \quad (113)$$

As for the radiative strength function, the phonon damping model (PDM) [162], in which the pairing effect is taken from the exact canonical ensemble instead of the approximate pairing as presented in section 6.1.2, has been used [41, 42, 180]. Within the PDM, the radiative strength function  $f_{X\lambda}(E_{\gamma})$  for the electric ( $X = E$ ) or magnetic ( $X = M$ ) excitations with multipolarity  $\lambda$  is calculated as

$$f_{X\lambda}(E_{\gamma}) = \frac{1}{(2\lambda + 1)\pi\hbar^2 c^2} \times \frac{\Gamma_{X\lambda}(E_{\gamma}) \sigma(X\lambda) S_{X\lambda}(E_{\gamma})}{E_{\gamma}}, \quad (114)$$

where  $\sigma(X\lambda)$  is the cross section, whereas the temperature-dependent width  $\Gamma_{X\lambda}$  is the sum of the quantal width  $\Gamma_Q$  caused by coupling the collective excitations to the non-collective  $ph$  configurations at zero and finite temperature and thermal width  $\Gamma_T$  caused by coupling of giant resonances to the  $pp$  and  $hh$  configuration at finite temperature. The formulations of these widths are given in detail in (109)–(111) of section 6.1.2. The strength function  $S_{X\lambda}(E_{\gamma})$  within the PDM is calculated as

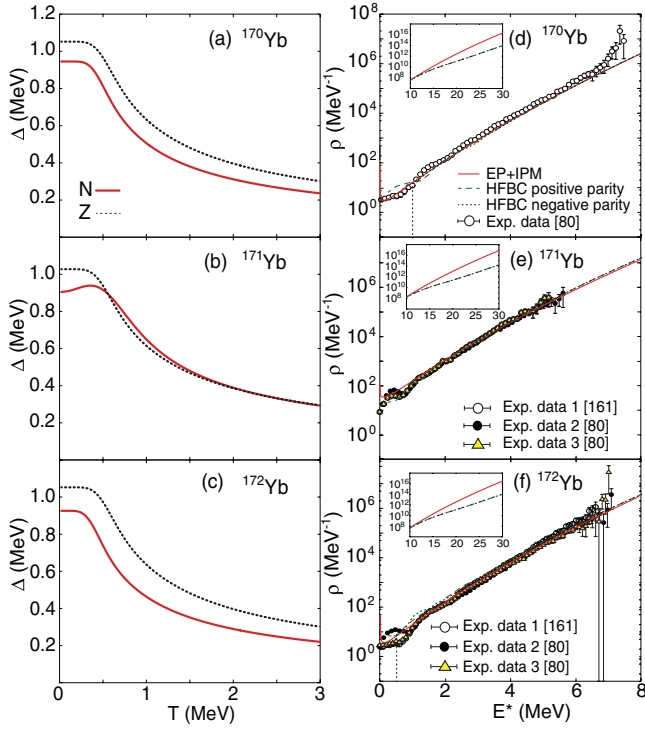


**Figure 58.** Neutron and proton pairing gaps  $\Delta$  ((a)–(c)) as functions of  $T$  and total level densities  $\rho$  ((d)–(f)) as functions of  $E^*$  obtained within the EP + IPM in comparison with predictions of HFBC calculations for the positive and negative parities and the experimental data for  $^{170,171,172}\text{Yb}$  nuclei. Adapted with permission from [45], Copyright (2017) by the American Physical Society.

$$S_{X\lambda}(E_\gamma) = \frac{1}{\pi} \frac{\gamma(E_\gamma)}{(E_\gamma - E_{X\lambda})^2 + \gamma(E_\gamma)^2}, \quad (115)$$

where the damping  $\gamma(E_{X\lambda})$  is calculated as the half of the width, namely  $\gamma(E_{X\lambda}) = \Gamma_{X\lambda}/2$ .

Shown in figure 58 are the exact neutron  $\Delta_N$  and proton  $\Delta_Z$  pairing gaps and total level densities  $\rho(E^*)$  obtained within the exact pairing plus independent particle model (EP + IPM) for  $^{170,171,172}\text{Yb}$  isotopes along with those obtained within the Hartree-Fock-Bogoliubov plus combinatorial model (HFBC) for positive and negative parities taken from RIPL-3 [181] versus the experimental data measured by the Oslo group [80, 182]. Within the EP + IPM, the single-particle spectra are taken from the deformed Woods–Saxon potential with the quadrupole deformation parameter  $\beta_2 = 0.295$  for  $^{170,171}\text{Yb}$  and 0.296 for  $^{172}\text{Yb}$  [142], whereas the values of pairing interaction parameter  $G$  for protons and neutrons are, as usual, adjusted so that the exact proton and neutron pairing gaps obtained at zero temperature fit the corresponding experimental values extracted from the odd–even mass formula. Figure 58 shows that the exact gaps (a)–(c) decrease with increasing the temperature and remain finite even at the temperature as high as 3 MeV, which is well above its critical value  $T_c \sim 0.57\Delta(T=0)$  where the conventional BCS gaps collapse. For an odd  $^{171}\text{Yb}$  nucleus, a slight increase in the exact neutron gap is seen at low  $T < 0.5$  MeV, which is caused by the blocking effect from the odd neutron as has been discussed in section 3.3. Because of these nonzero pairing gaps,

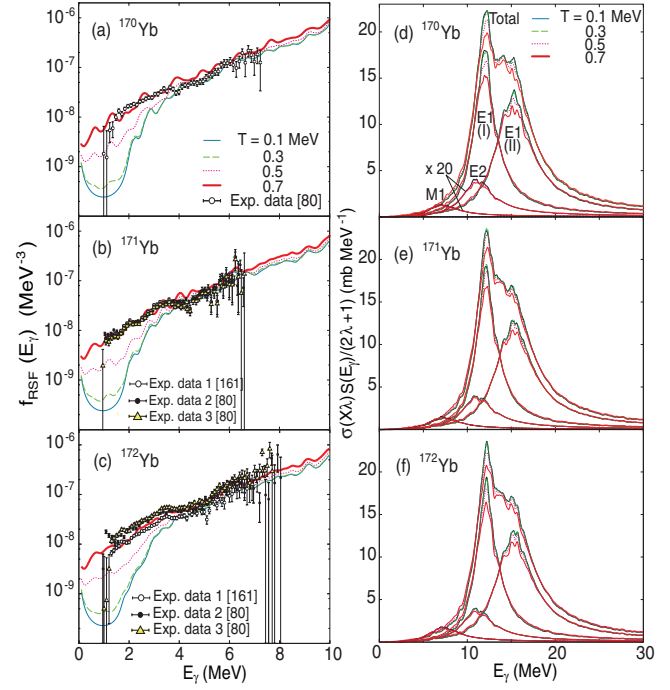


**Figure 59.** Radiative strength functions ((a)–(c)) obtained within the PDM plus exact pairing in comparison with experimental data for  $^{170,171,172}\text{Yb}$  nuclei, and the corresponding total strength functions ((d)–(f)) together with their components for  $E1$ ,  $E2$ , and  $M1$  excitations as functions of  $E_\gamma$  at different temperatures. Adapted with permission from [45], Copyright (2017) by the American Physical Society.

the total level densities obtained within the EP + IPM (solid lines in figures 58 (d)–(f)) agree very well with the experimental data. It is also shown that the EP + IPM level densities almost coincide with those obtained within the global microscopic HFBC calculations for both negative and positive parities [183]. However, to have a good description of nuclear level density, the latter have to be normalized to fit the experimental level densities at the low and neutron separation energies (see e.g. equation (9) of [184]). Moreover, it is known that the HFBC was derived based on the partition function of the incoherent  $ph$  states built on top of the HFB single-particle spectra, its prediction of level density in the high-energy region, where the contribution of higher coupling configurations such as  $pp$ ,  $hh$ ,  $2p2h$ ,  $3p3h$  etc is important, is certainly not reliable. At the same time, the EP + IPM is derived from the exact canonical ensemble partition function built based on the direct diagonalization of the pairing Hamiltonian, which consists of all the possible couplings between the  $pp$ ,  $hh$ , and  $ph$  states. By combining this exact partition function with the IPM, it is obvious that the EP + IPM is capable of describing the total level density up to very high excitation energy. This feature can be seen clearly in the insets of figures 58(d)–(f) showing that the EP + IPM level densities are significant higher than those obtained within the HFBC in the region of  $10 \leq E^* \leq 30$  MeV.

In figure 59, we plot the total radiative strength functions  $f(E_\gamma)$  and strength functions  $S_{X\lambda}(E_\gamma)$  (115) obtained within the PDM for the magnetic dipole  $M1$ , electric dipole  $E1$ , and

electric quadrupole  $E2$  resonances. The total radiative strength function is calculated as the sum of  $f_{X\lambda}(E_\gamma)$  (114), namely  $f_{\text{RSF}} = f_{M1} + f_{E1(I)} + f_{E1(II)} + f_{E2}$ , where  $E1(I)$  and  $E1(II)$  correspond to the two components of the GDR in deformed nuclei determined from the photoabsorption experiments [80]. Within the PDM calculation, all the resonance energies  $E_{X,\lambda}$ , resonance widths  $\Gamma_{X,\lambda}$ , and cross section  $\sigma(X\lambda)$  are fixed at  $T = 0$ . The values of these parameters for  $^{170,171,172}\text{Yb}$  are taken e.g. from table I of [80]. It is seen from figures 59(d)–(f) that the strength functions of the GDR, which correspond to the  $E1(I)$  and  $E1(II)$  resonances, give the largest contribution to the total strength. Their corresponding widths are found to be nearly constant at  $T \leq 0.4$  MeV and increase at  $T > 0.4$  MeV. Consequently, there is a significant increase of the total radiative strength function at low  $E_\gamma < 4$  MeV as seen in figures 59(a)–(c). Interestingly, one could see that the total radiative strength function obtained within the PDM at  $T = 0.7$  MeV agrees well with the experimental data for all three isotopes. This value of  $T$  is higher than that (around 0.4 MeV) obtained within the phenomenological fitting model of Kadenskij–Markushev–Furman (KMF) [185] reported in [80], indicating that the temperature-dependent width is indeed important for the description of total radiative strength function. This finding is important as it invalidates the Brink–Axel hypothesis [186, 187], which assumes that the strength function of collective excitations built on excited states should be always energy-independent. It is also very interesting to see from figures 59(b) and (c) that the two-component pygmy dipole resonance (PDR) seen in the total radiative strength functions of  $^{171}\text{Yb}$  and  $^{172}\text{Yb}$  in the region of  $2.1 < E_\gamma < 3.5$  MeV as indicated via the fitting of the KMF model in [80] can be described very well within the PDM calculation without the need of adding a PDR strength function to the total radiative strength function as often being done in the analysis of the KMF model [80, 182]. It is worth noting here that this two-component PDR has not been reproduced in any microscopic models so far. Within the PDM, it has been reported in [180] that the exact pairing is indeed important for the description of the  $E1$  strength function in the PDR region of  $E_\gamma < 5$  MeV. As the result, the enhancement of experimental radiative strength function at low  $E_\gamma$  associated with the PDR is well explained, for the first time, by the effect of exact thermal pairing within the present PDM calculations.

Very recently, by using the EP + IPM, we have provided a good and consistent description of total level densities of  $^{60-62}\text{Ni}$  isotopes in both low-energy  $E^* \leq 5$  MeV and high-energy (up to 20 MeV) regions [188]. Moreover, it has been found in [188] that the increase in the nuclear temperature, which is calculated from the derivative of the logarithm of the EP+IPM level densities, is relatively slow up to the excitation energy  $E^* = E_f^*$ . Therefore, at  $0 < E^* \leq E_f^*$  the level density can be well described by the constant-temperature model. The values of  $E_f^*$  are found to be 10 MeV for  $^{170-172}\text{Yb}$  and 20 MeV for  $^{60-62}\text{Ni}$ . These values are much higher than the particle separation threshold. Within this energy interval, the constant temperature is found to be around 0.5 MeV for  $^{170-172}\text{Yb}$ , whereas, for  $^{60-62}\text{Ni}$ , it can be any value between

1.3 and 1.5 MeV (see figure 8 in [188]), in excellent agreement with the recent experimental findings [181, 189]. It is also shown in [188] that pairing plays an important role in maintaining this constant temperature at low excitation energy (see figure 6 in [188]). At the same time, the EP + IPM has also been extended to successfully describe the angular-momentum dependent level densities of a hot rotating  $^{96}\text{Tc}$  nucleus, whose data are extracted from the evaporated neutron spectra in the  $^4\text{He} + ^{93}\text{Nb}$  reaction in the energy range of  $E^* \sim 5-15$  MeV [190]. Consequently, the EP + IPM level densities are used to study the thermodynamic properties of this hot rotating  $^{96}\text{Tc}$  nucleus (see e.g. figure 9 of [190]). The EP + IPM results for the total level densities of  $^{170-172}\text{Yb}$  and  $^{60-62}\text{Ni}$  together with those for the angular-momentum dependent level densities of a hot rotating  $^{96}\text{Tc}$  nucleus clearly show that the EP + IPM method, which conserves exactly the particle number at both zero and finite temperatures, is indeed a microscopic method capable of providing a reliable description of both total and angular-momentum-dependent level density data.

The merits of the approach reviewed in this section are its microscopic nature and the absence of fitting parameters at different excitation and  $\gamma$ -ray energies. In addition, its computational time is significantly shorter as compared with other approaches like SMMC or HFBC, namely one calculation takes less than 5 minutes even for a heavy nucleus.

## 7. Summary and outlook

The present review summarizes the recent progress in the study of pairing properties in excited nuclei and their analogy to those appeared in other finite systems including superconductors, metallic nano sized clusters/grains, and solid-state materials such as ferromagnets.

The first part of the review discusses the treatment of pairing within a uniform model based on the BCS Hamiltonian within the grand canonical ensemble. The phase diagram boundaries of the paired region with associated phase transitions are examined in several cases, namely (i) fixed total angular momentum: second-order phase transition; (ii) fixed quasiparticle number: first- and second-order phase transitions; and (iii) fixed total energy: first-order phase transition. This pairing treatment is extended to the realistic shell model single-particle spectra to confirm the robustness of the effects discussed above in realistic nuclei.

The second part of the review focuses on the grand-canonical treatment of pairing within the Hartree-Fock-Bogoliubov theory and finite-temperature pairing reentrance phenomenon in superconducting ultrasmall metallic grains as well as even-even and odd nuclei.

The third part of the review presents the results obtained from the treatment of nuclear pairing within the canonical and microcanonical ensembles, from which the effect caused by the finite size of the systems is highlighted. Different approaches to canonical and microcanonical ensembles including particle-number projection, particle-number projection plus static path approximation, solutions of BCS with Lipkin–Nogami particle-number projection incorporating

the self-consistent quasiparticle random-phase approximation and embedded into the canonical ensemble and microcanonical ensemble, shell model Monte Carlo method at finite temperature, and exact solutions of the pairing problems, which are embedded into the canonical and microcanonical ensembles, are introduced. The results obtained are compared with those predicted by the doubly-folded equidistant multilevel pairing model (Richardson model) as well as the experimental data of some realistic nuclei such as  $^{94,98}\text{Mo}$ ,  $^{162}\text{Dy}$ , and  $^{172}\text{Yb}$ .

In the fourth part of the review, the first experimental evidence of the pairing reentrance phenomenon in a warm rotating  $^{104}\text{Pd}$  nucleus, which was observed via the local enhancement of nuclear level density at low temperature and high angular momentum extracted from the reaction  $^{12}\text{C} + ^{93}\text{Nb}$  at the incident energy of 40–50 MeV, is analyzed and discussed within the framework of a BCS theory, which includes the quasiparticle-number fluctuations (BCS1) at finite temperature and angular momentum. The similar behavior of pairing reentrance observed in the condensed-matter counterpart such as metallic compound of  $\text{Eu}_{0.75}\text{Sn}_{0.25}\text{Mo}_6\text{S}_{7.2}\text{Se}_{0.8}$  and heavy-fermion cubic system of  $\text{CePb}_3$ , quasi-2D organic conductor  $\kappa\text{-(BETS)}_2\text{FeCl}_4$ , and ferromagnetic superconductor of  $\text{URhGe}$  under the strong magnetic field is also summarized in this part.

The role of approximate and exact thermal pairings in the properties of excited nuclei such as giant dipole resonance, total nuclear level density, and radiative strength function of the  $\gamma$ -rays emission is discussed in the last part. In particular, including the non-vanishing pairing gap allowed resolving the issue with the temperature-independent giant dipole resonance width at low temperature ( $T \leq 1$  MeV) in open-shell nuclei. Exact pairing is also crucial for the simultaneous description of the total level density and radiative strength function of some rare earth nuclei.

It has been found that, by applying the BCS theory at finite temperature and angular momentum to the uniform nuclear model, for which the analytic solutions of the BCS equation can be obtained, one is able to study the appearance of the first-order and second-order phase transitions in finite nuclear systems when either the total angular momentum or the number of quasiparticles or the total energy of the system is fixed. However, it has also been pointed out that these shape phase transitions are simply an artifact caused the application of the BCS theory to finite atomic nuclei, neglecting all the thermal fluctuations. In fact, in finite systems, where thermal fluctuations are rather strong, all the phase transitions are smoothed out, leading to different behaviors of nuclear thermodynamic quantities. For example, the modified BCS and BCS1 theories at finite temperature have shown that the fluctuations of the quasiparticle number are one of the microscopic origins caused the nonvanishing nuclear pairing gaps at finite temperature, which consequently result in the smoothing of the superfluid-normal (second-order) phase transition. This feature is also confirmed by the calculations within the shell-model Monte-Carlo method as well as exact thermal

pairing. This finding is important in the sense that thermal fluctuations should always be considered whenever the statistical methods are applied to finite systems.

The analysis of pairing reentrance within the BCS1 at finite temperature and angular momentum demonstrates that the effect caused by thermal fluctuations in terms of the quasiparticle-number ones seems to be quite significant. However, to have a more precise description of the experimental data, this theory should be extended to include higher components of the nuclear Hamiltonian such as dipole, quadrupole, and octupole excitations. On the other hand, more experimental measurements and analyses need to be performed in order to reaffirm the presence of the pairing reentrance in atomic nuclei.

The use of exact thermal pairing in combination with the independent-particle model as well as the PDM has shown its promising efficiency in providing a reliable prediction of nuclear level density and radiative strength function. This approach should therefore be extended to other nuclei in the entire mass region.

## Acknowledgments

Some parts of numerical calculations for excited nuclei reported in sections 4–6 were carried out on the Hokusai GreatWave Computer System of RIKEN. Thanks are due to Le Tan Phuc (Institute of Fundamental and Applied Sciences, Duy Tan University) for his assistance in arranging the text and drawing a number of figures. This work is funded by the Vietnam Government under the Program of Development in Physics toward 2020 (Grant No. DTDLCN.02/19) and the National Foundation for Science and Technology Development (NAFOSTED) of Vietnam (Grant No. 103.04-2017.69).

## ORCID iDs

N Quang Hung  <https://orcid.org/0000-0002-9739-301X>

## References

- [1] Bardeen J, Cooper L and Schrieffer J R 1957 *Phys. Rev.* **108** 1175–204
- [2] Atkins K R 1959 *Liquid Helium* (London: Cambridge University Press)
- [3] Baym G, Pethick C J and Pikes D 1969 *Nature* **224** 674–5
- [4] Hoffberg M, Glassgold A E, Richardson R W and Ruderman M 1970 *Phys. Rev. Lett.* **24** 775–7
- [5] Dean D J and Hjorth-Jensen M 2003 *Rev. Mod. Phys.* **75** 607–56
- [6] Suzuki M 1969 *Prog. Theor. Phys.* **41** 1438–49
- [7] Kawabata C and Suzuki M 1970 *J. Phys. Soc. Japan* **28** 16–28
- [8] Braun F and Delft J V 1998 *Phys. Rev. Lett.* **81** 4712–5
- [9] Braun F and Delft J V 1999 *Phys. Rev. B* **59** 9527–44
- [10] Borrmann P and Harting J 2001 *Phys. Rev. Lett.* **86** 3120–3
- [11] Harting J, Mulken O and Borrmann P 2000 *Phys. Rev. B* **62** 10207–11
- [12] Delft J V 2001 *Ann. Phys., Lpz* **10** 219–76

- [13] Delft J V and Ralph D C 2001 *Phys. Rep.* **345** 61–173
- [14] Bohr A, Mottelson B R and Pines D 1958 *Phys. Rev.* **110** 936–8
- [15] Bohr A and Mottelson B R 1969 *Nuclear Structure* vol 1 (New York: Benjamin)
- [16] Belyaev S T 1959 *Mat.-Fys. Medd. Dan. Vidensk. Selsk.* **31** <https://scholar.google.com/scholar?q=Belyaev%20S.%20T.%3A%20K.%20Dan.%20Vidensk%20Selsk.%20Mat.-Fys.%20Medd.31%20%281959%29%2C%20No.%2011>
- [17] Belyaev S T 1961 *Nucl. Phys.* **24** 322–5
- [18] Soloviev V G 1958/1959 *Nucl. Phys.* **9** 655–64
- [19] Soloviev V G 1971 *Theory of Complex Nuclei* (Moscow: Nauka)
- [20] Mottelson B R and Valatin J G 1960 *Phys. Rev. Lett.* **5** 511–2
- [21] Ericson T 1960 *Adv. Phys.* **9** 425–511
- [22] Richardson R W and Sherman N 1964 *Nucl. Phys.* **52** 253–68
- [23] Kammuri T 1964 *Prog. Theor. Phys.* **31** 595–608
- [24] Moretto L G 1972 *Phys. Lett.* **40** 1–4
- [25] Moretto L G 1971 *Phys. Lett. B* **35** 379–82
- [26] Moretto L G 1972 *Nucl. Phys. A* **185** 145–65
- [27] Ring P, Robledo L M, Egidio J L and Faber M 1984 *Nucl. Phys. A* **419** 261–94
- [28] Dang N D 1985 *J. Phys. G: Nucl. Phys.* **11** L125–33
- [29] Dang N D 1990 *Z. Phys. A* **335** 253–64
- [30] Balian R, Flocard H and Vénéroni M 1999 *Phys. Rep.* **317** 251–358
- [31] Lévy F, Sheikin I, Grenier B and Huxley A D 2005 *Science* **309** 1343–6
- [32] Ding H, Yokoya T, Campuzano J C, Takahashi T, Randeria M, Norman M R, Mochiku T, Kadowaki K and Giapintzakis J 1996 *Nature* **382** 51–4
- [33] Goodman A L 1981 *Nucl. Phys. A* **352** 30–44
- [34] Goodman A L 1984 *Phys. Rev. C* **29** 1887–96
- [35] Zelevinsky V, Brown B A, Frazier N and Horoi M 1996 *Phys. Rep.* **276** 85–176
- [36] Koonin S E, Dean D J and Langanke K 1997 *Phys. Rep.* **278** 1–247
- [37] Dang N D and Arima A 2003 *Phys. Rev. C* **68** 014318
- [38] Dang N D and Hung N Q 2008 *Phys. Rev. C* **77** 064315
- [39] Kaneko K and Hasegawa M 2005 *Phys. Rev. C* **72** 024307
- [40] Hung N Q and Dang N D 2009 *Phys. Rev. C* **79** 054328
- [41] Dang N D and Hung N Q 2012 *Phys. Rev. C* **86** 044333
- [42] Dey B *et al* 2014 *Phys. Lett. B* **731** 92–6
- [43] Chakrabarty D, Dang N D and Datar V M 2016 *Eur. Phys. J. A* **52** 143
- [44] Kumar A K R, Arumugam P and Dang N D 2015 *Phys. Rev. C* **91** 044305
- [45] Hung N Q, Dang N D and Huong L T Q 2017 *Phys. Rev. Lett.* **118** 022502
- [46] Frauendorf S, Kuzmenko N K, Mikhajlov V M and Sheikh J A 2003 *Phys. Rev. B* **68** 024518
- [47] Sheikh J A, Palit R and Frauendorf S 2005 *Phys. Rev. C* **72** 041301
- [48] Hung N Q and Dang N D 2008 *Phys. Rev. C* **78** 064315
- [49] Schiller A *et al* 2001 *Phys. At. Nucl.* **64** 1186–93
- [50] Kaneko K *et al* 2006 *Phys. Rev. C* **74** 024325
- [51] Algin E, Agvaanluvsan U, Guttormsen M, Larsen A C, Mitchell G E, Rekestad J, Schiller A, Siem S and Voinov A 2008 *Phys. Rev. C* **78** 054321
- [52] Dean D J, Langanke K, Nam H A and Nazarewicz W 2010 *Phys. Rev. Lett.* **105** 212504
- [53] Hung N Q and Dang N D 2011 *Phys. Rev. C* **84** 054324
- [54] Mitra A, Chakrabarty D R, Datar V M, Kumar S, Mirgule E T and Oza H H 2002 *Nucl. Phys. A* **707** 343–53
- [55] Mitra A, Chakrabarty D R, Data V M, Kumar S, Mirgule E T, Oza H H, Nanal V and Pillay R G 2006 *Nucl. Phys. A* **765** 277–93
- [56] Mitra A, Chakrabarty D R, Datar V M, Kumar S, Mirgule E T, Nanal V and Rout P C 2009 *J. Phys. G: Nucl. Part. Phys.* **36** 095103
- [57] Mitra A, Chakrabarty D R, Datar V M, Kumar S, Mirgule E T, Rout P C and Nanal V 2010 *EPJ Web Conf.* **2** 04004
- [58] Data V M, Mitra A and Chakrabarty D R 2012 *DAE Symp. Nucl. Phys.* 57 184–5
- [59] Hung N Q, Dang N D, Agrawal B K, Datar V M, Mitra A and Chakrabarty D R 2015 *J. Phys.: Conf. Ser.* **627** 012006
- [60] Hung N Q, Dang N D, Agrawal B K, Datar V M, Mitra A and Chakrabarty D R 2015 *Acta Phys. Pol. B* **8** 551–8
- [61] Bogoliubov N N 1958 *Sov. Phys.—JETP* **7** 41–6
- [62] Huizenga J R and Moretto L G 1972 *Annu. Rev. Nucl. Sci.* **22** 427–64
- [63] Sano M and Yamasaki S 1963 *Prog. Theor. Phys.* **29** 397–414
- [64] Bethe H 1936 *Phys. Rev.* **50** 332–41
- [65] Bethe H 1937 *Rev. Mod. Phys.* **9** 69–249
- [66] Moretto L G 1973 *Phys. Lett. B* **46** 20–2
- [67] Moretto L G 1974 *Nucl. Phys. A* **226** 9–30
- [68] Moretto L G 1973 *Nucl. Phys. A* **216** 1–28
- [69] Griffin J J 1966 *Phys. Rev. Lett.* **17** 478–81
- [70] Cline C K and Blann M 1971 *Nucl. Phys. A* **172** 225–59
- [71] Blann M and Mignerey A 1972 *Nucl. Phys. A* **186** 245–56
- [72] Cline C K 1972 *Nucl. Phys. A* **193** 417–37
- [73] Decowski P, Grochulski W, Marcinkowski A, Siwek K and Wilhelmi Z 1968 *Nucl. Phys. A* **110** 129–41
- [74] Moretto L G 1972 *Nucl. Phys. A* **182** 641–68
- [75] Moretto L G 1975 *Nucl. Phys. A* **243** 77–99
- [76] Gilbert A and Cameron A G W 1965 *Can. J. Phys.* **43** 1446–96
- [77] Melby E, Guttormsen M, Rekestad J, Schiller A, Siem S and Voinov A 2001 *Phys. Rev. C* **63** 044309
- [78] Siem S, Guttormsen M, Ingeberg K, Melby E, Rekestad J, Schiller A and Voinov A 2002 *Phys. Rev. C* **65** 044318
- [79] Guttormsen M, Bagheri A, Chankova R, Rekestad J, Siem S, Schiller A and Voinov A 2003 *Phys. Rev. C* **68** 064306
- [80] Agvaanluvsan U *et al* 2004 *Phys. Rev. C* **70** 054611
- [81] Nyhus H T, Siem S, Guttormsen M, Larsen A C, Burger A, Syed N U H, Toft H K, Tveten G M and Voinov A 2012 *Phys. Rev. C* **85** 014323
- [82] Guttormsen M, Hjorth-Jensen M, Melby E, Rekestad J, Schiller A and Siem S 2000 *Phys. Rev. C* **61** 067302
- [83] Guttormsen M *et al* 2014 *Phys. Rev. C* **89** 014302
- [84] Moretto L G, Larsen A C, Giacoppo F, Guttormsen M, Siem S and Voinov A V 2014 (arXiv:1406.2642v3)
- [85] Moretto L G, Larsen A C, Giacoppo F, Guttormsen M and Siem S 2015 *J. Phys.: Conf. Ser.* **580** 012048
- [86] Goodman A L 1986 *Phys. Rev. C* **34** 1942–9
- [87] Baranger M and Kumar K 1968 *Nucl. Phys. A* **110** 490–528
- [88] Kumar K and Baranger M 1968 *Nucl. Phys. A* **110** 529–54
- [89] Khan E, Giai N V and Grasso M 2004 *Nucl. Phys. A* **731** 311–6
- [90] Khan E, Giai N V and Sandulescu N 2007 *Nucl. Phys. A* **789** 94–102
- [91] Sandulescu N 2007 *Phys. Rev. C* **70** 025801
- [92] Li J J, Margueron J, Long W H and Giai N V 2015 *Phys. Rev. C* **92** 014302
- [93] Goodman A L 1981 *Nucl. Phys. A* **352** 45–59
- [94] Tanabe K, Sugawara-Tanabe K and Mang H J 1981 *Nucl. Phys. A* **357** 22–44
- [95] Sugawara-Tanabe K, Tanabe K and Mang H J 1981 *Nucl. Phys. A* **357** 45–60
- [96] Martin V and Egidio J L 1995 *Phys. Rev. C* **51** 3084–95
- [97] Magueron J and Khan E 2012 *Phys. Rev. C* **86** 065801
- [98] Belabbas M, Li J J and Margueron J 2017 *Phys. Rev. C* **96** 024304
- [99] Dang N D and Arima A 2003 *Phys. Rev. C* **67** 014304
- [100] Dang N D and Arima A 2003 *Phys. Rev. C* **68** 039902

- [101] Hung N Q, Dang N D and Huong L T Q 2016 *Phys. Rev. C* **94** 024341
- [102] Maino G, Menapace E and Venture A 1980 *Il Nuovo Cimento A* **57** 427–44
- [103] Benzi V, Maino G and Menapace E 1981 *Il Nuovo Cimento A* **66** 1–26
- [104] Lipkin H J 1960 *Ann. Phys., NY* **9** 272–91
- [105] Nogami Y and Zucker I J 1964 *Nucl. Phys.* **60** 203–8
- [106] Goodfellow J F and Nogami Y 1966 *Can. J. Phys.* **44** 1321–7
- [107] Pradhan H C, Nogami Y and Law J 1973 *Nucl. Phys. A* **201** 357–68
- [108] Magierski P, Cwiok S, Dobaczewski J and Nazarewicz W 1993 *Phys. Rev. C* **48** 1686–94
- [109] Dang N D, Ring P and Rossignoli R 1993 *Phys. Rev. C* **47** 606–11
- [110] Hubbard J 1959 *Phys. Rev. Lett.* **3** 77–8
- [111] Stratonovich R D 1957 *Dokl. Akad. Nauk SSSR* **115** 1907  
Stratonovich R D 1958 *Sov. Phys.—Dokl.* **2** 416
- [112] Lauritzen B, Arve P and Bertsch G 1988 *Phys. Rev. Lett.* **61** 2835–8
- [113] Esebbağ C and Egido J L 1993 *Nucl. Phys. A* **552** 205–32
- [114] Gambacurta D and Lacroix D 2012 *Phys. Rev. C* **85** 044321
- [115] Hung N Q and Dang N D 2010 *Phys. Rev. C* **81** 057302
- [116] Hung N Q and Dang N D 2010 *Phys. Rev. C* **82** 044316
- [117] Hung N Q and Dang N D 2007 *Phys. Rev. C* **76** 054302
- [118] Hung N Q and Dang N D 2008 *Phys. Rev. C* **77** 029905
- [119] Alhassid Y, Bertsch G F and Fang L 2003 *Phys. Rev. C* **68** 044322
- [120] Guttormsen M, Bjerve A, Hjorth-Jensen M, Melby E, Rekstad J, Schiller A, Siem S and Belic A 2000 *Phys. Rev. C* **62** 024306
- [121] Chankova R *et al* 2006 *Phys. Rev. C* **73** 034311
- [122] Kalos M H 1962 *Phys. Rev.* **128** 1791–5
- [123] Carlson J 1987 *Phys. Rev. C* **36** 2026–33
- [124] Carlson J 1988 *Phys. Rev. C* **38** 1897–910
- [125] Johnson C W, Koonin S E, Lang G H and Ormand W E 1992 *Phys. Rev. Lett.* **69** 3157–60
- [126] Lang G H, Johnson C W, Koonin S E and Ormand W E 1993 *Phys. Rev. C* **48** 1518–45
- [127] Ormand W E, Dean D J, Johnson C W, Lang G H and Koonin S E 1994 *Phys. Rev. C* **49** 1422–8
- [128] Alhassid Y, Dean D J, Koonin S E, Lang G and Ormand W E 1994 *Phys. Rev. Lett.* **72** 613–6
- [129] Richter W A, Vandermerwe M G, Julies R E and Brown B A 1991 *Nucl. Phys. A* **523** 325–53
- [130] Alhassid Y, Bertsch G F, Dean D J and Koonin S E 1996 *Phys. Rev. Lett.* **77** 1444–7
- [131] Dean D J, Koonin S E, Langanke K and Radha P B 1997 *Phys. Lett. B* **399** 1–7
- [132] Richardson R W 1963 *Phys. Lett.* **3** 277–9
- [133] Richardson R W 1965 *Phys. Lett.* **14** 325–7
- [134] Richardson R W and Sherman N 1964 *Nucl. Phys.* **52** 221–38
- [135] Dukelsky J, Pittel S and Sierra G 2004 *Rev. Mod. Phys.* **76** 643–62
- [136] Gross D H E 1997 *Phys. Rep.* **279** 119–201
- [137] Dukelsky J and Schuck P 1999 *Phys. Lett. B* **464** 164–8
- [138] Hirsch J G, Mariano A, Dukelsky J and Schuck P 2002 *Ann. Phys., NY* **296** 187–213
- [139] Puhlhofer F 1977 *Nucl. Phys. A* **280** 267–84
- [140] Chakrabarty D R, Datar V M, Kumar S, Mirgule E T, Oza H H and Pal U K 1995 *Phys. Rev. C* **51** 2942–51
- [141] Chakrabarty D R, Datar V M, Kumar S, Mirgule E T, Oza H H and Pal U K 1996 *Phys. Rev. C* **53** 2022
- [142] Cwiok S, Dudek J, Nazarewicz W, Skalski J and Werner T 1987 *Comput. Phys. Commun.* **46** 379–99
- [143] Hua H *et al* 2003 *Phys. Lett. B* **562** 201–7
- [144] Alhassid Y, Levit S and Zingman J 1986 *Phys. Rev. Lett.* **57** 539–42
- [145] Meul H W, Rossel C, Decroux M, Fisher Ø, Remenyi G and Briggs A 1984 *Phys. Rev. Lett.* **53** 497–500
- [146] Maple M B 1985 *Nature* **315** 95–6
- [147] Lin C L, Teter J, Crow J E, Mihalisin T, Boorks J, Abou-Aly A I and Stewart G R 1985 *Phys. Rev. Lett.* **54** 2541–4
- [148] Uji S, Shinagawa H, Terashima T, Yakabe T, Terai Y, Tokumoto M, Kobayashi A, Tanaka H and Kobayashi H 2001 *Nature* **410** 908–10
- [149] Konoike T, Uji S, Terashima T, Nishimura M, Yasuzuka S, Enomoto K, Fujiwara H, Zhang B and Kobayashi H 2004 *Phys. Rev. B* **70** 094514
- [150] Niwata M, Masutomi R and Okamoto T 2017 *Phys. Rev. Lett.* **119** 257001
- [151] Jaccarino V and Peter M 1962 *Phys. Rev. Lett.* **9** 290–2
- [152] Fischer Ø 1972 *Helv. Phys. Acta* **45** 331–97
- [153] Ignatyuk A V 1975 *Sov. J. Nucl. Phys.* **21** 10  
Ignatyuk A V 1975 *Yad. Fiz.* **21** 20
- [154] Ignatyuk A V 1974 *Izv. Acad. Nauk. Ser. Fiz.* **38** 2613
- [155] Baznat M I, Ignatyuk A V and Pyatov N I 1979 *Sov. J. Nucl. Phys.* **30** 493
- [156] Dang N D and Thang N Z 1988 *J. Phys. G: Nucl. Phys.* **14** 1471–8
- [157] Ponomarev V Yu and Vdovin A I 2005 *Phys. Rev. C* **72** 034309
- [158] Dang N D and Arima A 2006 *Phys. Rev. C* **74** 059801
- [159] Dang N D 2007 *Nucl. Phys. A* **784** 147–60
- [160] Dang N D and Arima A 1998 *Phys. Rev. Lett.* **80** 4145–8
- [161] Dang N D and Arima A 1998 *Nucl. Phys. A* **636** 427–51
- [162] Dang N D and Arima A 2003 *Phys. Rev. C* **68** 044303
- [163] Heckman P *et al* 2003 *Phys. Lett. B* **555** 43–8
- [164] Bracco A *et al* 1989 *Phys. Rev. Lett.* **62** 2080–3
- [165] Gaardhoje J J, Bruce A M and Herskind B 1988 *Nucl. Phys. A* **482** 121c–40c
- [166] Berman B L 1975 *At. Data Nucl. Data Tables* **15** 319–90
- [167] Pandit D, Pal S, De A and Banerjee S R 2012 *Phys. Lett. B* **713** 434–8
- [168] Kumar A K R, Arumugam P and Dang N D 2014 *Phys. Rev. C* **90** 044308
- [169] Harakeh M N and Van der Woude A 2001 *Giant Resonances: Fundamental High-Frequency modes of Nuclear Excitation* (Oxford: Oxford Science Publications)
- [170] Dang N D, Eisenman K, Seitz J and Thoennessen M 2000 *Phys. Rev. C* **61** 027302
- [171] Baumann T *et al* 1998 *Nucl. Phys. A* **635** 428–45
- [172] Mukhopadhyay S *et al* 2012 *Phys. Lett. B* **709** 9–13
- [173] Dilg W, Schantl W, Vonach H and Uhl M 1973 *Nucl. Phys. A* **217** 269–98
- [174] Junghans A R, Jong M, Clerc H G, Ignatyuk A V, Kudyaev G A and Schmidt K H 1998 *Nucl. Phys. A* **629** 635–55
- [175] Nasrabadi M N and Sepiani M 2014 *Acta Phys. Pol. B* **45** 1865–74
- [176] Ignatyuk A V 1983 *The Statistical Properties of the Excited Atomic Nuclei* (Moscow: Energoatomizdat)
- [177] Bjørnholm S, Bohr A and Mottelson B 1974 *Proc. of the Symp. on Physics and Chemistry of Fission* vol I (Vienna: IAEA) p 367
- [178] Iljinov A S 1992 *Nucl. Phys. A* **543** 517–57
- [179] Capote R *et al* 2009 *Nucl. Data Sheets* **110** 3107–214
- [180] Dang N D and Hung N Q 2013 *J. Phys. G: Nucl. Part. Phys.* **40** 105103
- [181] <https://www-nds.iaea.org/RIPL-3/>
- [182] Schiller A, Bjerve A, Guttormsen M, Hjorth-Jensen M, Ingebretsen F, Melby E, Messelt S, Rekstad J, Siem S and Ødegård S W 2001 *Phys. Rev. C* **63** 021306

- [183] Hilaire S and Goriely S 2006 *Nucl. Phys.* **799** 63–81
- [184] Goriely S, Hilaire S and Koning A J 2008 *Phys. Rev. C* **78** 064307
- [185] Kadenskij S G, Markushev V P and Furman V I 1983 *Yad. Fiz.* **37** 277  
Kadenskij S G, Markushev V P and Furman V I 1983 *Sov. J. Nucl. Phys.* **37** 165
- [186] Brink D M 1955 *PhD Thesis* Oxford University
- [187] Axel P 1962 *Phys. Rev.* **126** 671–83
- [188] Dang N D, Hung N Q and Huong L T Q 2017 *Phys. Rev. C* **96** 054321
- [189] Voinov A V, Grimes S M, Brunes C R, Massey T and Schiller A 2012 *EPJ Web. Conf.* **21** 05001
- [190] Dey B *et al* 2017 *Phys. Rev. C* **96** 054326



**Nguyen Quang Hung** received his PhD (2009) in theoretical and mathematical physics from an Asian Program Associate between Institute of Physical and Chemical Research (RIKEN), Japan and Institute of Physics, Hanoi, Vietnam. He became a Nishina Memorial fellow (2010) at RIKEN and Assistant Professor at Tan Tao University in Vietnam (2011–2014). Since 2015, he has been appointed as Associate Professor and later Director of Institute of Fundamental and Applied Sciences at Duy Tan University in Ho Chi Minh city, Vietnam. His research has focused on nuclear pairing properties at zero temperature, finite temperature, and finite angular momentum, quantal and thermodynamic fluctuations in finite systems, and nuclear giant and pigmy dipole resonances. Recently, his research subject has been extended to the nuclear level scheme, level density, and radiative strength function of the gamma-rays emission.



**Nguyen Dinh Dang** received the degrees of Candidate of Physical and Mathematical Sciences from the Joint Institute for Nuclear Research (Dubna) in 1985 and Doctor of Physical and Mathematical Sciences from the Moscow State University in 1990. He was a research scientist at the Vietnam Atomic Energy Institute (1982, 1987–2018) and Institute of Physics at the Vietnam Academy of Science and Technology (1985–1987). After conducting research in Europe in 1992–1993 at the Technical University of Munich and Catania Section of the National Institute of Nuclear Research, he came to Japan, first as a Nishina Memorial Fellow at the Institute of Nuclear Research of the University of Tokyo (1994 - 1995), then a Research Fellow of the Japan Science Technology Agency at RIKEN (Wako, 1996–1998), where he has been employed as a Nishina Center Research Scientist since 1994. The subjects of his research include nuclear collective excitations and properties of highly excited nuclei such as nuclear pairing, nuclear giant resonances, and nuclear thermodynamics.



**Luciano Moretto** received his PhD in Chemistry at University of Pavia in 1964, where he became a lecture in chemistry in 1965. After receiving the Fellowship “Miranda” Award at the Accademia dei Lincei in Rome in 1965–1966, he came to the Lawrence Berkeley National Laboratory (LBNL) as a postdoctoral fellow at the Nuclear Chemistry Division in 1966–1968, where he was appointed a group leader of Fission and Heavy-Ion Studies in 1971, a position he holds until present. After his positions as an Assistant Professor (1968–1970) and Libera Docenza and radiochemistry and nuclear chemistry (1970) at the University of Pavia, he became an Assistant Professor (1971–1972), Associate Professor (1973), Sloan Fellow (1974–1978), and a Full Professor (1977 until present) at the Department of Chemistry of the University of California at Berkeley. He was awarded the Alexander von Humboldt Prize in 1983 and Glenn T. Seaborg Award in Nuclear Chemistry of the American Chemical Society in 2005. He is a pioneer in the study of nuclear superfluidity in excited finite systems such as atomic nuclei in 1970s. His recent research subjects

include nuclear mesoscopic thermodynamics, its application to the interpretation of nuclear reactions in a variety of regimes, nuclear multifragmentation, interpretation of complex nuclear reactions, nuclear phase transitions and nuclear level densities.